PONTIFICIA UNIVERSIDAD CATOLICA DE CHILE

SCHOOL OF ENGINEERING

RESPONSE OF REINFORCED CONCRETE SHEAR WALL BUILDINGS DURING THE 2010, CHILE EARTHQUAKE

ROSITA JÜNEMANN URETA

Thesis submitted to the Office of Graduate Studies in partial fulfillment of the requirements for the Degree of Doctor in Engineering Sciences

Advisor:

JUAN CARLOS DE LA LLERA MARTÍN

Santiago de Chile, May, 2016

PONTIFICIA UNIVERSIDAD CATOLICA DE CHILE
ESCUELA DE INGENIERIA

RESPONSE OF REINFORCED CONCRETE SHEAR WALL BUILDINGS DURING THE 2010, CHILE EARTHQUAKE

ROSITA JÜNEMANN URETA

Members of the Committee:

JUAN CARLOS DE LA LLERA MARTÍN

RAFAEL RIDDELL CARVAJAL

MATÍAS ANDRÉS HUBE GINESTAR

PETER DECHENT ANGLADA

JACK P. MOEHLE

CRISTIÁN VIAL EDWARDS

Thesis submitted to the Office of Research and Graduate Studies in partial fulfillment of the requirements for the Degree of Doctor in Engineering Sciences

Santiago de Chile, May, 2016

To my dad who motivated me to be an engineer, and to my husband and children who are my inspiration.

ACKNOWLEDGEMENTS

I wish to express my sincere gratitude to my advisor Professor Juan Carlos de la Llera for his continuous support, motivation and knowledge. I would also like to thank Professor Matías Hube, for his insightful comments and dedication to this research. Additionally, I would like to thank the rest of my thesis committee for being part of this dissertation: Professors Rafael Riddell, Peter Dechent, Cristian Vial and Jack Moehle.

In addition, I would like to thank particularly to Professor Eduardo Kausel, who guided me as a visiting student at MIT, an experience that enriched this dissertation and was truly transformational. Special thanks for his hospitality, for his joy and for all the advice regarding my research.

My thanks also go to all the people and institutions that made this work possible. Particularly to the faculty of the Structural and Geotechnical Engineering Department of the Pontificia Universidad Catolica de Chile, and specially to the professors Rodrigo Jordán, Carl Lüders and Raúl Álvarez. Thanks also to the following engineers and students, who have been part of this research work: Rocío Rivera, Benjamín Westenenk, Cristóbal Alarcón, Felipe Quitral and Felipe Rivera. Particularly, I would like to thank Matías Chacón and Jorge Vásquez, for their great support. Finally, I would like to thank the companies SIRVE S.A., DICTUC S.A., and Spoerer Ingenieros Asociados SpA for their support throughout this work.

This research has been funded by the Chilean Fondo Nacional de Ciencia y Tecnología, Fondecyt through Grants #1110377 and #1141187, Fondap through Grant # 15110017, and MIT International Science and Technology Initiatives MISTI 2011 “Damage to Chilean High-rise Buildings During Large Thrust Earthquakes”. I am grateful for this support, without which this dissertation would have not been possible. This work was also funded by grants from the CONICYT / Human Capital Formation and Becas Chile.

However, none of this would have been possible without the quest for knowledge inculcated by my parents and specially by my father who motivated me to become an engineer, and without the unconditional support and encouragement of my husband Jaime and my children Jaime, Antonio and Ana.

TABLE OF CONTENTS

Page

LIST OF TABLES

Page

LIST OF FIGURES

Page

PONTIFICIA UNIVERSIDAD CATOLICA DE CHILE
SCHOOL OF ENGINEERING

RESPONSE OF REINFORCED CONCRETE SHEAR WALL BUILDINGS DURING THE MAULE EARTHQUAKE

Thesis submitted to the Office of Research and Graduate Studies in partial fulfillment of the requirements for the Degree of Doctor in Engineering Sciences by

ROSITA JÜNEMANN URETA

ABSTRACT

This dissertation presents an investigation on the earthquake behavior of Chilean "fish-bone" type shear-wall buildings that were damaged during the February 27, 2010 Great Maule earthquake (Mw=8.8). It makes a case that most of the damage took place in newer high rise buildings, caused in part by the use of ever slenderer walls in progressively taller buildings, and more importantly, by brittle failure in the walls at lower elevations due to high compressive loads in buildings with more than ten stories.

Close to 2% of the reinforced concrete buildings taller than 9 stories in Chile underwent substantial damage during the earthquake. Field observations have also revealed a high incidence of non-ductile (i.e. brittle) bending and compression failures of reinforced concrete shear walls which are typically found in the lower stories and first basements. Considering that other buildings with similar structural concepts performed rather well during this earthquake, it behooves to elucidate by comparative analysis some of the reasons underlying one type of behavior or the other. The typical Chilean "fish-bone" building behaved rather very well during the large, previous 1985 Chile earthquake, and one of the main reasons for this behavior may have been their conservative design, as reflected in their large amount of total shear-wall to floor area of, say, 5-6%. Considering that construction practices and design precepts have evolved significantly in Chile since 1985, one of the goals of this research is to discern how those design practices may have changed and thus influenced the seismic performance of tall buildings.

Although in a large majority RC buildings performed well during 2010 Maule Earthquake, this research aims to understand the observed damaged and earthquake behavior of these structures. To reach this goal, this dissertation is divided in three phases: (i) description of RC shear wall buildings damaged during 2010 Chile earthquake based on the analysis of data gathered in the field; (ii) inelastic analysis and response of RC walls damaged during 2010 earthquake by means of pushover analysis of a single wall; and (iii) three-dimensional inelastic dynamic analysis and response of a real RC building based on a detailed finite element model, with the goal of predicting damage using real earthquake records.

Keywords: shear wall damage, pushover analysis, inelastic finite element models, dynamic inelastic analysis, reinforced concrete buildings, thin shear walls, Chile earthquake.

Members of the Doctoral Thesis Committee:

Juan Carlos de la Llera Martín

Rafael Riddell Carvajal

Matías Andrés Hube Ginestar

Peter Dechent Anglada

Jack P. Moehle

Cristián Vial Edwards

Santiago, May, 2016

1. INTRODUCTION

1.1.The 2010 Chile earthquake and RC building behavior

Chile has suffered the consequences of many earthquakes of Magnitude $M_w \geq 7.5$ in the last 60 years (1960 Valdivia M_w=9.5; 1985 Llolleo M_w=8; 2010 Maule M_w=8.8; 2014 Iquique M_w=8.2; 2015 Coquimbo M_w=8.4, among others) [1]. The February 27th 2010 Maule earthquake was one of the strongest ever measured (M_w=8.8). Its effects were felt over 500 km of the central Chile coast, affecting more than 12 million people, which is about 75% of the country's population. The earthquake also triggered a tsunami that devastated several coastal towns in south-central Chile. Both the motion and the tsunami resulted in more than 500 deaths, around 2 million injuries, and serious damage to residential buildings, hospitals, schools, industries, lifelines, and other infrastructure. The losses by the earthquake and tsunami were estimated in USD 30 billion (~18% Chile's GDP) [2]. Nevertheless, the seismic behavior of engineered buildings, specifically medium to high rise reinforced concrete (RC) shear wall buildings has generally been very good [3][4].

The high-rise buildings in Chile began mainly as steel structures not higher than 12 stories in the 1920's. Beginning in the 1930's, buildings with reinforced concrete walls and facades started to be common. But only since 1940's, following the then new General Building Ordinance, most of the walls in buildings started to be made of reinforced concrete. Structural systems for RC buildings can be classified in one of three groups: (i) shear walls system; (ii) dual frame-wall system; or (iii) moment-resisting frames. Between 1940 and 1960, the typical structural configuration was shear wall system, with a large number of thick walls. From the 1970's and on Chile begun the construction of reinforced concrete buildings using a combination of both frame and shear walls. However, almost 77% of Chilean buildings constructed since 1940 are of the shear-wall type and the majority of them have residential use [5][6].

This type of buildings is commonly called “fish-bone” type (Figure 1-1a) and b)), which characterizes by relying almost exclusively on a system of RC shear walls to withstand gravity and lateral loads. They present a typical plan with a central longitudinal corridor with shear walls and transverse walls that separate building apartments and interior rooms. Transverse walls run from the corridor toward the building exterior creating a topology like a “fish bone”. Usually, a couple of basement stories are included, and no lintels are used to link the walls. These buildings are typically for residential use and range usually between 5 and 25 stories in height. On average they have 13 floors, but buildings over 15 floors are now more common, especially since 1996 [5][7]. Furthermore, the ratio of wall area to floor plan area, i.e. the wall density, is relatively large compared with buildings of similar height in seismic regions of the U.S. Wall densities in Chile range most commonly between 1.5% to 3.5% in each direction, with a mean value of 2.8%, a characteristic that has remained almost constant in time [5][7][8]. Walls are rather uniformly distributed in the two principal directions and the large amount of wall area results in very stiff buildings. It is generally believed that the significant stiffness given by the large amounts of wall area may have been responsible for the good seismic behavior of this type of buildings during the 1985 Chile earthquake [3][4].

Although a large majority of medium to tall RC buildings performed well during 2010 Maule earthquake, extensive localized brittle damage occurred in some of these structures located in the main cities affected by the earthquake: Santiago, Viña del Mar and Concepción. Observed damage was typically concentrated in the first story and basements, characterized by concrete crushing over a short height of the wall but in most cases almost over its entire length (Figure 1-1(c)). Reinforcement buckling and fracture was observed, and global wall buckling was also found in some cases. Different authors have reported detailed descriptions of observed damage after 2010 earthquake in RC wall buildings [9][10][11][12]. Damaged buildings were in a large majority modern buildings constructed after year 2000, however, many buildings of similar topology did not undergo damage during the earthquake and thus the question is why not.

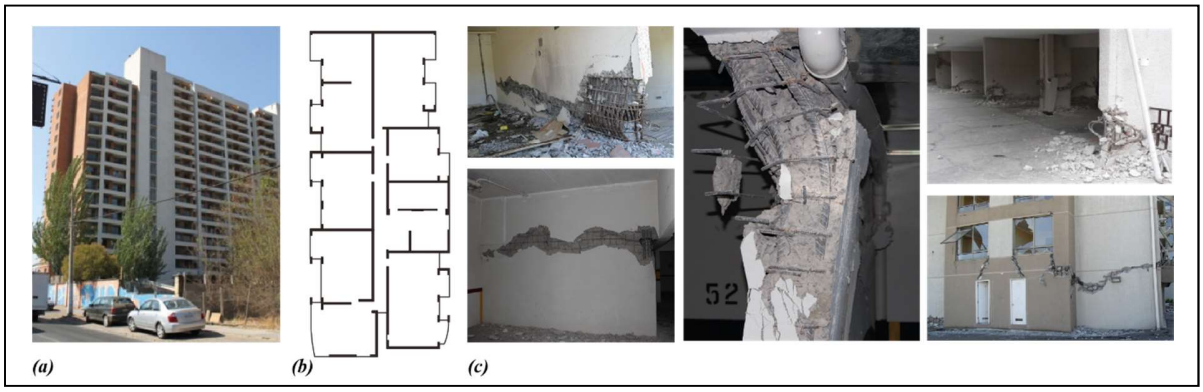

Figure 1-1: a) Typical "fish-bone" RC building; b) typical floor plan layout; and c) examples of observed damage in RC walls after 2010 earthquake

It is apparent that construction practices in Chile have evolved significantly from those that existed during the previous 1985 earthquake and the well behaved, and relatively resistant and stiff buildings of a quarter of century ago gave way to new, more daring and thus less conservative designs. First, modern buildings often use thinner walls, and second, they are often taller, or both. Despite these obvious changes, they still present similar wall densities than yesteryear. It is then not surprising that both of these factors have resulted in substantial increases in the axial loads carried by structural elements at lower elevations. Moreover, the use of parking areas in basements where structural walls are opened up for car circulation has often led to setbacks in wall elevation profiles and thus, to increased compression forces in those walls, which may have been one of the reasons for the frequently observed brittle failure modes below the ground level.

At the time of 2010 earthquake, current regulation in Chile was based on two main documents: (i) provisions for seismic design of buildings (Nch433of96) [13]; and (ii) provisions for Reinforced Concrete (Nch430of2008) [14]. They were based on ACI 318-95[15] provisions, however, Chilean provisions excluded the requirement of special confinement reinforcement in boundary elements, due to the good performance observed in the 1985 earthquake. Additionally, there was no restriction to the axial load or minimum thickness requirement for RC walls. After the 2010 earthquake, both Chilean seismic codes were modified. First, decree N60 [16] modified the Chilean code for reinforced concrete design [14], by placing an upper limit to the maximum compressive stress in walls of $0.35f'_c$, defining new criteria for wall confinement similar to ACI 318-08 requirements, and

providing a new damage limitation by limiting compressive concrete strain to 0.008 [17]. The second decree N61 [18] provided a new design displacement spectra for estimating roof displacement and a new soil classification.

1.2. Experimental and analytical behavior of RC walls

Experimental campaigns on RC walls have been developed in the past to understand the behavior of this type of elements, however, few experimental programs have focused on the effect of high axial loads in slender walls. Su and Wong [19] tested 3 RC specimens to study the effect of axial load ratio (ALR) and confinement on the wall performance. They found that the effectiveness of confinement depends on the arrangement of the transverse reinforcement and not only on the amount of reinforcement. Additionally, they found that the ductility of the specimen decreases with high ALR and abrupt compressive failures were observed for high ALR (50%). The work by Zhang and Wang [20] also considered experimental campaign on RC specimens with high levels of axial load, and observed that the specimen with lower axial load presented larger displacement capacity.

For RC walls with high axial load ratios combined with poor confinement, as was the case of Chilean buildings, damage have shown to be localized in a reduced region of the wall, characterized by an abrupt flexural-compressive failure just after spalling of concrete cover, as shown by Alarcon *et al.* [21]. Furthermore, Massone *et al.*[22], and Arteta *et al.*[23], have tested RC boundary elements with different levels of confinement under pure compression. On the one hand, Massone *et al.* [22] showed that although confinement traduces in a more ductile response, it is less effective in thinner specimens, thus a greater thickness is required to properly use confinement. On the other hand, Arteta *et al.* [23] proved experimentally that more confinement could not prevent a brittle behavior of boundary elements when subjected to pure compression. Segura and Wallace [24] have shown that for thin walls with boundary reinforcement according to ACI provisions, abrupt compression failures at wall boundaries occur for low axial load ratios (10%). This result is probably associated with larger displacement demands and also more ductility than the observed by Alarcon *et al*. [21].

Different analytical tools have been used in the past to represent the behavior of RC walls, which can be grouped in two main families: micro-modeling that generally discretize the real specimen into small elements where concrete and steel are considered separately, such as finite element models and fiber element models; and macro-models where the overall behavior of the RC element is represented as a whole [25]. Regarding behavior of Chilean RC walls, Magna *et al.* [26] have used a multi-spring macro-model including a horizontal shear spring with calibrated properties. Also, Vasquez *et al.* [27] have proposed a new force-based fiber element (FFE) for cyclic analysis including shear effects, buckling, and fracture of steel bars.

Regarding finite element models, two main approaches are commonly considered to model concrete fracture: the *cohesive crack* model, which assumes the fracture localized in a discrete crack, and the *smeared crack* model, which assumes the fracture distributed within a continuum with a defined stress-strain relation. Within the *smeared crack* model, a *decomposed strain* concept or a *total strain* concept can be considered for the stress-strain relations. In the first case the strain is decomposed into elastic (ε_e) and cracking (ε_{cr}) strain components, while in the second case the stress is considered as a function of the total strain. Additionally, there are two alternatives to model the shear stress-strain relationships: *fixed* and *rotating*. In the *fixed crack* model the principal axes are fixed during the post-cracking phase, while in the *rotating crack* model the principal axes co-rotate with the principal strains during crack propagation [28]. The smeared crack model has been widely used in finite element models and has been implemented in different available software [29]. The *total strain rotating crack* model implemented in the software DIANA [30] allows for orthotropic material and has been used by other authors showing good results to represent RC behavior [31][32][33].

Regarding three-dimensional inelastic finite element models of RC wall buildings, Rana *et al.* [34] developed a pushover analysis of a 19 story RC shear wall building in SAP2000 using equivalent frame elements to model shear walls. Penelis and Papanikolaou [35], developed nonlinear static and dynamic analysis of a 16 story RC building with dual system (frame-wall), where structural walls were modeled using vertical frame elements.

Ebrahimian *et.al* [36] developed a 3D nonlinear FE model in the software DIANA for the pre-test numerical simulation of a full scale five-story RC building specimen tested on the NEES-UCSD shake table, and results from the simulation are compared with experimental results. Kozmidis *et.al* [37] used fiber elements in Perform 3D to develop a nonlinear dynamic analysis on a tall RC building damaged during 2010 earthquake. Additionally, a broad initiative developed by NHERP [38] discusses approaches for analytical modeling of RC wall buildings, and presents a series of studies using these models to capture behaviors observed in experimental tests and buildings damaged in the 2010 Maule earthquake. The collapse of Alto Río building during 2010 earthquake was studied using a 3D finite element model using shell elements of a representative slice of the building in the software LS-DYNA [38].

1.3. Objectives and organization of the thesis

Motivated by the significant information provided by the "natural experiment" to which the RC shear-wall buildings were subjected to during the 2010 Chile earthquake, this research aims to understand the behavior of RC wall structures during this event. Although a large majority of medium to tall RC buildings performed well during 2010 Chile Earthquake, the extensive localized brittle damage observed in RC walls of buildings in different locations of the country, and the fact that many buildings of similar topology did not undergo damage during the earthquake are the main drivers of this investigation. Hence, it behooves to elucidate the following issues: What are the structural characteristics responsible for the observed damage? What makes these buildings different from other buildings with similar structural characteristics but without damage? Can the observed behavior be predicted by means of analytical models? Can we describe the seismic response of this type of buildings by means of inelastic dynamic analysis? To answer these questions, this research follows three avenues of research: (i) Description of RC shear wall buildings damaged during 2010 Chile earthquake based on the analysis of data gathered in the field; (ii) inelastic analysis and response of RC walls damaged during 2010 earthquake by means of pushover analysis of single walls; and (iii) three-dimensional inelastic dynamic analysis and response of a real

RC building based on a detailed finite element model, with the goal of predicting damage using real earthquake records. The document is written in the format of three independent articles, so each chapter or phase is a self-contained paper that has been published or is in the process of being published [39][40][41].

The first phase of this research (Chapter 2 [39]) focuses in the inventory of RC wall buildings with 10 or more stories that were damaged during the earthquake. Global parameters including geometric plan and height characteristics, material properties, dynamic parameters, wall parameters and irregularity indices of 36 buildings this type were calculated, analyzed and compared with the general building inventory and with a small benchmark of undamaged buildings with very similar configuration than the damaged ones. The correlation between damage level and global building parameters is explored in terms of ordinal logistic regression models. Finally, an estimation of the dynamic amplification factor of axial load ratios in this type of buildings is presented.

The second phase (Chapter 3 [40]) aims to study analytically the observed damage pattern of shear wall buildings during the 2010 earthquake. Two-dimensional inelastic pushover finite element models using DIANA are developed and validated with experimental data of RC walls available in the literature. The finite element models consider 4-node shell elements, where the inelastic behavior of concrete is simulated using the *total strain rotating crack* model, and reinforcement was modeled using an embedded formulation. Then, two walls that were severely damaged during the earthquake were studied in detail using different load patterns and stress-strain constitutive relationships for concrete in compression, and results are compared with the observed damage after the earthquake, and with results from a dynamic inelastic analysis of the building based on fiber elements.

Finally, the third phase of this study (Chapter 4 [41]) presents a three-dimensional inelastic dynamic analysis of a real building damaged during the 2010 earthquake, and subjected to different components of a ground motion recorded near the building for similar soil conditions. The building is modeled in the software DIANA with 3 or 4-node shell elements, following the same formulation of the second phase. Because the damage observed in this

building was localized mainly in the first basement, inelastic elements are concentrated in the first three stories of the building while the rest of the structure is modeled with linear-elastic behavior. Finally, different modeling assumptions, like the number and location of inelastic elements and the slab stiffness, are evaluated through a parametric study.

REFERENCES

[1] Servicio Sismológico Universidad de Chile, Sismos Importantes o destructivos desde 1950 http://www.sismologia.cl/

[2] Gobierno de Chile (2010). Plan de Reconstrucción, Terremoto y Tsunami 27 Febrero, 2010. Resumen Ejecutivo [in Spanish]. Concepción, Chile.

[3] Wood S.L. (1985). "Performance of reinforced concrete buildings during the 1985 Chile earthquake: implications for the design of structural walls." Earthquake Spectra; 7(4):607–638.

[4] Hidalgo, P., Ledezma, C., Jordán, R., (2002). "Seismic Behavior of Squat Reinforced Concrete Shear Walls." Earthquake Spectra, 18(2):287-308.

[5] Calderón J.A. (2007) "Update on structural system characteristics used in RC building construction in Chile." Civil Engineering Thesis. University of Chile. p. 76 [in Spanish].

[6] Moroni O., Astroza M. (2002) "Characteristic housing types in Chile." 7th U.S. National Conference on Earthquake Engineering (7NCEE).

[7] Gómez, C.E. (2001). Caracterización de Sistemas Estructurales Usados en las Viviendas de Hormigón Armado y Albañilería en Chile, Memoria para optar al título de Ingeniero Civil, Universidad de Chile.

[8] Guzmán, M.A., (1998). Caracterización de Tipologías Estructurales Usadas en el Diseño de Edificios Altos en Chile, Memoria para optar al título de Ingeniero Civil, Universidad de Chile.

[9] Rojas F., Naeim F., Lew M., Carpenter L.D., Youssef N.F., Saragoni G.R., Schachter M. (2011) "Performance of tall buildings in Concepcion during the 27 February 2010

moment magnitude 8.8 offshore Maule, Chile earthquake." Structural Design of Tall and Special Buildings; 20:37–64.

[10] Carpenter L.D., Naeim F., Lew M., Youssef N.F., Rojas F., Saragoni G.R., Schachter M. (2011) "Performance of tall buildings in Viña del mar during the 27 February 2010 offshore Maule, Chile earthquake." Structural Design of Tall Special Buildings; 20:17–36.

[11] Westenenk B., de la Llera J.C., Besa J.J., Jünemann R., Moehle J., Lüders C., Inaudi J.A., Elwood K.J., Hwang S-J. (2012) "Response of reinforced concrete buildings in Concepción during the Maule earthquake." Earthquake Spectra; 28(S1):S257–80.

[12] Westenenk B., de la Llera J.C., Jünemann R., Hube M.A., Besa J.J., Lüders C., Inaudi J.A., Riddell R., Jordán R.. (2013) "Analysis and interpretation of the seismic response of RC buildings in Concepción during the February 27, 2010 Chile Earthquake." Bulletin of Earthquake Engineering; 11(1):69–91.

[13] Instituto Nacional de Normalización, (1996). Diseño Sísmico de Edificios, Nch433Of.1996, Santiago, Chile.

[14] Instituto Nacional de Normalización (2008). Hormigón-Requisitos de Diseño y Cálculo, Nch430Of.2008, Santiago, Chile

[15] American Concrete Institute Committee 318 (1995). Building Code Requirements for Reinforced Concrete (ACI 318-05). American Concrete Institute, Detroit, USA.

[16] D.S. N 60 (2011) MINVU. Reinforced concrete design code, replacing D.S N 118. Chilean Ministry of Housing and Urbanism 2010, Diario Oficial; 13 December 2011 [in Spanish].

[17] Massone L. (2013) "Fundamental principles of the reinforced concrete design code changes in Chile following the Mw 8.8 earthquake in 2010". Engineering Structures; 56(2013) 1335-1345.

[18] D.S. N 61 (2011) MINVU. Building seismic design code, replacing D.S N 117, 2010. Chilean Ministry of Housing and Urbanism, Diario Official; 13 December 2011 [in Spanish].

[19] Su R., Wong S. (2007) "Seismic behavior of slender reinforced concrete shear walls under high axial load ratio." Engineering Structures; 29:1957–65.

[20] Zhang Y., Wang Z. (2000) “Seismic behavior of reinforced concrete shear walls subjected to high axial loading.” ACI Structural Journal; 97(5):739–50.

[21] Alarcon C., Hube M.A., de la Llera J.C. (2014) “Influence of axial load in the seismic behavior of RC walls unconfined wall boundaries.” Engineering Structures; 73:13-23.

[22] Massone L.M., Polanco P., Herrera P. (2014) “Experimental and analytical response of RC wall boundary elements”. Proceedings of the 10th National Conf. in Earthquake Engineering, Earthquake Engineering Research Institute, Anchorage, AK.

[23] Arteta C.A., To D.V., Moehle J.P. (2014) “Experimental response of boundary elements of code-compliant reinforced concrete shear walls.” Proceedings of the 10th National Conference in Earthquake Engineering, Earthquake Engineering Research Institute, Anchorage, AK.

[24] Segura, C., and Wallace J. (2915). “Experimental Study on the seismic performance of thin reinforced concrete structural walls”. SEFC 2015 Proceedings, Tokyo Institute of Technology, Yokohama, Japan

[25] Galal K., El-Sokkary H. (2008) Advancement in modeling of RC shear walls.” Proceedings of the 14th World Conference on Earthquake Engineering, Beijing, China

[26] Magna-Verdugo C.E., Kunnath S.K. (2014) “Non-linear response analysis of reinforced concrete shear walls using multi-spring macro-models.” Proceedings of the 10th National Conference in Earthquake Engineering, Earthquake Engineering Research Institute, Anchorage, AK.

[27] Vasquez J.A., de la Llera J.C., Hube M.A. (2015) “A regularized fiber element model for reinforced concrete shear walls”. Earthquake Engineering and Structural Dynamics, accepted for publication.

[28] Feenstra P.H., de Borst R., and Rots J.G. (1991) “A comparison of different crack models applied to plain and reinforced concrete.” Proceedings of the International RILEM/ESIS Conference “Fracture Processes in Concrete, Rock and Ceramics”, Noordwijk, The Nehterlands.

[29] Johnson A. (2006) “Comparison of Nonlinear Finite Element Modeling Tools for Structural Concrete”. CEE561 Project, University of Illinois

[30] TNO DIANA. (2010). DIANA - User's Manual.

[31] Hube M.A. and Mosalam K.M. (2011). “Experimental and computational evaluation of in-span hinges in reinforced concrete box-girder bridges.” Journal of Structural Engineering, Vol. 137, No. 11, pp. 1245-1253.

[32] Quitral F. (2013) “Non-linear brittle behavior of shear wall buildings during 2010 Chile earthquake.” Master of Science Thesis. Pontificia Universidad Católica de Chile. (in Spanish)

[33] Dashti F., Dakhal R.P., and Pampanin S. “Numerical simulation of shear wall failure mechanisms”, Proceedings of the New Zealand Society for Earthquake Engineering 2014 Conference, Auckland, New Zealand.

[34] Rana R., Ji L., and Zekioglu A. (2004) “Pushover Analysis of a 19 Story Concrete Shear Wall Building”. Proceedings of 13th World Conference on Earthquake Engineering, Vancouver, Canada.

[35] Penelis G.G., Papanikolaou V.K. (2010) “Nonlinear Static and Dynamic Behavior of a 16-story Torsionally Sensitive Building Designed According to Eurocodes.” Journal of Earthquake Engineering, 14:706-725

[36] Ebrahimian H., Astroza R., Conte J.P., Restrepo J.I., Hutchinson T.C. (2014) “Experimental Validation of Dynamic Nonlinear FE Model of Full-Scale Five-Story Reinforced Concrete Building”. Proc of the 9th International Conference on Structural Dynamics, EURODYN 2014, Porto, Portugal

[37] Kozmidis A., Melek M., Massone L., Orakal K. (2014). “Comparison of industry-standard nonlinear dynamic analysis methods with observed damage on a RC building.” Proceedings of the 10th National Conference in Earthquake Engineering, Earthquake Engineering Research Institute, Anchorage, AK.

[38] NERHP (2014). “Recommendations for seismic design of reinforced concrete wall buildings based on studies of the 2010, Maule, Chile Earthquake.” NIST GCR 14-917-25. US Department of Commerce.

[39] Jünemann R., de la Llera J.C., Hube M.A., Cifuentes L.A., Kausel E. (2015) "A statistical analysis of reinforced concrete wall buildings damaged during the 2010, Chile earthquake". Engineering Structures, 82 (2015) 168–185.

[40] Jünemann R., de la Llera J.C., Hube M.A., Vasquez J.A., Chacón M.F. (2016) "Study of the damage of reinforced concrete shear walls during the 2010, Chile earthquake", Earthquake Engineering and Structural Dynamics, 45;10:1621-1641.

[41] Jünemann R., de la Llera J.C., Hube M.A. (2016) "Earthquake damage assessment of reinforced concrete shear wall buildings using a 3D finite element model", to be submitted for publication.

2. A STATISTICAL ANALYSIS OF REINFORCED CONCRETE WALL BUILDINGS DAMAGED DURING THE 2010, CHILE EARTHQUAKE

R. Jünemann*[a], J.C. De La Llera[a], M. A. Hube[a], L.A. Cifuentes[b] and E. Kausel[c]

[a] *National Research Center for Integrated Natural Disaster Management CONICYT/FONDAP/15110017 and Department of Structural and Geotechnical Engineering, Pontificia Universidad Católica de Chile, Vicuña Mackenna 4860, Santiago, Chile*

[b] *National Research Center for Integrated Natural Disaster Management CONICYT/FONDAP/15110017 and Department of Industrial and Systems Engineering, Pontificia Universidad Católica de Chile, Vicuña Mackenna 4860, Santiago, Chile*

[c] *Department of Civil and Environmental Engineering, Massachusetts Institute of Technology, 77 Massachusetts Ave, Cambridge, MA, United States*

ABSTRACT

This research article investigates the correlation between a suite of global structural parameters and the observed earthquake responses in 43 reinforced concrete shear wall buildings, of which 36 underwent structural damage during the M_w 8.8, 2010, Maule earthquake. During the earthquake, some of these buildings suffered brittle damage in few reinforced concrete walls. Damage concentrated in the first two building stories and first basement, and most typically, in the vicinity of important vertical irregularities present in the resisting planes. This research consolidates in a single database information about these 36 damaged buildings for which global geometric and building design parameters are computed. Geometry related characteristics, material properties, dynamic and wall-related parameters, and irregularity indices are all defined and computed for the inventory of damaged buildings, and their values compared with those of other typical Chilean buildings. A more specific comparison analysis is performed with a small benchmark group of 7 undamaged buildings, which have almost identical characteristics to the damaged structures, except for the damage. A series of ordinal logistic regression

models show that the most significant variables that correlate with the building damage level are the region where the building was located and the soil foundation type. Most of the damage took place in rather new medium-rise buildings, and was due in part to the use of increasingly thinner unconfined walls in taller buildings subjected to high axial stresses due to gravity loads, which in turn are increased by dynamic effects. Time-history analyses are performed in five damaged buildings to analyze in more detail the dynamic effect in these amplifications of the average axial load ratios. Finally, a simplified procedure to estimate this dynamic amplification of axial loads is proposed in these buildings as an intent to anticipate at early stages of the design the seismic vulnerability of these structures.

Keywords: shear wall damage, statistical damage analysis, reinforced concrete, seismic behavior, thin shear walls, Chile earthquake

2.1. Introduction

The February 27th (M_w=8.8 [1]), 2010, Maule earthquake, led to one of the strongest ground shaking ever measured. This megathrust event ruptured over 550 km of the plate convergence zone in south-central Chile (Figure 2-1a)), affecting more than 12 million people, i.e., about 70% of Chile's population. The earthquake also triggered a tsunami that devastated several coastal towns in this region [1][2]. Both, the motion and the tsunami, resulted in about 524 deaths (156 for the tsunami), more than 800,000 injuries, and caused an estimate of 30 billion dollars in direct and indirect damage to residential buildings, industry, lifelines, and other relevant infrastructure [3].

Although a large majority of reinforced concrete (RC) buildings performed well during the earthquake, close to 2% of the estimated 2,000 RC buildings taller than 9 stories suffered substantial damage during the earthquake [4]. Observed damage in RC structural walls was produced by a combination of bending and axial effects, and was located at the first few stories and basements. In some of these walls, and going from the first floor to the basement, their cross sections were reduced in length, thus creating a flag-shape of the wall that led to a concentration of stresses around the irregularity. The

failure was characterized by concrete crushing and spalling of the concrete cover, thus generating a horizontal crack that initiates at the free end of the wall and crosses its entire length (Figure 2-1b)-c)) toward the interior of the building. The boundary and web reinforcement buckles and sometimes fractures. The horizontal crack crosses the wall and usually stops due to the existence of a compression flange corresponding to the longitudinal corridor wall. Damage was typically localized in height, and out-of-plane buckling of the wall was also observed in several cases. Some examples of the so-called "unzipping" bending-compression failure are shown in Figure 2-1b), c) and d).

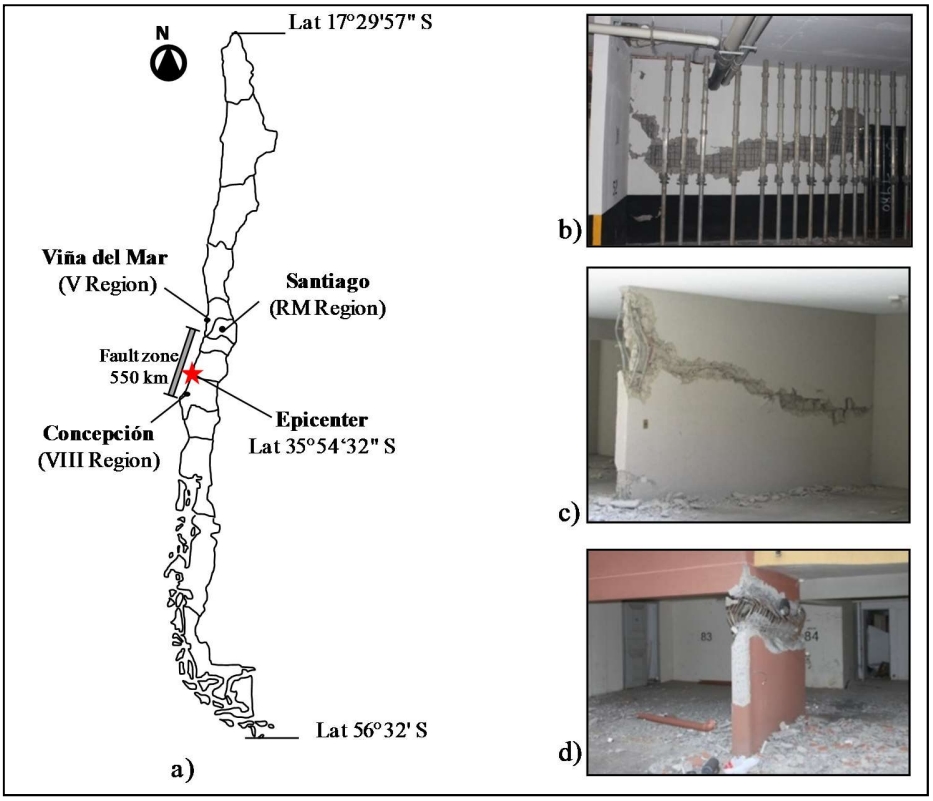

Figure 2-1. a) Map of Chile and principal cities affected by 2010 earthquake; b) typical failure in damaged building in Santiago; c) damaged building in Concepción; and d) damaged building in Viña del Mar.

The most common plan typology of residential Chilean building consists of a "fish-bone" configuration, which relies almost exclusively on a system of RC walls to resist both, gravity and lateral loads. Building plans are characterized by central longitudinal corridor

and transverse shear walls, the latter running orthogonally (Figure 2-2) to the corridor walls. It has been extensively reported in the literature that typical Chilean buildings behaved well during the 1985 Chile earthquake [5]. One of the main reasons for this behavior may have been their stiffness and over-strength at the time, as a consequence of the large amount of total shear-wall to floor area that ranged between 5 to 6% [5][6], which is relatively large compared with buildings of similar height in seismic regions elsewhere [5], and leads to low displacement and ductility demand requirements [7][8].

However, construction practices and design provisions have evolved in Chile since 1985. Because of real estate related issues, new buildings tend to be taller and with increasingly thinner walls, leading naturally to higher axial stresses. The Chilean seismic codes at the time of 2010 earthquake [9][10] did not limit the axial load and did not establish a minimum thickness for shear walls. Additionally, these codes incorporated ACI 318-95 [11] seismic provisions but excluded the special boundary elements due to the prior building success in 1985. This fact clearly affected the ductility capacity of these walls and structures, led to their poor boundary detailing, and made them more prone to brittle failures. Recent experimental results have shown that even if the boundary elements of these walls are properly confined, their behavior remains brittle [12]. In addition, there is little doubt that for specific bandwidths and soil types (II-stiff and III-soft), the 2010 earthquake exceeded the demand specified by the design spectrum. Buildings located in downtown Concepción with periods between 0.5 and 1s present spectral displacement demands two to four times larger than those for the design spectrum for soils II (stiff) and III (soft) [13].

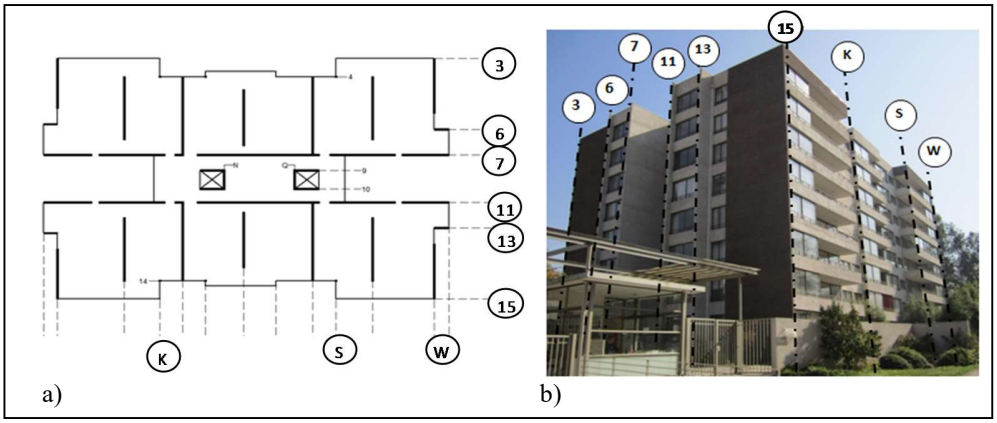

Figure 2-2. Typical "fish-bone" plan of Chilean residential building in Santiago: a) typical floor plan; and b) building photograph with some resisting planes.

After the 2010 earthquake, two new decrees were approved [14][15] that modified the provisions of previous codes. In particular, the first decree N°60 [14] modified the Chilean code for reinforced concrete design [9], placing an upper limit to the maximum compressive stress in walls of $0.35f'_c$, and defining new criteria for wall confinement. The second decree N°61 [15], modified the Chilean code for seismic design of buildings [10] by changing the soil classification and including several requirements for the soil type definition like geophysics studies, and by defining a more conservative displacement spectrum for buildings. Although there have been improvements in these decrees, new experimental data suggests that additional aspects may need to be considered in future code versions (e.g., [12]).

Recent publications on performance of RC buildings during 2010 earthquake focus mainly in description of observed damage [16][17], and description of construction practices. Westenenk et.al [18] presents a thorough damage survey for 8 damaged buildings in Concepcion, including a detailed description of the buildings. Also, a companion article [19] presents a complete code-type analysis of 4 damaged buildings, and a description of critical aspects like building orientation and observed damage, the evaluation of vertical and horizontal irregularities, wall detailing, and energy dissipation sources. Furthermore, Massone et. al [13] describes the typical design and construction practices of RC wall buildings in Chile. Finally, Wallace et.al [4] provides a description of observed damage, and analyzes critical aspects such as the lack of confinement at wall

boundaries, wall cross-section, and wall axial loads, including suggestions to design special RC shear walls.

This article focuses in the inventory of damaged buildings, trying to extract the most of the information contained in global building parameters. The fundamental aspects that this article aims to answer are questions such as: (i) which have been the main changes in construction practices since 1985, and how could they have influenced the seismic performance of tall buildings during the 2010 earthquake?; (ii) with the available building data, and computing basic global parameter estimations, would it be possible to differentiate in practice one building that would have undergone damage during the 2010 Chile earthquake, from one that would have not?; (iii) what would it be the most relevant information one could extract from the field observations and earthquake data regarding damage without going into inelastic and deeper analysis?; (iv) did a parameter like shear wall density, wall thickness, building slenderness, or axial load ratios played a role in the observed damage?

With these questions in mind, this article presents results of a large initiative that collected, classified, and analyzed data provided by 36 shear wall RC buildings taller than 9 stories that suffered light to severe damage during the earthquake. First, we attempt to correlate global building parameters with the observed damage. Geometric plan and height characteristics, material properties, dynamic parameters, wall-related parameters and irregularity indices of damaged buildings are compared with the general building inventory when possible, and with a small benchmark group of 7 undamaged buildings that were essentially identical to the damaged buildings in terms of geometry and structural design. Then, the association between building damage level and global building parameters was explored in terms of ordinal logistic regression models. Furthermore, we look at the axial load ratio (*ALR*) in RC walls including both, static and dynamic effects. A case-study building is analyzed in detail, and the *ALR* due to seismic actions is calculated by time-history analysis of a finite element model. Finally, a group of 4 buildings are analyzed with the same procedure, and an estimation of the dynamic

amplification factor of *ALR* is presented. This estimation can be used to evaluate at early stages of design the seismic vulnerability of RC wall buildings.

It is important to state upfront some of the assumptions of this research. There is no doubt that the earthquake response of a building is very complex, and several factors, beyond what global parameters can capture, control the seismic performance, such as specific ground motion characteristics (e.g., duration), foundation soil conditions, dynamic inelastic behavior of the soil and structure, coupling effects between vertical, lateral, and torsional effects, structural detailing of elements, quality control of the construction, and in general as built conditions as opposed to nominal design conditions. Although the structural parameters analyzed in this article will never be able to capture the entire complexities of the earthquake response of a building, the objective is to investigate how much of the response can be captured from their values, and validate if there is correlation, or not, with the observed earthquake building response and damage. Indeed, we would like to respond if these parameters help, and to what extent, as proxies for the brittle structural damage observed in these structures.

2.2. Building Inventory

The inventory of damaged buildings (Table 2-1) is composed of a group of Chilean "fish-bone" type buildings taller than 9 stories and located in the more populated cities affected by the earthquake, namely Santiago, Viña del Mar, and Concepción (Figure 2-1a)). From a total of 46 RC buildings of this type that suffered moderate to severe damage during the earthquake, complete information was obtained for 36 cases (Table 2-1). Structural and/or architectural drawings, soil-mechanics studies, and damage inspection reports were collected for almost all cases, thus generating a complete database of damaged buildings. Three damage levels were defined based on the operational conditions of the buildings immediately after the earthquake: damage level I is assigned to buildings with restricted use; damage level II to buildings declared non-habitable; and damage level III to collapsed buildings or with imminent risk of collapse. The damage level of each structure was defined in most cases after a visual inspection of the building performed by different teams of specialized professionals throughout the country [18][19][20].

Building characteristics such as location, year of construction, number of stories and damage level, are summarized in Table 2-1 for the database. Three general observations may be immediately inferred. First, Region VIII, including the city of Concepción, concentrates most of buildings with Damage Level III. Although Concepción is the closest city to the epicenter (Figure 2-1a)), the greatest energy release of the earthquake occurred further north at the latitude of the city of Curicó. Therefore, the concentration of damage in Concepción has to do with shaking intensity, but also with other local effects such as poor soil conditions, detailing in as built conditions, and possibly an unfavorable orientation of the buildings [18].

Second, data indicates that most of the damaged buildings are rather new structures. Figure 2-3a) illustrates that although most damaged buildings (Damage Level III) are broadly distributed by year of construction, most of the inventory was constructed after the year 2000. In fact, 78% of the inventory of damaged buildings was built after the year 2000, as compared to 70% for the total building inventory (Figure 2-3b)). The total building inventory considers a total of 2074 buildings of more than 9 stories located in the regions considered in this study (RM, V, and VIII), and was estimated using available national statistics from INE [21][22]. As of the date of the earthquake, there was a large proportion of medium to high-rise structures constructed before year 2000, which did not undergo as much damage as the newer structures. Thus, it is clear that the earthquake affected mainly relatively new structures.

Third, by looking at the distribution of damaged buildings by total number of stories N_t (including basements) (Figure 2-4a)), most buildings have range from 10 to 24 stories, with an average of 17 stories and a single one taller than 24 stories. Figure 2-4b) compares, by number of stories, the distribution of the total building inventory versus the damaged building inventory constructed in the period 2002-2009, since in that period data is available[1]. As it can be observed, the proportion of buildings in the range 10-14 and 15-19 stories is very similar, in both, the damaged and total inventories. However,

1 Total inventory of damaged buildings by number of stories estimated using internal statistics from the *Instituto del Cemento y Hormigón ICH,* 2011

there is a slight overrepresentation of damaged buildings in the range 20-24 floors (28%) as compared to the total building inventory (20%). Additionally, it is interesting to observe the low percentage of damaged buildings of more than 24 floors (4%). Taller buildings have generally longer periods and are founded in stiffer soils, which reduce their seismic demand. Additionally, taller buildings in Chile tend to present a slightly different structural layout than the fish-bone type [23], with the corresponding different behavior. Thus, it is clear that the earthquake affected mainly structures up to 24 stories, and the good performance observed in taller buildings can be attributed to several factors ranging from a different earthquake demand, slightly different structural typologies in plan, selection of better soils, and use (in one case) of different seismic protection technologies.

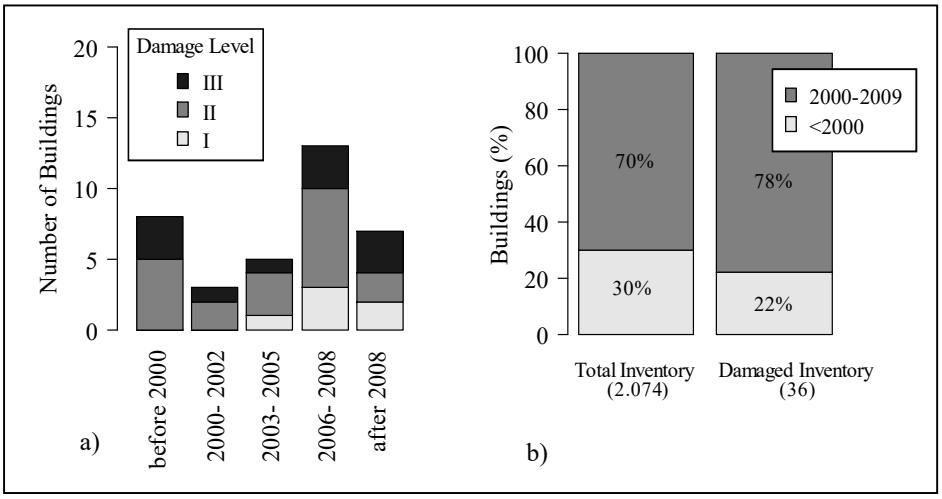

Figure 2-3. Distribution by year of construction: a) distribution of damaged buildings by damage level; b) comparison of total inventory versus damaged inventory.

Table 2-1. Inventory and properties of damaged buildings

Building ID	Region	Year of construction	Number of stories	Damage Level	Floor plan aspect ratio $\overline{b_l/b_t}$	Slenderness ratio $H/\overline{b_t}$	Total wall density $\bar{\rho}_l + \bar{\rho}_t$ (%)	Wall thickness (cm)
1	RM	2004	10+1	II	1.76	1.57	4.64	26
2	RM	2007	21+1	II	2.75	4.40	7.13	19
3	RM	2008	17+1	II	1.17	1.80	5.62	21
4	RM	2008	20+4	III	3.83	3.59	4.98	18
5	RM	2008	19+2	I	1.07	1.94	5.93	20
6	RM	2009	26+4	II	1.27	2.38	5.68	20
7	RM	2007	18+2	II	4.10	3.04	6.46	20
8	RM	2008	21+1	II	1.76	2.39	6.08	21
9	RM	2000	19+2	II	1.98	2.48	5.68	21
10	RM	2008	8+2	II	1.64	1.03	3.78	16
11	RM	2005	20+2	II	1.56	2.71	6.76	22
12	RM	2009	10+1	I	1.61	1.53	4.85	19
13	RM	2009	10+1	I	1.61	1.53	4.85	19
14	RM	2006	16+2	I	1.56	2.25	6.21	17
15	RM	2009	12+2	II	1.62	1.59	4.68	16
16	RM	2005	18+1	I	1.08	1.15	5.73	15
17	RM	2006	11+1	I	2.72	1.58	5.35	15
18	V	1999	16+1	II	1.44	2.10	5.46	20
19	V	1996	10+1	III	2.31	1.71	5.25	20
20	V	1974	14+1	III	1.68	1.32	6.01	28
21	V	2006	16+2	II	1.53	2.22	6.61	22
22	V	1988	15+2	II	2.29	2.78	4.44	23
23	V	1993	17+1	II	1.55	2.43	4.88	20
24	V	2000	11+1	II	2.57	2.24	6.26	20
25	V	1998	12+1	II	1.20	1.83	6.62	22
26	V	1997	11+1	II	2.21	2.48	5.53	20
27	VIII	2005	18+1	III	2.25	2.79	5.43	20
28	VIII	2001	20+1	III	1.19	2.37	6.60	19
29	VIII	2006	12+0	III	1.70	2.10	5.11	15
30	VIII	2009	21+2	III	1.82	2.83	5.15	24
31	VIII	1973	17+1	III	1.01	2.43	7.68	26
32	VIII	2009	15+2	III	2.54	2.82	6.83	20
33	VIII	2008	20+1	II	2.39	2.60	7.09	20
34	VIII	2009	15+2	III	1.32	1.71	5.07	20
35	VIII	2006	10+0	III	3.35	1.69	5.33	15
36	VIII	2004	10+0	II	3.35	1.69	5.33	15

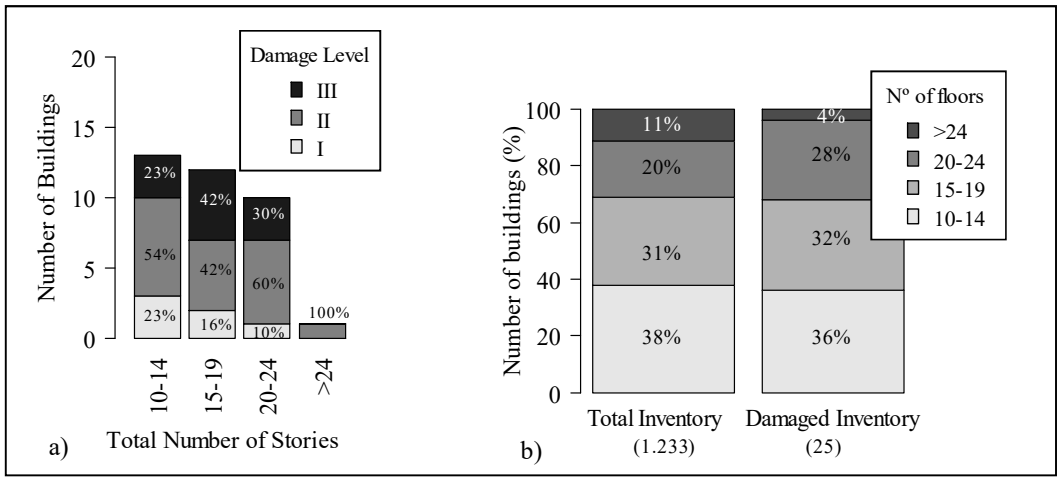

Figure 2-4. Distribution by number of stories: a) distribution by damage level; b) comparison of total buildings versus damaged buildings in the period 2002-2009.

As it has been discussed in previous work [19], damage to RC walls cannot be always traced back to an inappropriate structural design of the elements. Consequently, next sections concentrate on critical aspects that were omitted by official design codes at the time of the earthquake [10], in particular, the use of a minimum wall thickness, an upper bound for the axial stresses in walls, and limitations on the building plan and height irregularity.

2.3. Structural characteristics of damaged buildings

Five groups of structural characteristics or parameters were identified and obtained for each of the buildings: (i) geometric characteristics; (ii) material properties; (iii) dynamic parameters; (iv) wall-related parameters; and (v) irregularity indices. As possible, all characteristics of damaged buildings are compared with the general building inventory, which consists of a database of approximately 500 RC Chilean buildings that have been studied in the past [23][24][25], and for which some of the studied parameters are available. In addition to that, a small benchmark group of 7 essentially identical but undamaged buildings is included in order to compare in detail their parameters with those of the damaged buildings. Finally, a statistical analysis between the selected global building parameters and the damage level is also included.

2.3.1. Geometric characteristics

Figure 2-5a) shows the distribution of the average floor plan aspect ratio $\overline{b_l/b_t}$ for damaged buildings. This ratio is defined as the average for all stories (including basements) of the maximum longitudinal dimension of the floor plan $b_l = max(b_x, b_y)$ divided by the minimum transverse dimension of the floor plan $b_t = min(\ _x, b_y)$. The average floor aspect ratio varies between 1.0 and 4.1 with a mean value of 1.97 (Table 2-1). Figure 2-5b) shows the distribution of the slenderness ratio $H/\overline{b_t}$, where H is the total building height including basements, and $\overline{b_t} = min\ \overline{\ _x}, \overline{b_y})$ is the minimum of the average of the lateral dimensions of the floor plan along the building height. The damaged building inventory has an average slenderness ratio of 2.2, with values ranging from 1.0 to 4.4 (Table 2-1). Unfortunately, no information on floor plan aspect ratio or slenderness ratio is available for the general building inventory.

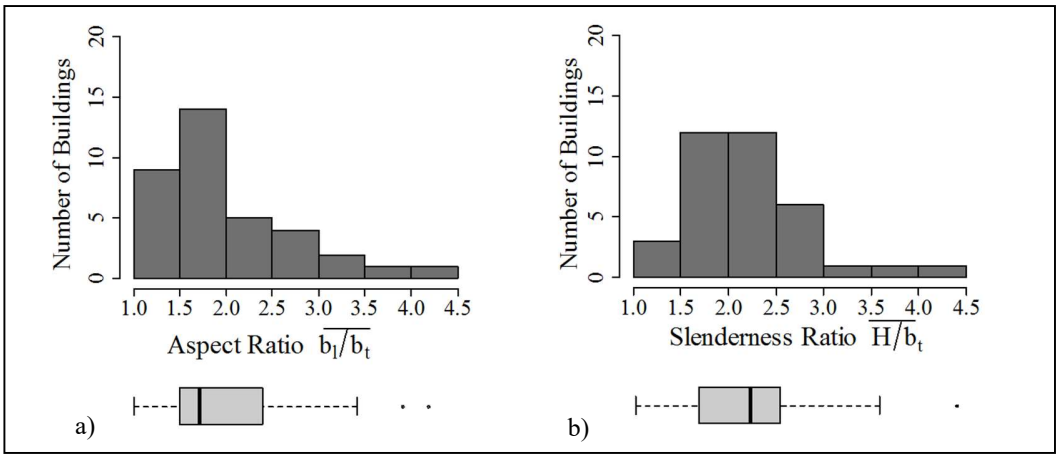

Figure 2-5. Building geometric characteristics: a) distribution of aspect ratio; and b) distribution of slenderness ratio.

2.3.2. Material properties

All the buildings considered in the inventory were nominally designed with steel A630-420H (f_y= 420 MPa), and using four different types of concrete cubic strength denomination H22.5, H25, H30 and H35, with characteristic concrete strength f_c' =19,

20, 25 and 30 MPa, respectively. Figure 2-6a) shows that most of the buildings (56%) were constructed using concrete H30. Although there is no available data on material properties for the general building inventory [24], a study of about 50 Chilean RC buildings [26] shows that A630-420H is the steel type used in all buildings studied, and concrete H30 is used in more than 70% of the cases.

Figure 2-6b) shows the distribution of the building inventory in terms of soil type and damage level. There are 8 cases without information on the soil type, and 4 cases where the information reported originally in the structural report is in contradiction with the soil type defined by studies conducted later. When more than one soil classification was available, the original information was considered. As shown in Figure 2-6b), damaged buildings with available data are founded in soils type II (stiff) or III (soft) according to the Chilean code [10].

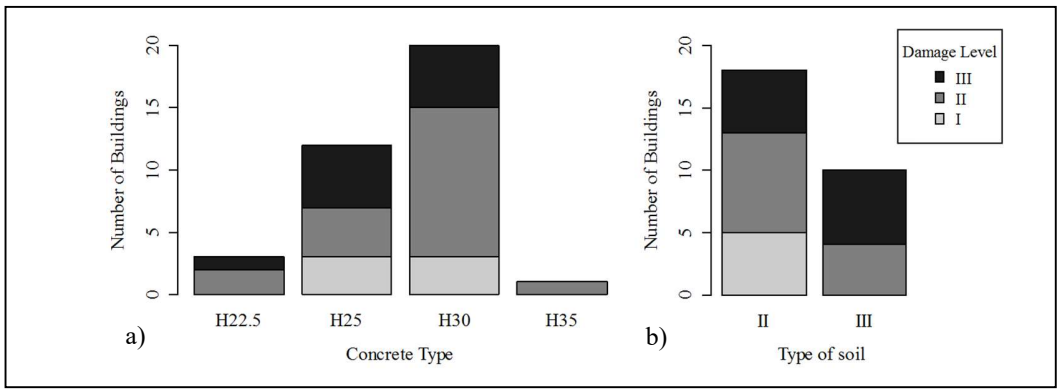

Figure 2-6. a) Distribution of concrete type by damage level; and b) distribution of soil type by damage level.

2.3.3 Dynamic parameters

The fundamental period of each building is obtained from a linear structural model when available (17 cases), and is calculated using the same assumptions commonly used in Chilean practice, which considers the gross section of structural elements, i.e. neglecting (i) the contribution of the slab in the stiffness of beams, (ii) the over-strength of steel and concrete, and (iii) the cracking of the structural elements. Periods are simply labels to identify each building, and as long as they are computed in the same way for all buildings,

this definition does not introduce a distortion on the interpretation of the sample. To estimate the period in buildings where no models exist, three methods were used. First, due to the rather good correlation of period and total number of stories N_t (Figure 2-7a)), the simple model $N_t/20$ is considered, as it has been used in the past with very good results for Chilean buildings [4][27]. Second, the ATC3-06 specifications are used [28], which estimates building period as $T = 0.05H/\sqrt{D}$, where H is the height of the building in feet above the base, and D is the dimension in feet of the building at its base in the direction under consideration. Finally, a linear regression of the available data from the linear models is proposed. All models work well (Figure 2-7a)), but naturally the linear regression using the available data from linear models is the one that better represents the sample data and is thus chosen to estimate the period for the rest of the damaged buildings. Thus, the distribution of the estimated periods of damaged buildings is shown in Figure 2-7b), where periods vary from 0.36 to 1.56 s., with a mean value of 0.77 s.

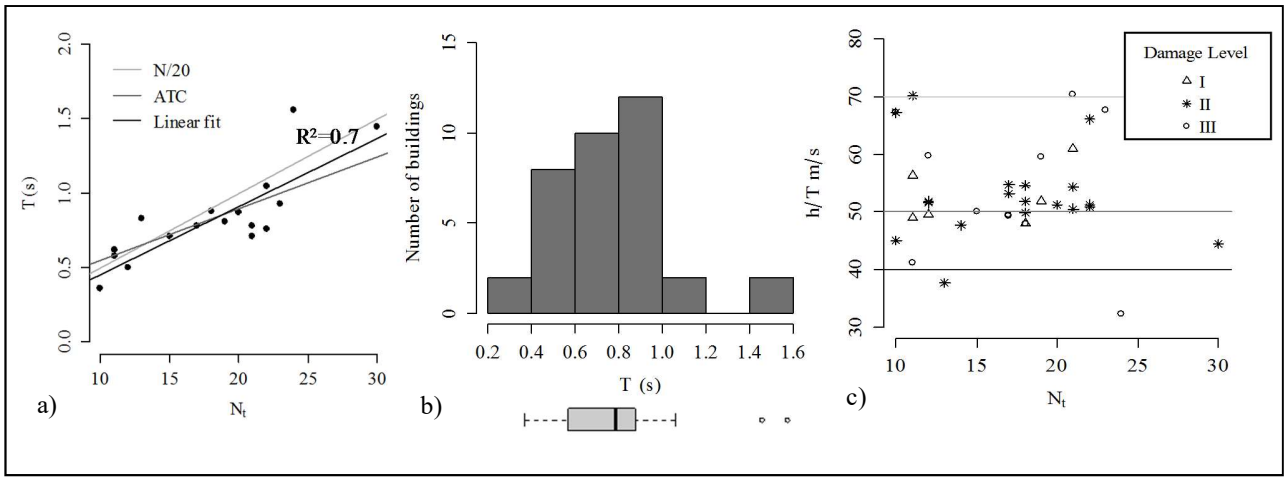

Figure 2-7. Building periods using data from building models: a) data fit; b) distribution of estimated periods; and c) dynamic parameter *h/T*.

The ratio *h/T* between the height of the building above ground level *h* and the fundamental building period *T* has been used in the past as a measure of the stiffness of buildings [7][8]. Buildings are classified as "very stiff" (*h/T*>150 m/s), "stiff" (70-150 m/s), "normal" (40-70 m/s), "flexible" (20-40 m/s), and "very flexible" (<20 m/s) [7]. Most damaged buildings have *h/T* in the ranges 40-70 m/s with a mean value of 53 m/s (Figure 2-7c)), which makes those structures be classified as "normal" in terms of this

parameter. The average *h/T* for the general building inventory is 77 m/s [24], which is higher than the average for the damaged buildings. However, the parameter for damaged buildings increases considerably when considering the total height of the building *H*. If such is the case, more structures are classified as "stiff", and the average value increases to 59 m/s. This is important to take into account considering that newer buildings tend to have more than one basement level, and hence, values *H* and *h* tend to be quite different.

Furthermore, past studies using shear wall buildings in Chile correlated the index *h /T* with the earthquake damage [29]. Expected damage could be "negligible" (*h/T*>70 m/s), "non-structural" (50-70 m/s), "light structural damage" (40-50 m/s), or "moderate structural damage" (30-40 m/s) [7]. Most damaged buildings have values above 40, suggesting that only light structural damage should be expected according to this simplified rule (Figure 2-7c)). If the total height of the building is considered, the situation is even more critical since most of the damaged buildings should have presented only non-structural damage, which empirically is incorrect. Whatever the building height considered, the observed damage after the earthquake was substantially more severe than predicted by this rule. Therefore, other global building parameters should be developed as predictors of expected damage.

2.3.4. Wall parameters

Field observations show that damage occurred mainly in RC walls localized in the first few stories and first basement, and it was of brittle nature in general. Therefore, special emphasis is given to the wall properties characterized through four parameters: wall thickness, wall density, wall density per weight (DNP)—inverse of the more physical weight per shear wall density in terms of plan area—and axial load ratio (*ALR*).

First, the distribution of the average wall thickness $\bar{e}$ is shown in Figure 2-8a) and values for each building are presented in Table 2-1. This parameter is calculated for each building as the average wall thickness in all stories. The average wall thickness in each story is computed as a wall-length weighted average $e = \sum_1^m e_i\, l_i / \sum_1^m l_i$, where e_i is the thickness of the i-th wall, l_i is its length, and m is the number of walls per story. Wall

thickness varies from 15 to 28 cm with a mean value of 19.9 cm (Figure 2-8a)). The distribution is skewed toward smaller values, with 22% of the inventory presenting wall thickness lower than 18 cm, and 69% of the building inventory presenting values lower than 21 cm (Figure 2-8b)). This average wall thickness is very small if compared with the wall thicknesses of the well-behaved buildings in Viña del Mar during the 1985, Chile earthquake, which ranged between 30 and 50 cm [5]. Buildings at that time where based on Chilean codes that required a minimum wall thickness of 20 cm [5][30]. This is critically important since ductility of the walls is controlled by concrete section and axial stresses. Also, thinner walls are very sensitive to proper execution and in-situ detailing during construction. Although there is no available data on the wall thickness for the general building inventory [24], a study of about 50 Chilean RC buildings [26] shows that 58% of the walls have thickness of 20 cm, followed by 18% with thickness 25 cm, and only 12% of the cases presenting wall thickness below 20 cm. It can be inferred from this study that the average wall thickness is 22 cm, which is larger than the average thickness of the damaged buildings.

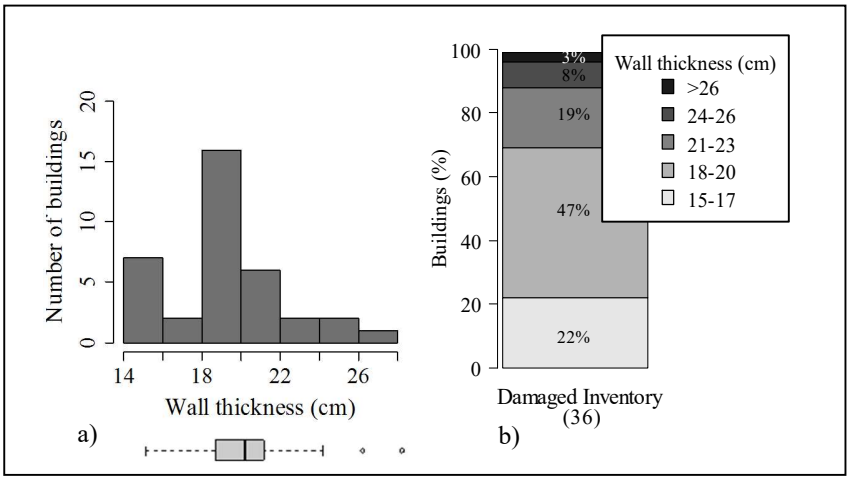

Figure 2-8. a) Distribution of average wall thicknesses in damaged buildings; and b) as a percentage with base on the damaged buildings.

Second, shear wall density is defined as the ratio between the wall section area and the floor plan area, and is calculated for each floor and for each principal direction of the building. The results presented herein refer to the average of all floors (including

basements). Total values of wall densities are presented in Table 2-1. Figure 2-9 shows the distribution of wall densities for the longitudinal ($\bar{\rho}_l$) and transverse ($\bar{\rho}_t$) directions, which have mean values of 2.8% and 2.9%, respectively. These mean values are similar to the general building inventory [5][23][24], where mean values of 2.7% and 2.9% have been reported for the longitudinal and transverse directions respectively (for typical story). This indicates that damaged buildings exhibit typical wall densities in either direction, and that this density is similar to that of other undamaged buildings. However, though these buildings have similar wall densities than buildings in 1985, they are taller, and hence subjected to larger axial compression stresses. Therefore, and based on basic considerations of RC section analysis, these taller buildings presented a less ductile behavior; an effect that was not incorporated in Chilean code provisions at the time [9][10].

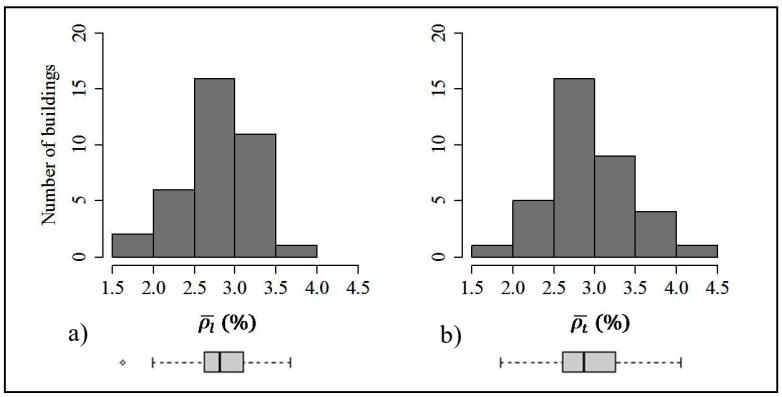

Figure 2-9. Wall density distribution of damaged buildings: a) longitudinal direction; and b) transverse direction.

Third, the wall density over the weight of the building above the level considered, or DNP parameter is presented. This parameter has been selected because it has been used in previous studies of Chilean buildings [23][24][25] and reference values of this index are available. In previous studies this parameter is defined as $DNP = \rho_z / (N \cdot w)$, where ρ_z is the total wall density in a given story, N the number of stories above the level considered, and w the floor weight per unit area. In the present study, the DNP is computed more precisely as the wall area of the first story divided by the weight W of the building above that story, and is calculated for both, the longitudinal and transverse

directions. The total weight W considers the dead load plus 25% of the live load (D+0.25L), where D considers the weight of all structural elements, as well as the self-weight of non-structural elements assumed as 1.47 kPa in each story; and L was considered as 0.16 kPa in each story. These values lead to an average unit weight per floor of w=9.12 kPa, slightly smaller than the average unit weight per floor w=9.81 kPa used elsewhere [12]. As it can be observed in Figure 2-10, the distribution of DNP has mean values of 0.21 and 0.23x10^{-3} m^2/kN for the longitudinal and transverse directions, respectively, values that are similar to the average value reported for the general building inventory of about 0.2x10^{-3} m^2/kN [23][24][25]. However, this parameter has decreased to almost half in the period between 1939 and 2007 [23][24][25], which implies a 100% increase in the average axial compression in walls during that period [31]. Historically, the smallest value for the DNP parameter in Chilean buildings was about 0.1x10^{-3} m^2/kN and resulted in an adequate earthquake behavior of RC walls [31]. However, the same smallest value was observed in the 2010 inventory of damaged buildings, and hence it is not sufficient to guarantee an adequate behavior of RC walls.

Finally, the average ALR at the first floor ($\overline{ALR}^1$) is calculated as the quotient $W/(A_w f_c')$, where W is the total weight of the structure above and including the first story; A_w is the total area of vertical structural elements at the first-story (including columns); and f_c' is the characteristic concrete strength used in the building. This ratio is usually expressed as a percentage (%). Figure 2-11a) shows the distribution of $\overline{ALR}^1$ for the damaged buildings, which ranges between 6% and 16%, and has a mean value of 10.4%, which corresponds to an average gravity axial stress of 2,39 MPa. This value is relatively high specially considering three additional factors: i) the localized increase of $\overline{ALR}$ in basement levels due to the vertical irregularities in walls; ii) the increase of $\overline{ALR}$ due to seismic actions; and iii) the distribution of ALRs among walls.

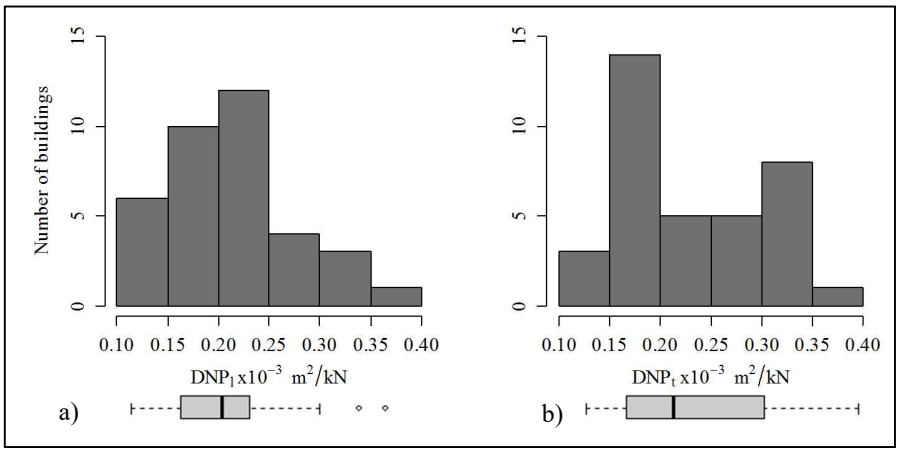

Figure 2-10. DNP parameter distribution in damaged buildings: a) longitudinal direction; and b) transverse direction.

Figure 2-11b) shows that $\overline{ALR}^1$ somewhat positively correlates with the number of stories above ground level (N_a). The figure also shows in dashed line the estimation of the average *ALR* for the first floor ($\overline{ALR}^{1*}$) presented elsewhere [13], which is a linear function of the number of stories and was calculated considering the stories above ground level assuming a unit weight for the floor w=9.81 kPa, a ratio of vertical elements over floor plan, A_w/A_f , of 6%, and a concrete strength f_c'=25MPa. These three values are similar to the average values of the presented inventory of damaged buildings. It is apparent that $\overline{ALR}^{1*}$ is a reasonable estimator of the *ALR* of the damaged buildings; however, this estimation naturally improves by using the real wall density and concrete strength of each building.

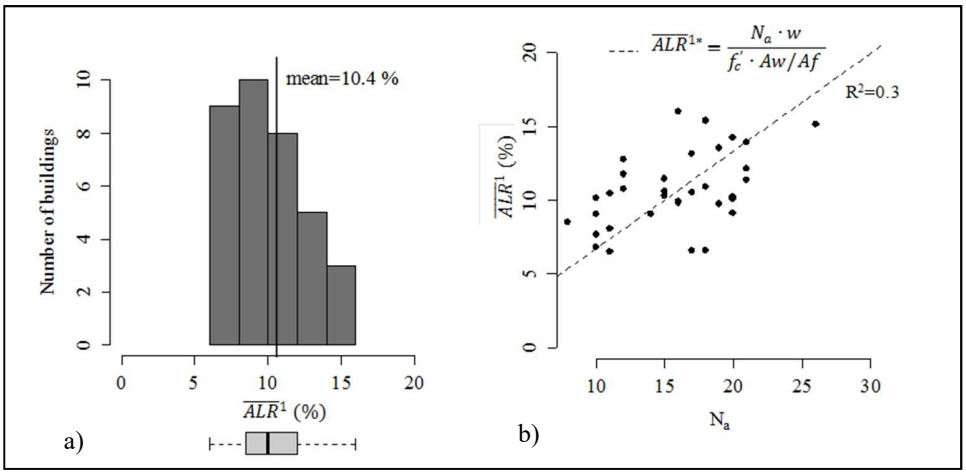

Figure 2-11. Variation of $\overline{ALR}^1$ in damaged buildings: a) histogram; and b) variation of $\overline{ALR}^1$ versus number of stories above ground level.

Although poorly-detailed wall boundaries has shown to be related to the observed damage [4][19], experimental results on typical Chilean RC wall buildings presented elsewhere [32][33] show that the most apparent effect of well confined boundary elements is to prevent, after occurrence of the in-plane rupture of the wall, its out-of-plane buckling and vertical instability, which is critical to preserve the load path of the vertical loads carried to the ground by the resisting plane. However, in terms of improving the in-plane bending and compression behavior of the wall, the boundary confinement does not lead to a noticeable improvement in strength or ductility, as it does an increase in the wall cross section, by increasing wall thickness or reducing axial stresses, which contribute more significantly to improve the cyclic behavior of these brittle elements.

2.3.5. Irregularity indices

Most damaged buildings show abrupt changes and irregularities in the transition between the basement and the first stories, or in their first stories. Thus, three irregularity indices are proposed and evaluated next. The first one is the ratio of average floor plan area of all levels above ground level ($\overline{A_a}$) relative to the average floor plan area of all levels below ground level ($\overline{A_b}$), defined as $\overline{A_a}/\overline{A_b}$. The average $\overline{A_a}/\overline{A_b}$ ratio for the inventory of

damaged buildings is 66% (Figure 2-12a)), which is due to the large increase in floor plan area of the basements.

This increase in plan surface also occurs with an increase in the shear wall area at the basements, which implies that the average wall density below ground level ($\overline{\rho_b}$) may be similar to that above ground level ($\overline{\rho_a}$). The second irregularity index, defined as the average $\overline{\rho_a}/\overline{\rho_b}$ is 97%, and it is shown in Figure 2-12b). Please note that $\overline{\rho_a}$ is calculated as the average wall density of all levels above ground level, while $\overline{\rho_b}$ is calculated as the average wall density of all levels below ground level. This ratio of 97% is difficult to interpret since the distribution of walls in the basements differs in general from that of first story walls. This occurs due to the basement requirements of vehicle circulations and parking spaces, the existence of perimeter walls, and changes in the core walls to ensure proper circulation.

The preceding discussion justifies the definition of an irregularity index, i.e. the wall area ratio WA_{s1}/WA_1, where WA_{s1} is the plan area of shear walls in the first-story that have continuity into the first basement, and WA_1 is the total first-story shear wall area (Figure 2-12c)). The wall area ratio is on average 82%, which means that 82% of the walls in the first story have continuity into the first basement. This implies that average axial stresses in the core walls of the first basement are about, and as a result of this effect, 22% higher than those in the first-story walls. The average *ALR* of the first basement ($\overline{ALR}^{s1}$), which includes this irregularity effect, increases to 12.7%, which compares with the previous value of 10.4% (Figure 2-12a)). Therefore, walls located in the basement present higher axial stresses, especially if the resisting plane exhibits an important vertical discontinuity. Similarly, because buildings lack beams in general, the critical wall section for checking the bending moment and compression design is always below the slab level, where the section of the wall is reduced. This fact may have contributed to the observed brittle failure mode of walls at the basement [4][18][19]. Unfortunately, there is no data available on irregularity indices for the general building inventory.

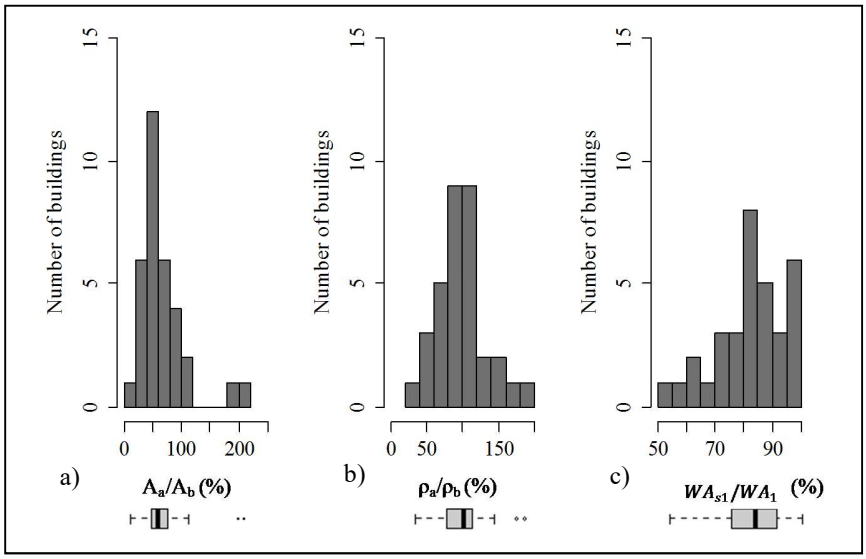

Figure 2-12. Histogram of vertical irregularity indices: a) area ratio $\overline{A_a}/\overline{A_b}$; b) wall density ratio $\overline{\rho_a}/\overline{\rho_b}$; and c) core wall area ratio WA_{s1}/WA_1.

2.3.6 Characteristics of undamaged buildings

A control group of 7 undamaged buildings located in the same regions affected by the earthquake was selected in order to find out if the parameters of damaged buildings differ or not from those of undamaged buildings. The 7 undamaged benchmark buildings were obtained from three well known different structural engineering offices, which had designed very similar structures that in some cases underwent the same type of structural damage considered herein. The RC buildings selected satisfied the following criteria, i.e.: (i) they were located in Santiago, Viña del Mar, and Concepcion; (ii) they were built after the year 2000; (iii) had the same typology of shear walls in plan and height; and (iv) had 10 or more stories. The engineering offices provided all the structural drawings and design information of these undamaged buildings that they considered completely analogous to the buildings that experienced damage during the earthquake. Of the sample, 5 buildings were selected in the RM region (Santiago), 1 building in Region V (Viña del Mar), and one building in Region VIII (Concepción).

Table 2-2 shows general information, geometric characteristics and material properties of undamaged buildings, and includes for comparison average values for the inventory

of damaged buildings. Their number of stories ranges between 17 and 29 including basements, with an average of 25 stories, which is larger than the average height of damaged buildings. This has an implication on the earthquake demand, but otherwise the structures are similar and indices are comparable. Undamaged buildings have floor plan aspect ratios ($\overline{b_l/b_t}$), varying between 1.12 and 2.63 with an average of 1.82, which is comparable to the values of the damaged inventory. The slenderness ratio ($H/\overline{b_t}$) varies between 1.81 and 4.27 with an average value of 2.77, slightly larger than the average for damaged buildings. On the one hand, all undamaged buildings are constructed using steel type A630-420H and concrete type H30, with the exception of building 7 which uses H25. On the other hand, all buildings are located in soil type II, only with the exception of building 3, which is in a softer soil (soil type III).

Table 2-2. General characteristics, material properties and geometric characteristics of selected undamaged buildings

				Geometric characteristics		Material properties	
Building ID	Region	Year of construction	Number of stories (Above grade+ below grade)	Floor plan aspect ratio $\overline{b_l/b_t}$	Slenderness ratio $H/\overline{b_t}$	Concrete Type	Soil Type
1	RM	2008	24+3	1.12	2.64	H30	II
2	RM	2008	27+2	2.42	4.27	H30	II
3	RM	2007	23+2	1.34	2.76	H30	III
4	RM	2006	15+2	2.63	1.81	H30	II
5	RM	2003	18+3	1.42	2.31	H30	II
6	V	2004	28+1	1.45	2.60	H30	II
7	VIII	2008	21+2	2.32	3.03	H25	II
Average Undamaged Buildings			**25**	**1.82**	**2.77**		
Average Damaged Buildings			**17**	**1.97**	**2.20**		

Dynamic characteristics, wall-related parameters, and irregularity indices for undamaged buildings are shown in Table 2-3. It is apparent that the selected undamaged buildings are in general more flexible than the damaged ones; the average period is 1.45s, which is about twice the mean of 0.77s for damaged buildings. The height to period parameter *h/T* ranges from 28 to 54 m/s, which means that the structures can be classified as normal to flexible [7]; their *h/T* values are in general smaller than that of damaged buildings. Wall thicknesses vary from 17 to 23 cm, and have a mean value of 21 cm, which is larger than the average value for damaged buildings (≈20cm). Wall densities $\bar{\rho}_t$

and $\overline{\boldsymbol{\rho_t}}$ for undamaged buildings are very similar to those of damaged buildings, with mean values of 2.7% and 2.6% in the longitudinal and transversal directions, respectively. These values are also similar to the average of 2.8% of Chilean buildings [23][24] . Additionally, the wall density per weight (DNP parameter) in the first story has mean values of 0.17 and 0.16 x10^{-3} m2/kN in the longitudinal and transversal directions, respectively. These values are smaller than the 0.21 and 0.23x10^{-3} m2/kN of damaged buildings, which was expected since these buildings are taller and newer, and this value has kept decreasing over the years [23][24][25]. The average axial load ratio in the first story $\overline{\boldsymbol{ALR}}^{\mathbf{1}}$ is on average 12.9%, larger than the average for damaged buildings.

Table 2-3. Dynamic characteristics, wall-related parameters and irregularity indices of selected undamaged buildings

	Dynamic characteristics			Wall characteristics						Irregularity Indices		
Building ID	**T (s)**	H/T (m/s)	h/T (m/s)	**Wall thickness e (cm)**	**Wall density** $\bar{\rho}_l$ (%)	**Wall density** $\bar{\rho}_t$ (%)	**DNP_l x10^{-3} (m^2/kN)**	**DNP_t x10^{-3} (m^2/kN)**	$\overline{ALR}^1$ (%)	$\overline{A_a}/\overline{A_b}$ (%)	$\overline{\rho_a}/\overline{\rho_b}$ (%)	WA_1/WA_{s1} (%)
1	1.30	53	46	20	3.22	2.91	0.13	0.16	13.9	41	134	71
2	1.84	40	37	23	3.59	3.59	0.14	0.15	13.6	104	55	100
3	1.08	59	53	19	2.25	2.59	0.14	0.11	16.1	30	142	79
4	1.19	37	32	17	1.57	1.38	0.23	0.20	9.2	38	94	73
5	0.85	64	54	22	3.08	2.96	0.18	0.14	12.2	60	74	87
6	1.88	37	35	22	2.60	2.26	0.19	0.14	12.1	53	77	98
7	2.00	30	28	22	3.18	3.47	0.16	0.22	12.9	41	121	74
Average U	**1.45**	**46**	**41**	**21**	**2.78**	**2.74**	**0.17**	**0.16**	**12.9**	**52**	**100**	**83**
Average D	**0.77**	**59**	**53**	**19.9**	**2.80**	**2.90**	**0.21**	**0.23**	**10.4**	**66**	**97**	**82**

Table 2-3 shows that undamaged buildings also present irregularities at ground level. The plan area ratio above and below ground level $\overline{A_a}/\overline{A_b}$ has a mean value of 52%, but values range between 30% to 104%, thus showing a great dispersion. The mean value of the ratio of wall densities $\overline{\rho_a}/\overline{\rho_b}$ is 100% and also shows great dispersion. Finally, the ratio WA_1/WA_{s1} ranges between 71% and 100% with mean value 83%, similar to the mean value of 82% of damaged buildings.

Most of the analyzed properties of undamaged buildings are very similar to those of damaged buildings, which suggests that damage cannot be explained by a single parameter. This result may also suggest that the observed damage in RC walls may have been brittle and having no damage during the earthquake of 2010 does not necessarily

mean great ductile behavior of the walls during a future earthquake. Structural safety of existing shear wall buildings may need to be considered on case-to-case basis.

2.3.7 Factors determining building damage

The association between building damage level and global building parameters was explored. A first, simple univariate descriptive analysis is shown in Figure 2-13). As it has been already discussed, buildings with no-damage are taller than damaged buildings (Figure 2-13a)). The stiffness parameter *h/T* has apparently no significant association with damage level in this case (Figure 2-13b), in contrast to results presented elsewhere [8][29]. On the other hand, Figures 2-13c) and 13d) show that excluding undamaged buildings (Damage Level 0), there is a positive correlation between damage level and the floor plan aspect ratio $\overline{b_l/b_t}$, and slenderness ratio $H/\bar{b}_t$. Larger values of building slenderness lead in general to larger overturning moments, and larger dynamic axial loads, which played an important role in building damage. Finally, Figure 2-13e) shows that wall area irregularity index WA_{s1}/WA_1 has no significant association with damage level, while Figure 2-13f) suggests a small negative association of axial load ratio in first story ALR^1 with damage level. This statistical result is contrary to what it would be expected, since one would expect that buildings with the highest ALR^1 were the most severely damaged ones. However, buildings with high ALR^1 are located mainly in RM region (Figure 2-14a)) and are clearly placed in better foundation soils (soil type II, Figure 2-14b)), which would help to explain why these buildings presented lower damage levels. On the contrary, buildings with low ALR^1 are located mainly in Regions V and VIII and are placed in soft soils (soil type III), which would explain their higher damage level. These observations suggest that damage level is strongly correlated with the variables *Region* and *Soil type*, as can be inferred from Table 2-4.

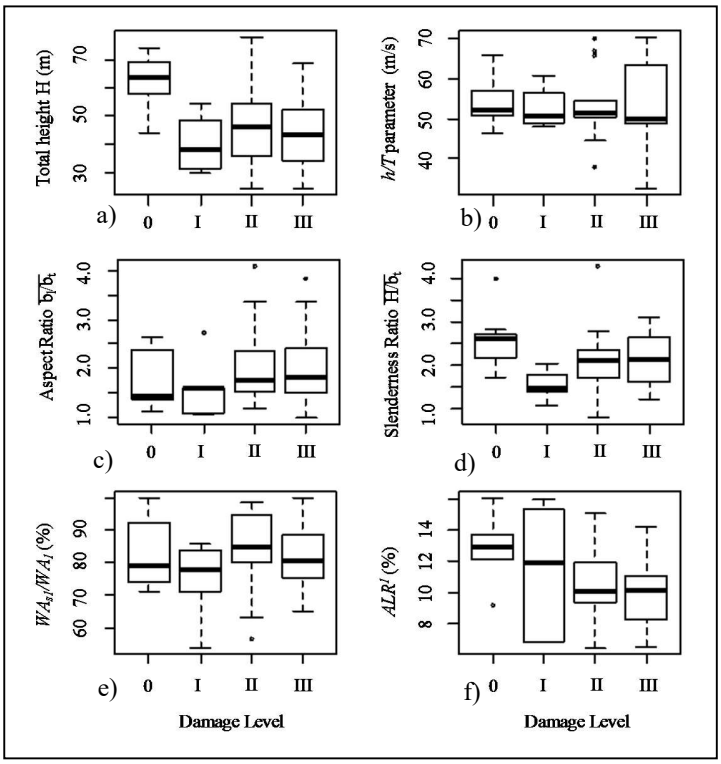

Figure 2-13. Box plots of building parameters by damage level: a) total height; b) stiffness ratio *h/T*; c) floor plan aspect ratio $\overline{b_l/b_t}$; d) slenderness ratio $H/\overline{b_t}$; e) wall irregularity index WA_{s1}/WA_1; and f) axial load ratio ALR^l.

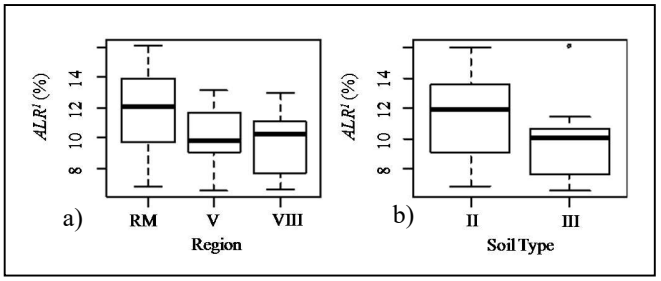

Figure 2-14. a) ALR^l versus region; and b) ALR^l versus soil type.

Table 2-4: Number of buildings by damage level, soil type, and Region number

Damage Level	Soil Type	Region			Total
		RM	V	VIII	
0-No Damage	NA				
	II	4	1	1	**6**
	III	1			**1**
I-Light	NA	1			**1**
	II	5			**5**
	III				
II-Moderate	NA	3	4		**7**
	II	5	3		**8**
	III	2		2	**4**
III-Severe	NA				
	II	1	2	2	**5**
	III			6	**6**
Total		**22**	**10**	**11**	**43**

Logistic regression models are usually used to disentangle the effect of different variables on a discrete response variable. Since in this case the response variable (damage level) is ordinal, *proportional odds logistic regression models* (POLR) [34] were used. The models were adjusted using the *polr* function of the *R*-statistical language [35]. This model assumes that the ratio of the odds for successive categories (i.e. I to II, or II to III) is constant. Application of this type of model is appropriate in this case since the damage level categories are discrete divisions of an unobservable, continuous *damage* variable.

Results considering univariate models for each independent variable are shown in Table 2-5a). Results show that the most significant variables are *Region* and *Soil type*, followed by total height, axial load ratio, and density irregularity index, which present negative correlation. Finally, the period of the building and floor plan aspect ratio also has some degree of significance, but the rest of the parameters seem less significant. The variable *Region* is probably the best proxy for ground motion intensity, and *Soil type* also contributes to the ground motion at the building site. Unfortunately, no precise assessments of ground motions are available for each building. If so, the models would probably be much more precise in determining damage levels.

Because the negative coefficient for the axial load ratio in story 1 is contrary to what common sense would dictate, this may suggest the need to consider more than one variable through multivariate models. In order to interpret the results, a series of multivariate POLR models were performed, where the damage level was explained in terms of *Region*, *Soil type* and *X*, i.e., isolating the effect of the most significant variables *Region* and *Soil type* (Table 2-5b)). In this case, the only significant variables are the stiffness ratio *h/T* and the building height H. The other variables do not seem to be very significant when included in a model together with *Region* and *Soil type*.

Table 2-5: Proportional ordinal logistic regression models: a) univariate; b) multivariate

a)

Damage Level~X		
Variable X	**Coefficient**	**p-value**
Region RM	0 (reference)	-
Region V	1.57	0.02
Region VIII	3.66	0.00
Soil Type II	0 (reference)	-
Soil Type III	1.62	0.02
Total height (m)	-0.04	0.03
ALR^1 (%)	-19.05	0.04
ρ_a/ρ_b (%)	-1.54	0.04
Period T (s)	-1.47	0.10
Aspect ratio	0.45	0.12

b)

Damage level~region+soil type+X		
Variable X	**Coefficient**	**p-value**
Region V	1.56	0.05
Region VIII	3.72	0.00
Soil Type III	1.06	0.16
h/T (m/s)	-0.11	0.02
Region V	1.26	0.10
Region VIII	2.82	0.01
Soil Type III	0.47	0.31
Total height (m)	-0.04	0.08
Region V	1.66	0.04
Region VIII	2.73	0.01
Soil Type III	0.61	0.26
Aspect ratio $\overline{b_l/b_t}$	0.33	0.22
Region V	1.50	0.06
Region VIII	2.94	0.00
Soil Type III	0.47	0.31
Slenderness Ratio $\overline{H/b_t}$	-0.30	0.31

Figures 2-15a), b) and c) show the probability of the different damage levels in terms of the stiffness ratio *h/T* for regions VIII, V, and RM, respectively. Results shown correspond to soil type III, and a particular value of height that in this case has been set to 54 m. It is shown that the main determinant of the probability for damage level is *Region*. Although the stiffness ratio modifies the probabilities, the effect of the former is much bigger. Figure 2-15a) shows that the probability of presenting damage "III-Severe" is higher in Region VIII, and decreases with stiffness ratio. Looking to Figures 2-15b) and c), it is clear that the probability of presenting "III-Severe" damage decreases as regions are farther from the epicenter. On the contrary, the probability of presenting

I-Light damage or 0-No damage is almost negligible in VIII Region (Figure 2-15a)), while it increases as we move right with the regions, and clearly increases with the stiffness ratio. Meanwhile, the probability of presenting II-Moderate damage increases from Regions VIII to V, but decreases again in Region RM. The trends observed in Figure 2-15 let us observe that the probability of presenting damage increases with the stiffness ratio for low level of damage, but decreases with stiffness ratio when the expected damage is high.

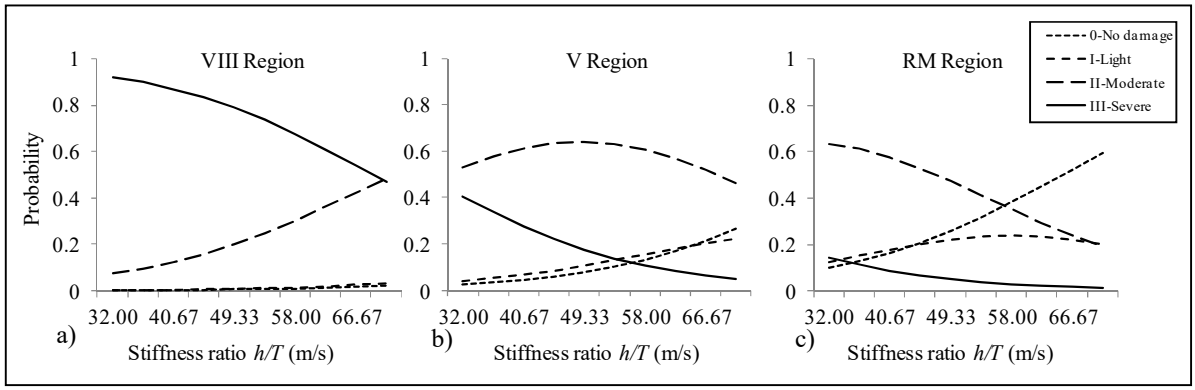

Figure 2-15. Damage probability in terms of stiffness ratio: a) VIII region; b) V region; and c) RM Region.

The statistical analysis presented in this section shows that the most significant variables in explaining the observed damage level for the selected sample are *Region* and *Soil type*, while the rest of the parameters do not seem to present high correlation with damage level. However, there are three aspects to consider when interpreting these results. First, this statistical analysis assumes a rather course granularity of data regarding building damage and, hence represents one more piece of data for the assessment, and it cannot be considered as unequivocal. Second, the category classification of damage is also uncertain, it represents only the habitability condition of the building, and it is not a precise measurement of the structural damage by element. Finally, as discussed in previous sections, the inventory of damaged buildings as whole show very particular characteristics —such as thin walls and high *ALRs*— that have been related to observed damage by field observations as well as experimental results [4][13][12][32]. Although

the statistical model captures the main variables *Region* and *Soil type*, it is unable to capture these more specific effects.

2.4. Axial load ratio analysis in damaged buildings

Because experiments have shown the importance of the axial load ratios (*ALR*) of the RC walls in controlling the damage of shear walls, this section focuses on it, and considers, both, the static and dynamic effects. First, *ALR* due to seismic actions are calculated and analyzed by a case-study building. Second, the same analytical procedure is followed by three more buildings. Finally, a simple procedure to estimate dynamic amplification factor for the average *ALR* is presented.

2.4.1 Dynamic axial load ratio

The axial load ratio $ALR_i^j(t)$ of wall "*i*" at story "*j*" is defined next in Eq. 2-1

$$ALR_i^j(t) = \frac{N_i^j(t)}{Ag_i^j \cdot f_c'} \qquad \text{Eq.2-1}$$

where $N_i^j(t) = (N_i^j)_S + (N_i^j(t))_D$ is the axial load of the wall decomposed in its static (S) and dynamic (D) effect; Ag_i^j is the gross area of wall; and f_c' is the specified characteristic concrete strength of the building.

Analogously, the *ALR* of wall "*i*" can also be expressed in terms of static and dynamic components as $ALR_i^j(t) = (ALR_i^j)_S + (ALR_i^j(t))_D$. For simplicity, these variables will be redefined as $X_T = X_S + X_D$, where $X_T = ALR_i^j$ is the *ALR* of wall "*i*" at story "*j*"; and sub-indices *T*, *S* and *D* refer hereafter to total, static, and dynamic components. The maximum value of the *ALR* in time can be calculated as $max(X_T) = |X_S| + max(X_D)$. We assume without loss of generality that X_S is positive, and define the amplification factor *AF* as the ratio between the maximum total axial load ratio $max(X_T)$ and the static axial load ratio X_S (Eq 2-2).

$$AF = \frac{max(X_T)}{X_S} = 1 + \frac{max(X_D)}{X_S} \qquad \text{Eq.2-2}$$

where we redefine $max(X_D)/X_S = \alpha$. The maximum $max(X_D)$ may be estimated using the peak factor definition given by Davenport [36], i.e. $max(X_D) = p \cdot \sigma_{X_D}$, where p is the peak factor and σ_{X_D} is the standard deviation of X_D. Therefore, factor α can be expressed as $\alpha = p \cdot s$, where $s = \sigma_{X_D}/X_S$. Thus, if we have an estimation of either the pair (p,s), or α, for a particular wall or group of walls, we are able to estimate the amplification factor AF, which is a measure of the total amplification of the static axial load ratio due to dynamic effects. In the following, these parameters will be analyzed for a case-study building, and then will be extended to the response of other shear wall buildings subjected to different ground motion inputs.

Linear behavior of buildings is assumed in this section since the observed building damage was essentially brittle and localized, and hence, inelasticity in these structures was presumably small. Buildings probably maintained a predominantly elastic behavior until they reached brittle failure in some of the walls, as has been proved recently by a step-by-step nonlinear brittle analysis of one of these structures [37]. Additionally, damage occurred in very few cycles as demonstrated by cyclic experiments recently finished [33]. Thus, the assumption of a predominantly linear behavior is adequate for this study.

Detailed results for damaged building 7 (Table 2-1) are analyzed and presented next. This building is composed of two different blocks separated by a construction joint; indices "a" and "b" denote each of the blocks. Results presented correspond to a dynamic finite element linear model of block "b" developed using ETABS [38]. The static analysis case (S) includes dead loads plus 25% of live loads; and the dynamic case (D) considers a unidirectional time-history analysis for four different ground motions (Table 2-6) with components X- and Y- analyzed independently. Each ground motion record is normalized by a factor f such that the pseudo-acceleration at the fundamental building period equals a pre-established reference value A_b, which for the sake of this study has been set arbitrarily to $0.2g$. This factor is different in each direction of analysis and is calculated as $f_{x,y} = 0.2g/S_A(T_{x,y})$ (Table 2-6). Moreover, the significant duration of the ground motion in seconds is defined using the Arias Intensity I_A [39] between 5%I_A and

95%I_A (Table 2-6). The first pair of ground motions (D1 and D2) corresponds to the two closest seismic records (Santiago-Peñalolen and Santiago Centro) registered during the 2010 earthquake [40], where the corresponding horizontal component is used for each direction of the building. The second pair of ground motions (D3 and D4) corresponds to two artificial records compatible with the elastic design spectrum defined by the Chilean Seismic Code [10] for soil type II and seismic zone 2. The only difference between the X- and Y- components of these latter two seismic records is their normalizing factor f (Table 2-6).

Table 2-6. Dynamic cases considered for analysis of Building 7b

Dynamic Case	Seismic Record	Significant duration (s)	f_x	f_y
D1	Santiago Peñalolén	34	0.39	0.75
D2	Santiago Centro	34	0.23	0.68
D3	Compatible 1 Soil II, Zone 2	39	0.36	0.7
D4	Compatible 2 Soil II, Zone 2	40	0.4	0.72

Because similar results are obtained in both directions, results for the analysis in the Y-direction of the building are presented next. Shown in Figure 2-16a) are the Y-component of each normalized seismic record, and in Figure 2-16b) the corresponding response spectrum including the fundamental period of the building in the direction of analysis. Let us consider first results for individual walls. A schematic view of floor plan of the first basement of building 7b is shown in Figure 2-17a), where walls Q.01and N.02 are selected to illustrate the results of time-history analysis for the D1-Y case (Figure 2-16a)). Figures 2-17b) and c) show the static (S) and dynamic (D) components of the *ALR* for both walls. In the case of Wall Q.01 (Figure 2-17b)), the static component is18.4%, while the total *ALR* reaches a peak of 40.9%. In the case of wall N.02 (Figure 2-17c)) the static component is 16.9% and the peak total *ALR* is 42.6%. If the original input is considered (i.e., without the scale factor defined in Table 2-6), the total peak *ALR* for each wall is 48.3% and 51.1% for walls Q.01 and N.02, respectively. These values are large, especially if we consider the limit of 35% for ultimate loads included in current Chilean seismic code [14].

Results for all walls of the first basement of the building are presented in Figure 2-18. It is important to consider that only the elements with length-to-width ratio greater than 4 [41] are selected, and perimeter walls in the basement levels have been ignored. Figure 2-18a) shows the distribution of the static component for individual walls, which has a mean value $\overline{X_S}$=10.75%. Part b) of the Figure shows the distribution of the maximum of the dynamic component for individual walls, which has mean value $\overline{max(X_D)}$ =10.76%. This leads to a total mean value $\overline{max(X_T)}$ = 21.51% (Figure 2-18c)), i.e., an average amplification factor *AF*=2.1. If the original input is considered, i.e. D1-Y with f_y=1, these values increase to $\overline{max(X_D)}$ =14.5% and $\overline{max(X_T)}$ = 25.1% Additionally, a single wall can present values as high as $max(X_D)_i$ =38.4%, which for the original input increases to 51.2%

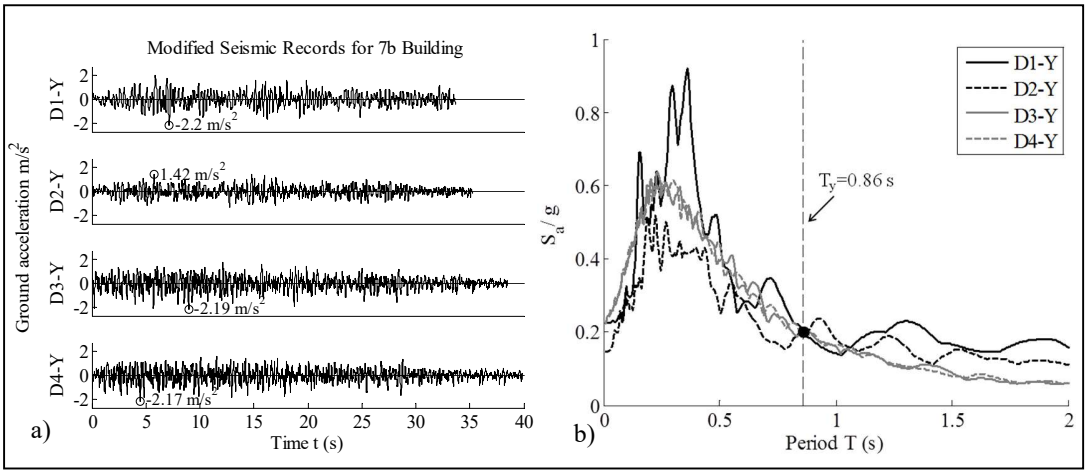

Figure 2-16. Building input: a) Y-component of the seismic records; and b) pseudo-acceleration spectrum.

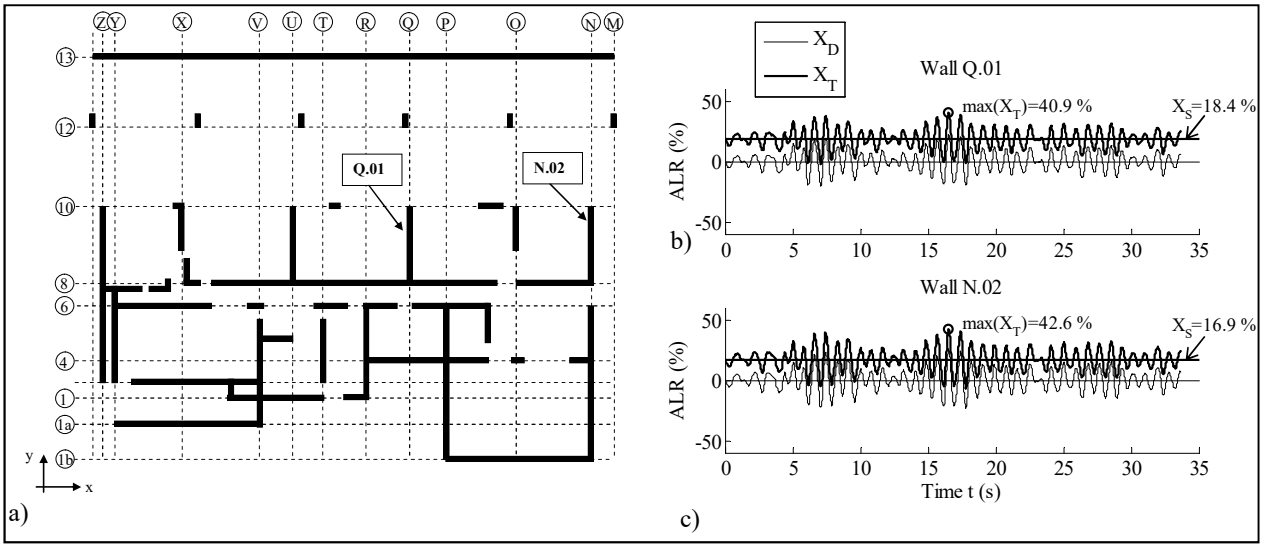

Figure 2-17. First basement of building 7b: a) schematic floor plan of RC walls in the first basement and selected walls; b) time-history results for wall Q.01; and c) time-history results for wall N.02, D1-Y case

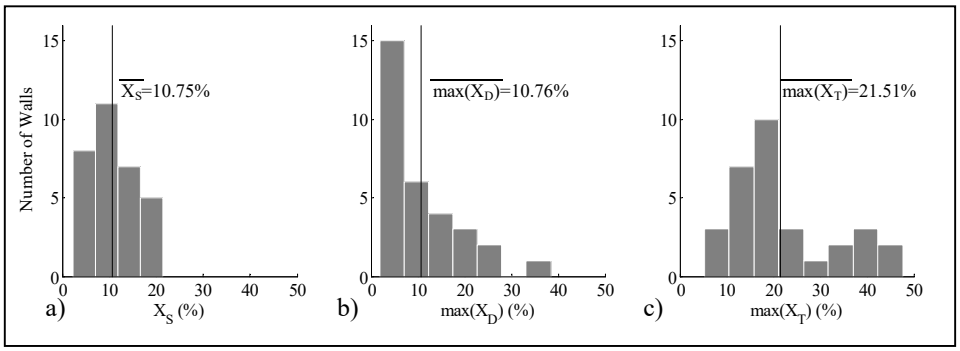

Figure 2-18. Results for the first basement of building 7b, D1-Y case: a) distribution of static axial load ratio; b) distribution of maximum dynamic axial load ratio; and c) distribution of maximum total axial load ratio.

The same procedure was followed for the first five stories of building 7b. Shown in Figure 2-19 a), b) and c) is the distribution of X_S, $max(X_D)$ and $max(X_T)$, respectively, in the form of a standard box plot, where the mean values for each story are marked as **x** and the corresponding values are indicated above the box. The results show that for each story, as it was for the first basement, maximum axial load ratios including dynamic

effects, $max(X_T)$, are about twice the corresponding values for the static component alone.

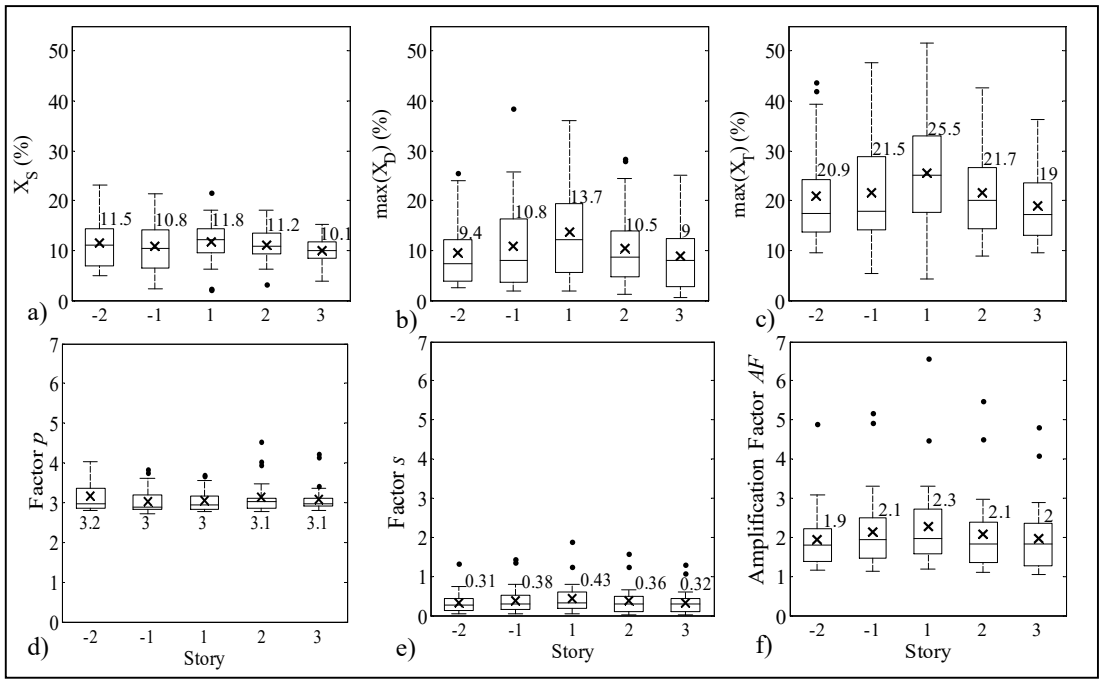

Figure 2-19. Results for first five stories of building 7b D1-Y case: a) distribution of static *ALR*; b) distribution of maximum dynamic *ALR*; c) distribution of maximum total *ALR*; d) distribution of *p*-factor; e) distribution of *s*-factor; and f) distribution of amplification factor *AF*.

Figures 2-19d), e) and f) show the distribution of the factors *p*, *s* and the amplification factor *AF*, respectively, for the first five stories of building 7b as defined previously in Eq. 2-2. Peak factor *p* is about 3 for each story (Figure 2-19d)), which coincides with the definition and values given by Davenport [36]. On the other hand, factor *s* (Figure 2-19e)) is also rather constant among different stories and varies between 0.31 and 0.43. Finally, the amplification factor *AF* (Figure 2-19f)) has mean values of about 2.0 for the five stories considered.

The results for the four dynamic cases defined in Table 2-6 are shown in Figure 2-20, presented for each direction of analysis and for each story of building 7b. Figures 2-20a), c) and e) show average *p*-, *s*-factors and *AF* for the X-Direction of analysis, respectively. It is apparent that the three factors present similar results between the five stories

considered and between the different inputs. The same trend is shown in Figures 2-20b), d) and f), for the Y-Direction of analysis. On the one hand, the *p*-factor is similar in both directions of analysis (Figures 2-20a) and b)), with a value of about 3.6 for the X-Direction and 3.1 for the Y-Direction. However, factors *s* and *AF* differ among directions of analysis. Factor *s* (Figures 2-20c) and d)) is about 0.2 for the X-Direction and 0.4 for the Y-Direction. The amplification factor *AF* (Figures 2-20e) and f)) is about 1.4 for the X-Direction, and 2.1 for the Y-Direction. These results show a clear dependence on the direction of analysis because of the fundamental period of the building.

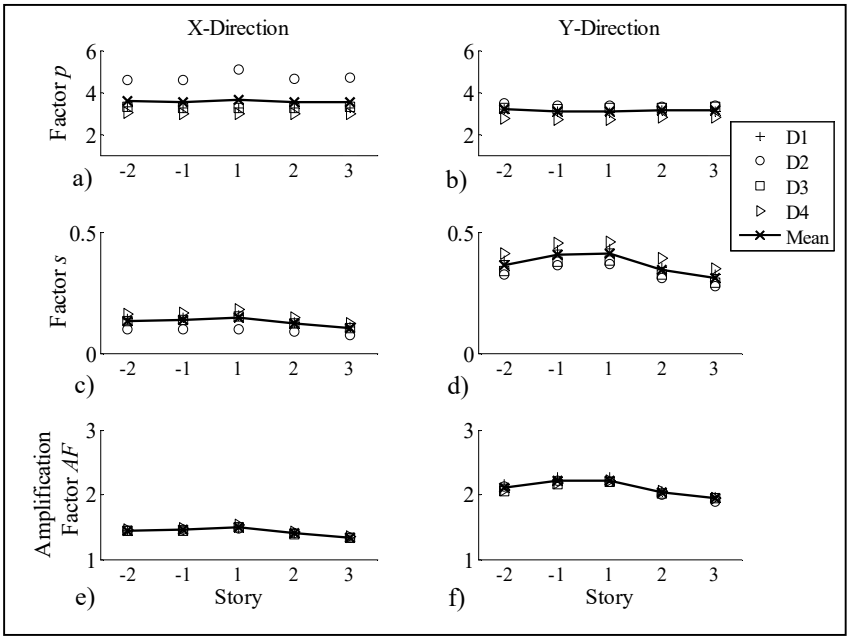

Figure 2-20. Results for Building 7b: a) peak factor *p* in the X-Direction; b) peak factor *p* in the Y-Direction; c) factor *s* in the X-Direction; d) factor *s* in the Y-Direction ; e) amplification factor *AF* in the X-Direction; and f) amplification factor *AF* in the Y-Direction.

2.4.2 Dynamic amplification factor AF

Based on the available data for the inventory of damaged buildings, the objective of this section is to propose a simplified procedure to estimate the *ALR* in walls including both, static and dynamic effects. This estimation aims to assess the seismic vulnerability of existing or new buildings, and to complement other indices that have been used in the past such as *h/T* or DNP [7][8][31].

The same procedure followed in section 4.1 was repeated for a total of four damaged buildings and is summarized in Table 2-7. Again, the first pair of ground motions (D1 and D2) corresponds to the two closest seismic records registered during the 2010 earthquake [40] (Table 2-7); and the second pair of ground motions (D3 and D4) corresponds to two artificial records compatible with the elastic design spectrum defined by the NCh433 Chilean Seismic Code [10][15] for the specific soil type and seismic zone of each building (Table 2-7). Each seismic record was normalized as indicated previously (correcting factor *f* and significant duration). Finally, an additional building (building 28) is selected to blindly test the proposed estimation (Table 2-7).

Table 2-7. Buildings considered in time-history analysis

Building ID	Region	Number of stories (Above g.l. + below g.l.)	Closest Seismic Records (D1-D2)	Soil Type, Seismic Zone (D3-D4)	Critical Levels	Tx (s)	Ty(s)
2	RM	21+1	Santiago Centro/Santiago Peñalolen	II, 2	-1,1,2,3	0.68	1.05
4	RM	20+4	Santiago Centro/Santiago Peñalolen	II, 2	-2,-1,1,2,3	0.71	1.37
7b	RM	18+2	Santiago Centro/Santiago Peñalolen	II, 2	-2,-1,1,2,3	0.52	0.86
27	VIII	18+1	Concepción/ San Pedro	III, 3	-1,1,2,3	0.56	0.81
28	VIII	20+1	Concepción/ San Pedro	III, 3	-1,1,2,3	0.62	0.71

To present global results for each building only critical levels are considered. These levels include the first two basements (if applicable), and the first, second, and third stories (Table 2-7). Such is the selection because most of the damage in RC walls was observed in the lower levels of these buildings [18]. A summary of the results of the four buildings selected is shown in Figure 2-21. First, peak factor *p* apparently does not vary significantly with the period of the building and a constant value around 3.5 can be considered for estimation purposes. Second, factor *s* clearly increases with building period, which leads to an amplification factor *AF* that also increases with building period. Indeed, a linear estimation for the factor *s* in terms of the period *T* is presented in (Eq. 2-3).

$$s(T) = 0.3829T - 0.0638 \qquad \text{Eq. 2-3}$$

Thus, the amplification factor AF for a building with fundamental period T (s) can be estimated as

$$AF(T) = 1 + 3.5 \cdot s(T) \cdot 1/f_a(T) \qquad \text{Eq. 2-4}$$

where $s(T)$ is given by Eq. 2-3, and $f_a(T) = A_b/S_A(T)$ is the scaling factor for the seismic records with $S_A(T) \neq A_b$. With this consideration, amplification factors *AF* range between 1.3 and 2.9 for periods varying from 0.4s to 1.6s, respectively, and considering $f_a(T) = 1$. For example a building with period 0.77 s (the average of damaged buildings), has an estimated amplification factor of *AF*=1.8.

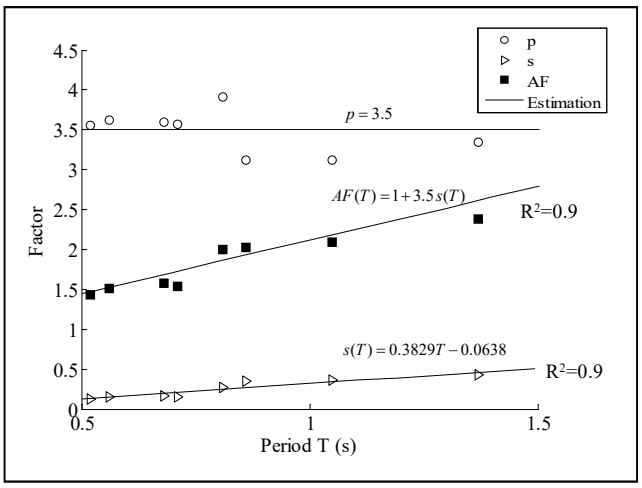

Figure 2-21. Average results for selected damaged buildings.

Consequently, the proposed estimator for the average total *ALR* of a building with period *T*, considering both static and dynamic effects, is $X_T = X_S \cdot AF(T)$. Additionally, for a particular story "*j*" with an average *ALR* due to static loads X_S^j , the total *ALR* can be estimated as $X_T^j = X_S^j \cdot AF(T)$, where the average due to static loads X_S^j can be estimated using, for instance, the recommendations discussed earlier in section 3.4. Please note that the estimated amplification factor *AF(T)* given in Eq. 2-4 is for the average *ALR* and considers all critical levels of the buildings, which actually show a similar behavior.

Finally, analysis for building 28 is presented as a blind example in order to verify the accuracy of the proposed estimation. As for the previous cases, results presented herein correspond to time-history analyses of a finite element linear model, and considering the four different ground motions summarized in Table 2-7. Four critical stories are considered, and results for both directions of analysis are presented independently in

Table 2-8, where it is shown that the average static ALR is $X_S = 9.2\%$. For the X-direction, results from time history analysis show that average ALR due to dynamic effects are as high as $max(X_D) = 34.9\%$ (case D3), which implies a total ALR $max(X_T) = 44.1\%$ and an amplification factor of AF=4.79. Using Eq. 2-4, the estimated amplification factor AF* for this case (D3) is 4.69, with an error of -2%. Analogously, for the Y-direction average ALR due to dynamic effects are as high as $max(X_D) = 32.5\%$ (case D4), which implies a total ALR $max(X_T) = 41.7\%$, and an amplification factor of AF=4.54. Using Eq. 2-4, the estimated amplification factor AF* for this case (D4) is 5.06, with an error of 11%. In any case, amplification factor estimations using Eq. 2-4 are a good predictor of the amplification factor obtained from time-history analysis with a maximum observed error in this case of 12%.

Table 2-8. Time history analysis and ALR estimation for building 28

			X DIRECTION					Y DIRECTION				
			Time History Analysis		Proposed Estimation			Time History Analysis		Proposed Estimation		
Dynamic Case	**Seismic Record**	**X_s**	**max(X_d)**	***AF***	**f_a**	***AF****	**Error**	**max(X_d)**	***AF***	**f_a**	***AF****	**Error**
D1	Concepcion	9.2%	12.6%	2.37	0.45	2.36	0%	28.2%	4.07	0.21	4.47	10%
D2	San Pedro	9.2%	30.9%	4.36	0.18	4.46	2%	20.5%	3.23	0.29	3.50	8%
D3	Compatible 1 Soil III, Zone 3	9.2%	34.9%	4.79	0.16	4.69	-2%	33.1%	4.60	0.16	5.15	12%
D4	Compatible 2 Soil III, Zone 3	9.2%	34.4%	4.74	0.16	4.72	0%	32.5%	4.54	0.18	5.06	11%

2.5. Conclusions

This article summarizes structural characteristics of a group of 36 buildings damaged during the 2010 Chile earthquake. Most of the damaged buildings were rather new structures built after the year 2000. Damaged buildings had high average wall densities, similar to that of typical Chilean buildings in the 1985 earthquake, i.e., 2.8% approximately in each principal direction. However, the set of damaged buildings presents three critical aspects that were not common in buildings affected by the earlier 1985 Chile earthquake: (i) smaller wall thickness, (ii) larger axial loads, and (iii) significantly larger vertical irregularities, especially in the lower levels. The combination of these characteristics induced average axial load ratios ($\overline{ALR}$) in RC walls of the first story due only to gravity effects of about 10%. As a result of this work, it is highly recommended to limit vertical irregularities in resisting planes designed according to the

Chilean code. To generalize the procedure, this could be done by limiting stress concentrations thus avoiding the onset of brittle damage.

The characteristics obtained from a benchmark group of 7 undamaged buildings were similar than those of damaged buildings, thus it is concluded that damage may not be explained by a specific value of a global building parameter, and is the result of several factors such as seismic intensity, foundation soil type, plan and height asymmetries of the structure, structural detailing, difference between design and as-built conditions, and construction details among others. Statistical analysis in terms of an univariate ordinal logistic regression model shows that the most significant variables to explain the observed damage level are the *Region* were the building was located, and the *Soil type*. Additionally, positive correlation is observed between damage level and the floor plan aspect ratio $\overline{b_l/b_t}$, and slenderness ratio $H/\overline{b_t}$ if the undamaged buildings are excluded. Finally, the stiffness parameter *h/T* is the most significant variable when multivariate statistical models are considered.

Although statistical analysis is unable to capture more specific effects, field observations and experimental results have shown that high *ALR* reduce ductility capacity of RC walls and make them more prone to brittle failures. For this reason, time history analyses of damaged buildings are presented to estimate the axial load ratios in RC walls due to seismic effects. For a case-study building, and considering the closest 2010 seismic record, the average *ALR* due to dynamic effects is about 14.5% for the first basement, and reaches a peak of 51.2% for a specific wall.

This article also proposes a simple procedure to estimate the axial load ratios in RC walls including both static and dynamic effects. An amplification factor *AF* is defined as the ratio between the total maximum axial load ratio including dynamic effects relative to the static axial load ratio. It is found that *AF* depends primarily on the period of the building in each direction and on the seismic intensity. Results show that *AF* varies between 1.4 and 2.8 for building periods *T* ranging from 0.5s to 1.5s, and ground motions normalized to 0.2g at the fundamental period of the building. The analysis of an additional shear wall building shows that applying this procedure to obtain blind

estimates of the *AF*, errors are smaller than 12%.The total *ALR*, including the static and dynamic contribution may be used to foresee the vulnerability of existing shear wall buildings subjected to future events that may trigger the observed brittle behavior. Other parameters used in the past, like the shear wall density ρ and *h/T* have proven to be no longer sufficient to predict seismic performance of these structures with brittle behavior, which is highly controlled by large values of axial loads.

AKCNOWLEDGEMENT

The authors are grateful to the many people and institutions which made this work possible. This research was funded by the Chilean Fondo Nacional de Ciencia y Tecnología, Fondecyt through Grant #1110377 and Fondap through Grant # 15110017, and MIT International Science and Technology Initiatives MISTI 2011 “Damage to Chilean High-rise Buildings During Large Thrust Earthquakes”. The authors are grateful for this support and would like to thank also the following professors: Rafael Riddell, Rodrigo Jordán, and Raúl Alvarez, engineers: Rocío Rivera, Benjamín Westenenk, Juan José Besa, and companies: SIRVE S.A., DICTUC S.A., and Spoerer Ingenieros Asociados SpA.

REFERENCES

[1] EERI. The Mw 8.8 Chile Earthquake of February 27, 2010. EERI Earthquake Special Report 2010.

[2] Fritz H, Petroff CM, Catalan PA, Cienfuegos R,Winckler P, Kalligeris N, Weiss R, Barrientos S, Meneses G, Valderas-Bermejo C, Ebeling C, Papadopoulos A, Contreras M, Almar R, Dominguez JC, Synolakis CE. Field Survey of the 27 February 2010 Chile Tsunami. Pure and Applied Geophysics 2011; 168: 1989–2010

[3] Ministerio de Vivienda y Urbanismo (MINVU). National Housing Reconstruction Program 2010. (in Spanish).

[4] Wallace JW, Massone LM, Bonelli P, Dragovich J, Lagos R, Lüders C, Mohele J. Damage and Implications for Seismic Design of RC Structural Wall Buildings. Earthquake Spectra 2012; 28(S1); S281-S299.

[5] Wood SL. Performance of reinforced concrete buildings during the 1985 Chile earthquake: implications for the design of structural walls. Earthquake Spectra 1991; 7(4): 607-638.

[6] Hidalgo P, Ledezma C, Jordán R. Seismic Behavior of Squat Reinforced Concrete Shear Walls. Earthquake Spectra 2002; 18(2): 187-208.

[7] Guendelman T, Lindenberg J, Guendelman M. Bioseismic Buildings Profile. Proceedings of the VII Chilean Conference on Seismology and Earthquake Engineering 1997, Chile. (in Spanish).

[8] Moroni O. Concrete shear wall construction. World Housing Encyclopedia 2011, 6 pp.

[9] Instituto Nacional de Normalización (INN). Reinforced Concrete – Design and Calculation Requirements, NCh430.Of2008. Santiago, Chile, 2008. (in Spanish).

[10] Instituto Nacional de Normalización (INN). Earthquake resistant design of buildings, NCh433 Of.1996 Mod 2009. Santiago, Chile, 2009. (in Spanish).

[11] American Concrete Institute (ACI). Building Code Requirements for Structural Concrete and Commentary (ACI 318-95). Farmington Hills 1995, MI, 391 pp.

[12] Arteta C.A., To D.V., Moehle J.P. Experimental response of boundary elements of code-compliant reinforced concrete shear walls. 2014. Proceedings of the 10th US National Conference on Earthquake Engineering, Paper N°864, July 21-25, Anchorage, Alaska, USA.

[13] Massone LM, Bonelli P, Lagos R, Lüders C, Mohele J, Wallace JW. Seismic Design and Construction Practices for RC Structural Wall Buildings. Earthquake Spectra 2012; 28(S1): S245-S256.

[14] D.S. N 60 MINVU. Reinforced concrete design code, replacing D.S N 118. Chilean Ministry of Housing and Urbanism 2010, Diario Oficial; 13 December 2011 (in Spanish).

[15] D.S. N 61 MINVU. Building seismic design code, replacing D.S N 117, 2010. Chilean Ministry of Housing and Urbanism, Diario Official; 13 December 2011 (in Spanish).

[16] Rojas F, Naeim F, Lew M, Carpenter LD, Youssef NF, Saragoni GR, Schachter M. Performance of tall buildings in Concepcion during the 27 February 2010 moment magnitude 8.8 offshore Maule, Chile earthquake. The Structural Design of Tall and Special Buildings 2011; 20:37-64.

[17] Carpenter LD, Naeim F, Lew M, Youssef NF, Rojas F, Saragoni GR, Schachter M. Performance of tall buildings in Viña del Mar during the 27 February 2010 offshore Maule, Chile earthquake. The Structural Design of Tall and Special Buildings 2011; 20:17-36.

[18] Westenenk B. de la Llera JC, Besa JJ, Jünemann R, Moehle J, Lüders C, Inaudi JA, Elwood KJ, and Hwang S-J. Response of Reinforced Concrete Buildings in Concepción during the Maule Earthquake. Earthquake Spectra 2012; 28(S1): S257-S280.

[19] Westenenk B, de la Llera JC, Jünemann R, Hube MA, Besa JJ, Lüders C, Inaudi JA, Riddell R, Jordán R. Analysis and Interpretation of the Seismic Response of RC Buildings in Concepción during the February 27, 2010 Chile Earthquake. Bulletin of Earthquake Engineering 2013; 11(1): 69-91.

[20] Moehle J, Kelson K, Bray J, Yashinsky M, Holmes W. Chile EERI/PEER Reconnaissance Briefing at UC Berkeley 2010. http://peer.berkeley.edu/events/2010/chile_eq_briefing.html (last accessed 2014/02/21)

[21] Instituto Nacional de Estadística Chile (INE). Building Construction Yearbook 2001-2009, Chile (in Spanish).

[22] Instituto Nacional de Estadística Chile (INE). 2002 Census Results, Chile (in Spanish)

[23] Gómez CE. Structural System Characteristics used in RC and Reinforced Masonry Building Construction in Chile, Civil Engineering Thesis 2001. University of Chile, 215 pp. (in Spanish).

[24] Calderón JA. Update on Structural System Characteristics Used in RC Building Construction in Chile. Civil Engineering Thesis 2007. University of Chile, 76 pp. (in Spanish).

[25] Guzmán MA. Structural Characteristics used in Design of High Buildings in Chile. Civil Engineering Thesis 1998. University of Chile. (in Spanish).

[26] Estay CG. Characteristics of Reinforced Concrete Walls designed in Chile. Civil Engineering Thesis 2008. University of Chile. (in Spanish).

[27] Wood SL, Wight JK, and Moehle JP. The 1985 Chile Earthquake, Observations on Earthquake Resistant Construction in Viña del Mar, Civil Engineering Studies 1987, Structural Research Series No. 532, University of Illinois, Urbana, 176 pp.

[28] Goel RK, and Chopra AK. Period Formulas for Concrete Shear Wall Buildings. Journal of Structural Engineering 1998; 124.4: 426-433.

[29] Moroni O, Astroza M. Characteristic housing types in Chile, 7th U.S. National Conference on Earthquake Engineering 2002 (7NCEE).

[30] Riddell R, Wood SL, de la Llera JC. The 1985 Chile Earthquake: Structural Characteristics and Damage Statistics for Building Inventory in Viña del Mar. Civil Engineering Studies 1987, Structural Research Series No. 534, University of Illinois, Urbana, 265 pp.

[31] Lagos R, Kupfer M. Performance of High Rise Buildings Under the February 27th 2010 Chilean Earthquake. Proceedings of the International Symposium on Engineering Lessons Learned from the 2011 Great East Japan Earthquake 2012. Paper 15, Tokyo, Japan, 1754–1765.

[32] Alarcon C, Hube MA, de la Llera JC. Effect of axial loads in the seismic behavior of reinforced concrete walls with unconfined wall boundaries. Engineering Structures 2014; 73:13-23.

[33] Hube MA, Marihuen AN, de la Llera JC, Stojadinovic S. Seismic behavior of slender reinforced concrete walls. Engineering Structures 2014; (80):377-388.

[34] Agresti A. Categorical Data Analysis. John Wiley & Sons, Inc. 2002. Second edition

[35] R Core Team (2014). R: A language and environment for statistical computing. R Foundation for Statistical Computing, Vienna, Austria. URL http://www.R-project.org/

[36] Davenport AG. Note on the distribution of the largest value of a random function with application to gust loading. Proc, Institution of Civil Engineers 1964; 28:187-196.

[37] Quitral F., Non-linear brittle behavior of shear wall buildings during 2010 Chile earthquake, Master of Science Thesis 2013. Pontificia Universidad Catolica de Chile. (in Spanish).

[38] Computers & Structures, Inc. ETABS v.9.7.1 2011. Berkeley, California, USA.

[39] Arias A. A Measure of Earthquake Intensity, R.J. Hansen, ed. Seismic Design for Nuclear Power Plants, MIT Press 1970, Cambridge, Massachusetts, pp. 438-483.

[40] Universidad de Chile, Departamento de Ingeniería Civil and Oficina Nacional de Emergencia Chile (ONEMI). Earthquakes of Chile 2010. http://terremotos.ing.uchile.cl/2010 (in Spanish) (last accessed 2014/02/21).

[41] Eurocode 8. Design of structures for earthquake resistance, Part I: General rules, seismic actions and rules for buildings, EN 1998-1, CEN – European Committee for Standardization 2004, Brussels.

3. STUDY OF THE DAMAGE OF REINFORCED CONCRETE SHEAR WALLS DURING 2010 CHILE EARTHQUAKE

R. Jünemann[a], J.C. de la Llera[a], M.A. Hube[a], J. Vásquez[a], M. F. Chacón[a]

[a] *National Research Center for Integrated Natural Disaster Management CONICYT/FONDAP/15110017 and Department of Structural and Geotechnical Engineering, Pontificia Universidad Católica de Chile, Vicuña Mackenna 4860, Santiago, Chile*

ABSTRACT

Reinforced concrete shear wall buildings have shown, in statistical terms, an adequate performance in past seismic events. However, a specific damage pattern was observed in 2010, Chile earthquake in some shear walls located in the lower stories of the building, usually associated with high axial stresses, lack of transverse reinforcement, and vertical irregularity. Results show that the nature of this failure led to a sudden degradation in strength and stiffness of walls and resulted in very limited ductility. This research aims to study analytically this damage pattern of shear wall buildings during the 2010 earthquake. By starting with two-dimensional inelastic pushover finite element models using DIANA, two walls that were severely damaged during the earthquake were studied in detail using different load patterns and stress-strain constitutive relationships for concrete in compression. These models were validated with experimental data of four reinforced concrete walls available in the literature. It can be shown that the geometry of the damage in the building walls cannot be correctly represented by conventional pushover load patterns that ignore the lateral and axial interaction. Indeed, the failure mechanism of walls shows strong coupling between lateral and vertical deformations within the plane of the wall. Results shown for a 3D inelastic analysis of the building are consistent with these 2D results, and predict a brittle failure of the structure. However, these models predict a large increase in axial load in the walls, which needs to be validated further with more experimental and analytical studies.

Keywords: shear wall damage, pushover analysis, inelastic finite element models, dynamic inelastic analysis, reinforced concrete buildings, thin shear walls.

3.1. Introduction

Reinforced concrete (RC) shear walls are used in seismic environments as a typical lateral force resisting system to provide an effective seismic load path for lateral motions in buildings, and simultaneously carry vertical loads to the ground. Countries such as Canada, Colombia, New Zealand, and Chile among others, have adopted this structural configuration in practice for an important percentage of their medium to high-rise buildings (e.g., [1],[2],[3],[4]). In Chile, approximately 78% of the RC building stock are shear wall buildings ([5],[6]), typically intended for residential use. These buildings have a plan configuration that resembles that of a "fish-bone" structure [7]. Although these buildings showed in statistical terms an adequate seismic performance in previous 1985 Chile earthquake [8], during recent large magnitude earthquakes in Maule (Chile, 2010), and in Christchurch (New Zealand, 2011), a limited ductility failure has been observed (Figure 3-1), which is characterized by spalling of the concrete cover and buckling of the vertical reinforcement in a zone that extends from the wall boundary well into the web of the wall. This rupture mechanism was observed typically in the lower stories of the building.

This damage pattern was observed repetitively in buildings located in different cities after the 2010 Chile earthquake, and was characterized by concrete crushing and reinforcement buckling throughout the boundaries and web of the wall in the lower stories and/or first basements, usually in the neighborhood of vertical irregularities. A lot of research was conducted after the earthquake in order to describe the observed damage pattern and identify the possible causes of it repetitiveness (e.g., [7],[9],[10],[11]). The principal causes of the observed damage have been attributed to the small wall thickness and high axial stresses (stresses due to gravity loads reach about 10% $A_g f_c'$), stress concentrations due to vertical irregularities, and lack of transverse reinforcement and ties at the wall boundaries and web, which implies limited ductility in the wall due to low concrete confinement and inadequate buckling restraint to its vertical reinforcement. Additionally, different experimental campaigns on RC walls have been developed to reproduce this failure. For instance, Alarcon *et al.* [12] and Hube *et al.* [13] tested ½-scale slender RC walls using a quasi-static cyclic

incremental lateral displacement test protocol with a constant axial load. The main variables analyzed were the axial load ratio, wall thickness, wall aspect ratio, distribution of vertical reinforcement, and the effect of the addition of stirrups and crossties at wall boundaries. Furthermore, Massone *et al.* [14], and Arteta *et al.* [15], have tested RC boundary elements with different levels of confinement under pure compression. Arteta *et al.* [15] proved experimentally that more confinement could not prevent a limited ductile behavior of boundary elements when subjected to pure compression.

Figure 3-1. Typical failure in RC walls in the first basement of building SO during the 2010, Maule earthquake: (a) axis Q; (b) axis U; and (c) axis F. [Photo (b) thanks to Professor Jack Moehle]

The objective of this research is to study the damage patterns observed in several wall resisting planes during the 2010, Chile earthquake, using state-of-the-art analytical models, and link these analytical results with information of the observed behavior. This is done by essentially casting the problem as an inverse one, i.e., by defining the loading conditions in these resisting planes that could have led to the geometry of the observed damage pattern. Several alternative models have been developed and used in the past to reproduce RC shear-wall behavior, ranging from simple macro-models that represent the overall behavior of the wall as a single element, to more sophisticated micro-models that generally discretize the real specimen into small elements where concrete and steel are considered separately. Finite element models and fiber (layer) models belong to this micro-model family, and are typically complex and time consuming computationally [16]. Simpler models that have been used in the past with good results for RC elements are the beam-column element introduced first by Takayanagi *et al.*[17], which is an elastic element in bending with nonlinear springs at both ends; the multiple spring models such as the Multiple Vertical Line Element (MVLEM) introduced first by Vulcano *et al.* [18], which represents the axial-bending behavior of the

wall by a number of uniaxial elements connected in parallel under the assumption of plane sections at the top and bottom ends of the wall; and the panel model developed by Massone *et al.* [19], which couples the flexural and shear response of the wall, retaining most of the features of the MVLEM.

Motivated by the damage observed in shear-wall buildings during the large seismic events occurred recently, different researchers have developed analytical models to better understand the observed behavior. One such example is Magna *et al.* [20], who used a multi-spring macro-model to study Chilean RC walls. Besides bending, the model includes a horizontal shear spring, with properties calibrated using experimental data. Similarly, Vasquez *et al.* [21] proposed a new Force-based Fiber Element (FFE) to perform cyclic analysis including shear effects, bar buckling, and fracture of steel bars, extending the work of previous researchers [22][23]. Furthermore, the collapse of the Alto Rio building was studied using a 3D finite element model [24] aimed to reproduce the inelastic seismic response in the software LS-DYNA [25]. Inelastic response history analyses have also been conducted for a T wall in the damaged Alto Huerto building [24] using Perform 3D [26].

This article aims to identify the most critical modeling assumptions that enable 2D and 3D structural models reproduce the observed damage pattern in these wall buildings. For this purpose, different alternative uniaxial stress-strain constitutive behaviors of concrete were evaluated and validated with experimental data. Regularization of the stress-strain constitutive relationship of concrete in compression, using the preservation principle of fracture energy, was used in all models. Once the constitutive models were validated, two RC resisting planes of a test-bed building damaged during the 2010, Chile earthquake, were studied in detail using pushover analysis and the software DIANA [28]. In the pushover analysis, concrete was modeled by the *smeared cracking* approach, while reinforcement was modeled using an embedded formulation, but neglecting bar fracture in tension and buckling in compression, and assuming perfect bonding. Despite these model limitations, it will be shown that the 2D pushover models provide useful information that helps understand the rupture mechanism that occurred in these walls. The only variables used in replicating the observed damage were the constitutive model of concrete, and the critically important

displacement load pattern imposed to the pushover analysis. Finally, an inelastic 3D analytical model was developed for the complete building to confirm and overcome the eventual limitations of the pushover model and results. The inelastic wall elements used in this building model were the wall fiber elements developed recently by Vasquez *et al.* [21]. The dynamic non-linear analysis of the building was performed for the simultaneous action of the three components of a nearby ground-motion record obtained in a similar soil, and assumed that the inelastic behavior was localized in a few walls of the first building story and basement.

3.2. Model Description

Different alternatives to consider concrete fracture are available in finite element modeling. One alternative is the *smeared cracking* approach, which represents the fracture within a continuum using a stress-strain constitutive model typically with an elastic-softening behavior for both compressive and tensile behavior. Concrete strain in this model may be treated in two ways. First, by decomposing the strain into elastic, ε_e, and cracking, ε_{cr}, components; and second, by using a *total strain* concept that considers stress as a function of the total strain [27], [28]. Additionally, both concepts may consider different alternatives to model the shear stress-strain relationship, which lead to the *fixed crack* and *rotating crack* models. In the *fixed crack* model the principal axes are fixed during the post-cracking phase, while in the *rotating crack* model the principal axes co-rotate with the principal strains during crack propagation [27]. Herein, the *total strain rotating crack* model is used since it has proven to match reasonably well experimental results [27], [29] and has an adequate numerical stability [30].

Inelastic finite element models are developed in DIANA [28] using the *total strain* model just described. Concrete is modeled using the Q8MEM element, which is a four-node quadrilateral iso-parametric plane stress element, based on a linear interpolation for the displacement field, and uses Gauss-point quadrature. Reinforcement is modeled using the BAR element, which is an embedded element and follows the assumption of perfect bonding [28]. Reinforcing steel is modeled using exponential hardening (Voce, [28]), and a typical

example of this law is shown in Figure 3-2(a). It is important to notice that this stress-strain constitutive model is equal in tension and compression, and the model does not include the effect of bar buckling or fracture. This is a limitation of the 2D model, as bar buckling was observed in damaged walls after the 2010 earthquake. However, as discussed later, results of the 3D nonlinear model that include bar buckling show that for the particular building studied in this article, the buckling effect of bars is less important since the structure remains essentially elastic until the failure cycle.

In modeling plain concrete, DIANA presents different alternatives to simulate the inelastic behavior in tension and compression based on predefined constitutive models. Herein, four alternatives are evaluated to model concrete compressive behavior, which are shown in Figure 3-2(b). The constitutive models considered are: (i) the constant model (CONS), because it is very stable and provides reasonable estimates for the capacity of RC members; (ii) the Thorenfeldt (THOR) model, which depends on the unit-dependent parameters n and k that can be assumed by the software [28] or provided by the user; (iii) the Parabolic (PARA) model [28], which is based on the compressive fracture energy G_c assumed to be a material property, and the crack bandwidth h, which it is assumed equal to the square root of the area of the element –i.e., for a square element, the crack bandwidth equals the element size; and (iv) the Multilinear (MULT) model, which is based on a user defined set of stress-strain pairs. The backbone constitutive relationships for concrete in compression is characterized by the peak stress σ_p and the corresponding peak strain α_p. These values consider the increase of strength due to lateral confinement according to the Selby and Vecchio relationship [28], and the compression softening effect according to Vecchio and Collins [28]. These effects are not included in the MULT case; however, the decrease in Poisson's ratio with increased cracking is included in all models [28].

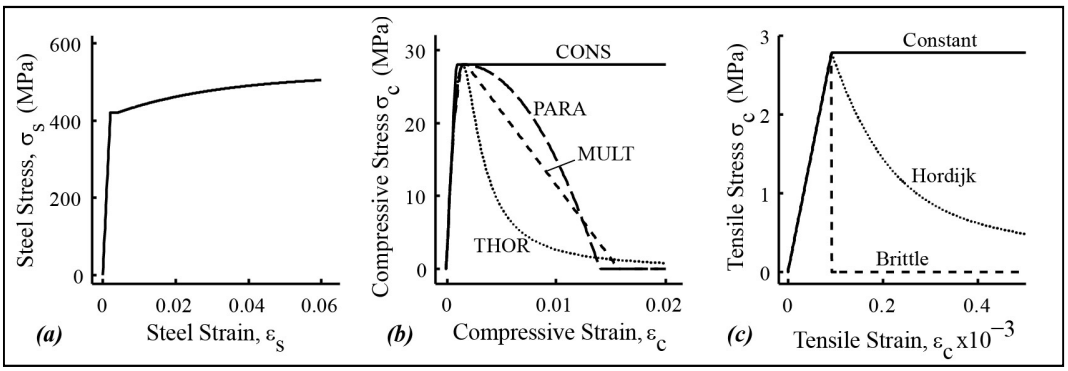

Figure 3-2. Stress-strain constitutive models: (a) reinforcing steel; (b) concrete in compression; and (c) concrete in tension.

For concrete tensile behavior, three stress-strain constitutive models are used. They are the constant, Hordijk, and brittle models as shown in Figure 3-2(c). The Hordijk model is based on the tensile fracture energy G_f, which is related to a crack bandwidth h. For the tensile properties, the CEB-FIP (1990) [31] code recommendations are followed. Thus, the tensile strength f_t is estimated as $f_t = 1.4(f_c'/f_{c0}')^{2/3}$, where f_c' is the concrete compressive strength, $f_{c0}' = 10$ MPa, and the tensile fracture energy G_f is estimated by $G_f = G_{f0}(f_c'/f_{c0}')^{0.7}$, where G_{f0} is the base value of fracture energy depending on the maximum aggregate size $d_{\max}$. In this case, a maximum aggregate size of 32 mm is assumed, which corresponds to $G_{f0} = 0.058$ MPa-mm [31].

In finite element models, results are usually affected by the mesh-size effects, especially when a strain-softening rule is adopted. A customary assumption is that the concrete fracture energy is an inherent material property, and hence, the parameters of the stress-strain relationship need to be adjusted to keep the compressive fracture energy G_c constant [32], [31]. For the PARA model, in which the stress-strain relationship depends on the crack bandwidth h, the software automatically modifies the stress-strain relationship based on the element size of the model. For other constitutive models with strain-softening such as THOR and MULT, the energy regularization consists in adjusting the respective parameters of the stress-strain constitutive relationship in order to keep the fracture energy G_c independent of the element size h. This is done by imposing:

$$G_c = h \int_{\varepsilon_o}^{\varepsilon_u} \sigma(\varepsilon) d\varepsilon \qquad \text{Eq. 3-1}$$

where G_c is the compressive fracture energy per unit area of plane, h is the element size, $\sigma(\varepsilon)$ is the unixial stress-strain relation in compression, $\varepsilon_o = \varepsilon_p/2$, and $\varepsilon_u = \frac{2G_c}{f_c' h} + \varepsilon_o$. Figure 3-3(a) shows the stress-strain relation and parameters proposed by Nakamura and Higai [32].

Unlike for the tensile fracture energy G_f, there is no substantial information on the concrete compressive fracture energy G_c. Nakamura and Higai [32] investigated experimentally the compressive fracture zone and found that the compressive fracture energy, defined by the energy per cross section area absorbed in the fracture zone is constant regardless of the element size and shape, while it is influenced by the maximum size of the aggregate. Therefore, in finite element analyses, the compressive fracture energy can be considered as a material property given by $G_c = 8.8\sqrt{f_c'}$ in MPa-mm.

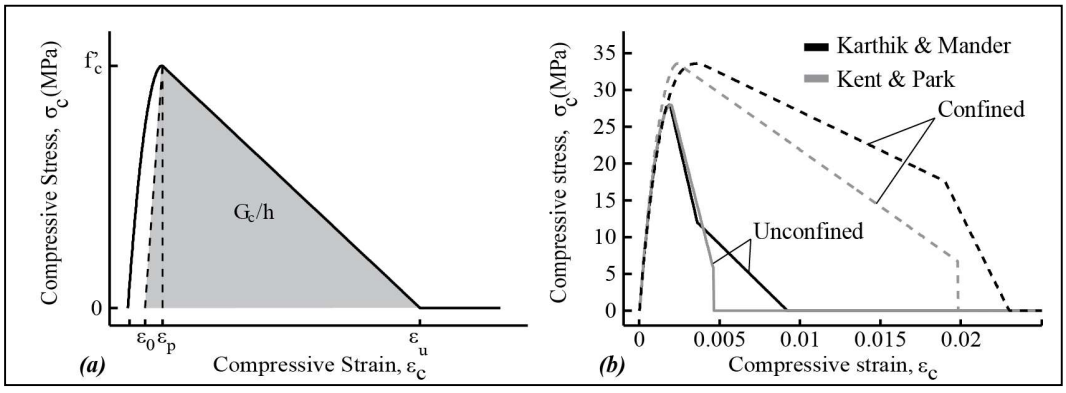

Figure 3-3. a) Energy regularization; and b) unconfined and confined concrete constitutive models.

The compressive fracture energy proposed by Nakamura *et al.* [32] corresponds to unconfined concrete, and recommendations for the compressive fracture energy of confined concrete G_{cc} do not exist. The effect of confinement is shown in Figure 3-3(b), where the stress-strain constitutive models proposed by Karthik and Mander [33], and by Kent and Park [34], are shown for unconfined and confined concrete, with cylindrical strength $f_c' = 28$ MPa, and confinement ratio $K = 1.2$. The area under the stress-strain relationship of

unconfined concrete is obviously lower than confined concrete. Thus, considering an element of the same size h_{eq}, it is possible to estimate the compressive fracture energy for confined concrete G_{cc}. First, for the two constitutive models for unconfined concrete shown in Figure 3-3(b), the equivalent element size h_{eq} is estimated as $h_{eq} = \frac{G_{uc}}{\int_{\varepsilon_0}^{\varepsilon_u} \sigma_{uc}(\varepsilon) d\varepsilon}$, where $\sigma_{uc}(\varepsilon)$ is the stress-strain constitutive relationship, and G_{uc} is the compressive fracture energy for unconfined concrete. Then, the compressive fracture energy for confined concrete G_{cc} is estimated as $G_{cc} = h_{eq} \int_{\varepsilon_0}^{\varepsilon_u} \sigma_{cc}(\varepsilon) d\varepsilon$, where $\sigma_{cc}(\varepsilon)$ is the stress-strain constitutive relationship for confined concrete. Finally, the average fracture energy obtained by considering the two constitutive models is considered. For the example in Figure 3-3(b), the unconfined compressive fracture energy given by $G_{uc} = 8.8\sqrt{f_c'} = 46.6$ MPa-mm, and the confined compressive fracture energy estimated by this proposed methodology is $G_{cc} = 289.2$ MPa-mm, i.e., $G_{cc}/G_{uc} \approx 6$. Once unconfined and confined compressive fracture energy are estimated for a given RC specimen, the stress-strain relationship for finite element analysis must be adjusted for the selected element size according to Eq. 3-1. The proposed regularization technique will be validated in the next section.

3.3. Validation between inelastic FEM and experimental results of single walls

A series of RC specimens tested earlier were modeled using the material definitions described in the previous section aimed to validate the proposed finite element models and regularization technique. The three rectangular and single T-shaped RC wall specimens selected are summarized in Table 3-1, where the axial load ratio (ALR) is calculated as the total axial load relative to $A_g f_c'$ and expressed in percentage. The first specimen (ID1, Figure 3-4(a)) corresponds to a rectangular-shaped unconfined wall tested by Dazio *et al.* [35] on an experimental campaign of quasi-static cyclic tests on six RC slender walls [36]. Specimen ID2 (Figure 3-4(b)) corresponds to the specimen boundary element tested by Arteta *et al.* [15], who performed an experimental campaign of seven thin boundary elements tested under pure compression. Specimen ID3 (Figure 3-4(c)) corresponds to another rectangular wall tested by Dazio *et al.* [35] but with confining reinforcement at both ends. Finally, shear

wall ID4 (Figure 3-4(d)) corresponds to a T-shaped wall tested by Thomsen and Wallace [37]. The general information of the selected specimens is summarized in Table 3-1, and the material properties are summarized in Table 3-2. If material properties exist from tests results, these values are used in the models; otherwise, recommendations discussed in section 2 are used.

Table 3-1. General characteristics of selected RC wall specimens.

ID	Wall	Type	Wall thickness, t_w (cm)	Wall length, l_w (cm)	Shear span, h_w (cm)	ALR (%)
1	WSH4	Rect-Unconfined	15	200	456	5.7%
2	W3	Rect-Confined	31	91.5	183	-
3	WSH3	Rect-Confined	15	200	456	5.8%
4	NTW1	T-Confined	10	122	366	9%

Table 3-2. Material properties of selected RC wall specimens.

	Concrete						**Steel**	
ID	f_c' (MPa)	E (MPa)	G_{uc} (MPa-mm)	G_{cc} (MPa-mm)	f_t (MPa)	G_f (MPa-mm)	f_y (MPa)	C (MPa)
1	41	38,500	56.3	-	3.58	0.155	576	98.9
2	26	18,670	44.9	389.8*	2.65	0.113	420	0
3	39	35,200	55.1	308.9*	3.48	0.151	601	124.5
4	33	24,115	50.5	519.0*	3.10	0.133	434	207

* Estimated in this investigation.

3.3.1. Unconfined rectangular specimens

Specimen ID1 was modeled first since it represents an unconfined slender shear wall similar to those damaged during the 2010, Chile earthquake. In this case, concrete strength f_c' and Young´s modulus E were obtained from cylinder concrete specimens [35]. The confinement ratio calculated for this specimen according to Kent and Park [34] is K=1.01, which is very low, and hence, only unconfined concrete is considered in the finite element analysis. Finally, tensile strength and tensile fracture energy are estimated according to CEB-FIP

recommendations [31] previously presented in section 2. The mean yield and maximum stress values of a 12 mm reinforcing steel bar, obtained from uniaxial tension tests, are 576 MPa and 675 MPa, respectively. The hardening constant is *C*=99 MPa, and the properties for other diameter bars are detailed elsewhere [35]. For Voce´s hardening rule, the hardening exponent assumed is $\varepsilon_0 = 0.03$ and the yield plateau is $\varepsilon_{p1} = 0.002$. These values are kept the same for the other three walls analyzed in this section.

Finite element models were developed in DIANA following the description presented in Section 2. Four different mesh sizes were used to validate the proposed regularization methodology, *h*=20, 10, 5 and 2.5 cm. Figure 3-5(a) shows schematically the finite element model for mesh size *h*=20 cm, where the displacements in the base nodes are constrained. Vertical load is applied as a first load case, and lateral displacement is applied gradually in the nodes located at the horizontal actuator height as a second load case. As stated earlier, four different concrete stress-strain constitutive models in compression were considered: (i) CONS, (ii) THOR, (iii) PARA, and (iv) MULT. Shown in Figure 3-5(b) are the final compressive stress-stress relationships after energy regularization using the unconfined compressive fracture energy, G_{uc}. The CONS model does not depend on the mesh size, whereas the other three models depend on it. For THOR model, the parameters *n* and *k* are scaled simultaneously in order to ensure fracture energy conservation. For the THOR model, Figure 3-5(b) includes in gray the stress-strain constitutive relationship with default values for *n* and *k* given by the software (T_0) [28]. Finally, the MULT model is based on Nakamura *et al.* [32] and is defined with a linear ascending branch up to the concrete strength associated with the deformation ε_p, taken as 0.0021 in this case, and a descending branch up to ε_u defined by Nakamura [32], which varies with the mesh size. The tensile behavior in all cases is modeled using Hordijk´s stress-strain constitutive model, since no significant differences were found when considering different tensile models regularized with tensile fracture energy.

Force-displacement results obtained using CONS, PARA, THOREN and MULT models are shown in Figures 3-6(a) through (d), respectively, and considering the four mesh sizes. CONS model (Figure 3-6(a)) accurately predicts the specimen strength for all mesh sizes,

but misses completely the ultimate behavior of the specimen. It is also apparent from this figure that a thinner mesh increases the stiffness of the system. Further, all other models provide a good estimate of the strength of the specimen, and also good results for the strength degradation and ultimate behavior of the specimen. Figure 3-6(c) shows in lighter gray lines the results obtained for T_0, i.e., considering the default values of n and k in the THOR model without energy regularization. It is clear that for any mesh size, this case results in a poor prediction of the specimen behavior, showing the relevance of the proposed regularization.

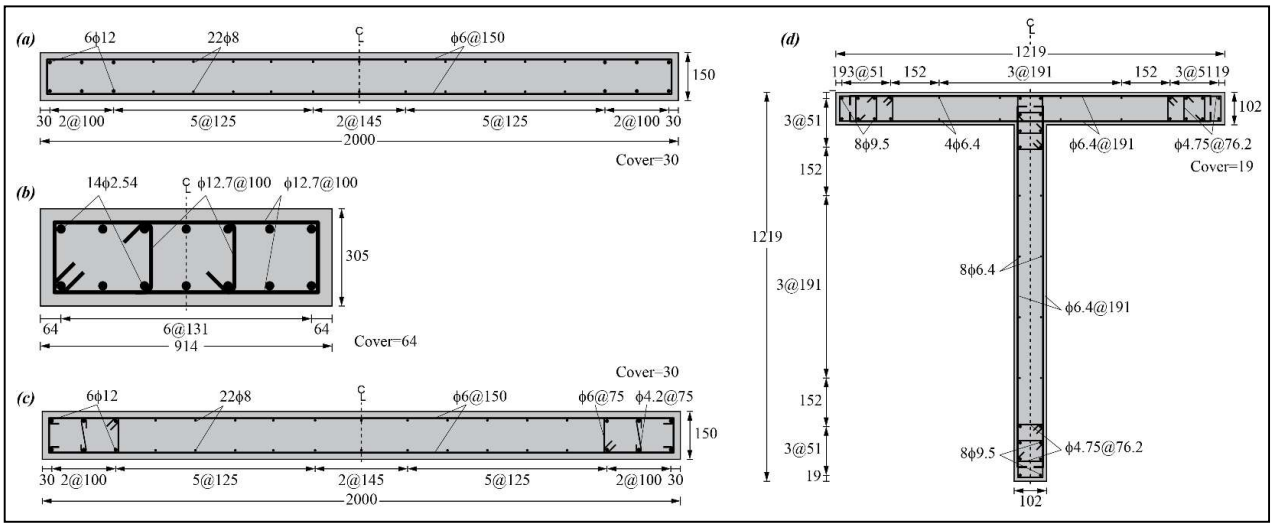

Figure 3-4. Cross-sections of the selected specimens: (a) ID1, WSH4 Dazio *et al.*; (b) ID2, W3 Arteta *et al.*; (c) ID3, WSH2 Dazio *et al.*; and (d) ID4, TW1 Thomsen *et al.* All units in cm.

Table in Figure 3-6 summarizes the strength obtained for each stress-strain constitutive model and mesh size, and strength measured in the experiment was 443 kN. The range of strength estimation for a given stress-strain constitutive model between different mesh sizes with respect to the experimental result, ΔF_{mesh}, varies between 3% and 11%, showing that the effect of the mesh-size for any stress-strain constitutive model is small due to the proposed energy regularization method. Moreover, the range of strength estimations for a given mesh-size between different stress-strain constitutive models and experimental results, $\Delta F_{\mathrm{Model}}$, varies between 6% and 11%; therefore, all models provide in this case a good estimation of the experimental lateral strength of the specimen. CONS model leads to the best results in terms of strength relative to the experiment, followed by PARA and MULT

models, while THOR model presents the largest difference with the experimental measurement.

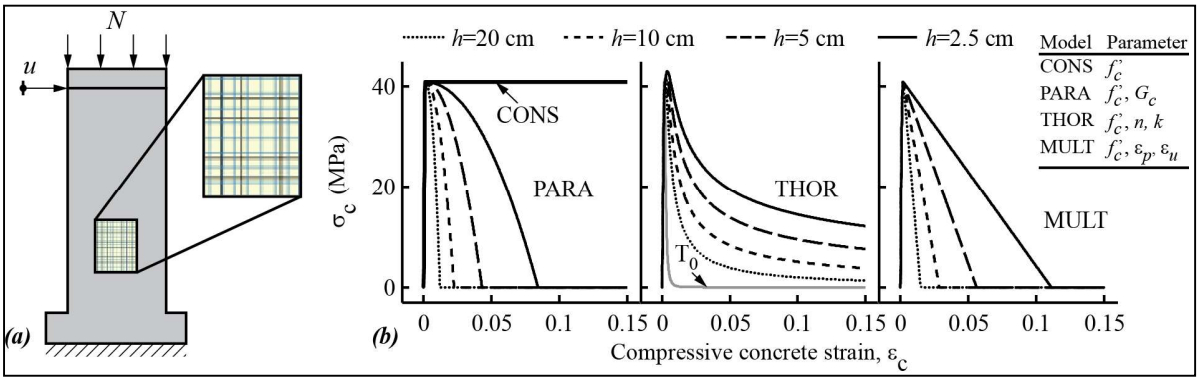

Figure 3-5. Schematic view of the wall and stress-strain constitutive models: (a) Finite element models for mesh size *h*=20 cm; and (b) compression stress-strain for PARA, THOR and MULT models, respectively and for different mesh sizes.

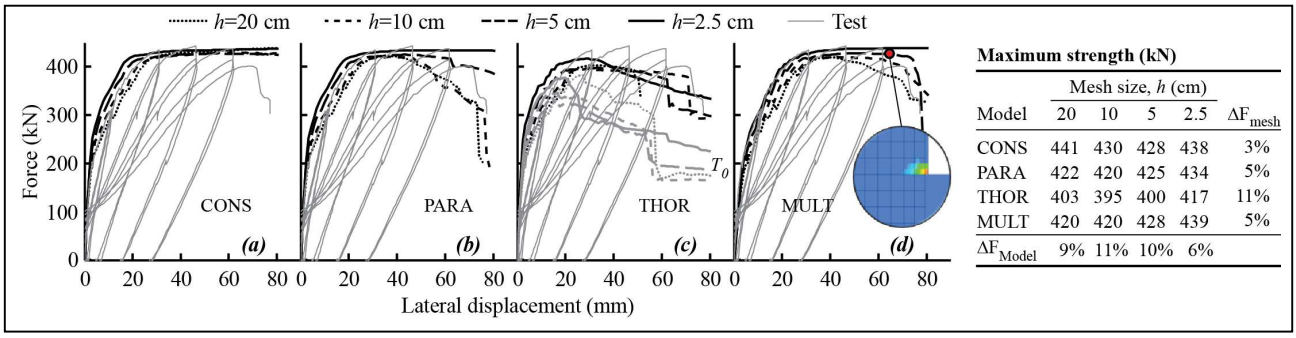

Maximum strength (kN)

Model	Mesh size, *h* (cm) 20	10	5	2.5	ΔF_{mesh}
CONS	441	430	428	438	3%
PARA	422	420	425	434	5%
THOR	403	395	400	417	11%
MULT	420	420	428	439	5%
ΔF_{Model}	9%	11%	10%	6%	

Figure 3-6. Estimation of the relationship between force and top displacements using different finite element meshes and stress-strain constitutive relationships, Specimen ID1: (a) CONS; (b) PARA; (c) THOR; and (d) MULT.

With respect to the ultimate behavior, Figure 3-6(a) shows that CONS model completely misses the ultimate behavior of the specimen. It also appears that PARA model (Figure 3-6(b)) is more sensitive to the mesh size than THOR and MULT models, and apparently MULT model is the best model in predicting the ultimate behavior of the specimen for all mesh sizes. Figure 3-6(d) includes a close-up of the calculated damage pattern at the base of the specimen with mesh size *h*=5 cm and constitutive MULT model. The figure shows the plastic concrete compressive deformations in the step marked with a red dot in the force-

displacement relationship, which represents the concrete crushing at the bottom right corner of the specimen. The model predicts that the plastic deformations concentrate in the corner of the test unit, which coincides well with the damage pattern obtained in the test [35]. The presented results show that a good selection to represent the wall behavior would be MULT model with a mesh size h=5 cm, which corresponds to 40 finite elements along the wall length in the critical section. Moreover, PARA model gives very good results, with the advantage that no regularization is needed in this case.

3.3.2. Confined rectangular specimens

Specimen ID2 was selected to validate the proposed methodology for the compressive fracture energy of confined concrete. The specimens were detailed with transverse reinforcement according to current code requirements for special boundary elements. Concrete strength f_c' and Young´s modulus E were obtained from experimental tests of concrete cylinders [15]. Unconfined concrete fracture energy G_{uc} was estimated following the recommendations given earlier [32], while the confined concrete fracture energy G_{cc} is estimated following the procedure described in Section 2. The confinement ratio calculated according to Kent and Park [34] is K=1.275, and the estimated G_{cc} considering either of Karthik-Mander (K&M) and Kent-Park (K&P) constitutive models are 291.6 and 488.1 MPa-mm, respectively. The average value between these models is $G_{cc} = 389.8$ MPa-mm. Figure 3-7(a) shows results obtained for a mesh size with h=5 cm considering the unconfined and confined concrete fracture energy. It is clear that using PARA model with unconfined concrete fracture energy (PARA-G_{uc}) is not adequate in this case. Furthermore, results show that using PARA model with a confined fracture energy G_{cc} in the range between K&M and K&P leads to more reasonable results. Also, results of the MULT regularized to the mesh size are also presented and prove to lead to good accuracy. Therefore, for this case it is recommended to use either a parabolic constitutive model with mean confined compressive fracture energy G_{cc}, or a multilinear constitutive model regularized to mesh size.

Specimen ID3 is a rectangular specimen with the same layout as specimen ID1, but with confined boundary elements as shown in Figure 3-4(c). This specimen was used to validate

the method to estimate the compressive fracture energy for confined concrete. General dimensions and material properties of the specimen are presented in Tables 3-1 and 3-2, respectively, and unconfined and confined concrete fracture energies were estimated as in the previous case. The confinement ratio calculated according to K&P [34] is K=1.11, and the estimated G_{cc} considering K&P and K&M stress-strain constitutive models are 315.3 and 300.8 MPa-mm, respectively. The average between both models is $G_{cc} = 308.1$ MPa-mm will be used for confined concrete in finite element models. Using a mesh-size h=10 cm, the results for PARA model are shown in Figure 3-7(b). It is apparent that using unconfined concrete properties G_{uc} for all concrete elements is not adequate and underestimates the wall capacity (PARA-G_c). However, using mean confined concrete fracture energy G_{cc} at boundary elements (PARA-G_{cc} Mean) gives reasonable results, which validates the proposed model for confined concrete.

3.3.3. T-shaped specimen

The last specimen (ID 4) has a T-shaped cross section (Figure 3-4(d)). This specimen aims to verify the behavior of the analytical model when the cross section of the element is no longer rectangular. Thomsen and Wallace [37] tested four 1/4-scale structural walls under constant axial stress and cyclic lateral load—two with rectangular and two with T-shaped cross sections. The specimen modeled in this study corresponds to TW1 as indicated in Table 3-1. Because the finite element model is planar, the T-wall flange needs to be modeled with 48 in thick elements (Figure 3-8(a)). A fine mesh of 1 in is considered, and the model was loaded with 50% of the total axial load concentrated at the edge elements of the flange of the wall, while the other 50% of the total axial load was uniformly distributed throughout the web. With this assumption, the nodal forces applied to the model are N_o=73,338 N (5 edge nodes) and N_i=7,639 N (44 web nodes) (Figure 3-8(a)). Analytical results are presented in Figure 3-8(b). The proposed analytical model predicts a specimen capacity and stiffness larger than the experimental results. This discrepancy can be attributed to different effects, such as reinforcement slip, pedestal rotation, reinforcement buckling, and the effective width of the flange. The latter, derived from a shear lag effect, is important in this case since the flange size is (1:1) relative to the web size. In the 2D model proposed, all the elements in the

flange are basically subjected to the same deformation (i.e. a “plane section” case), and reinforcement located at the wall flange yields simultaneously (and also hardens simultaneously), which is not necessarily the case in the real wall.

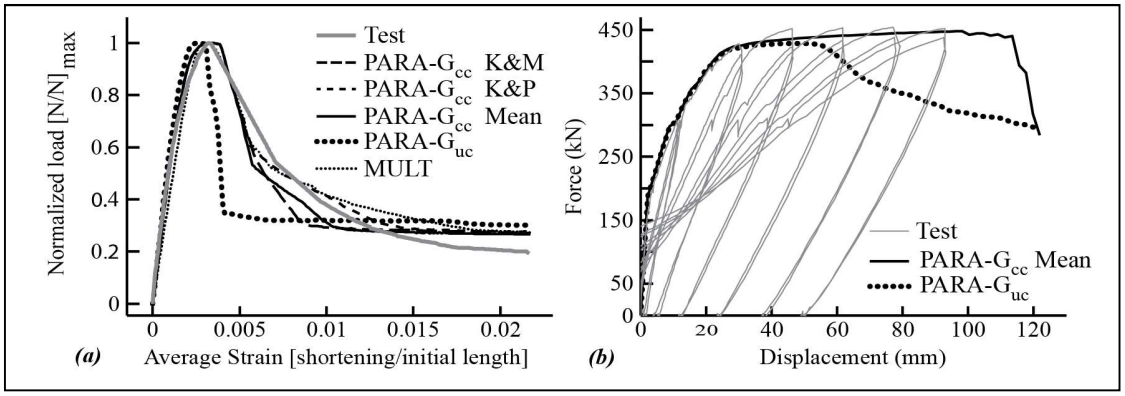

Figure 3-7. Finite element models results for confined concrete: a) specimen ID3; and b) specimen ID4.

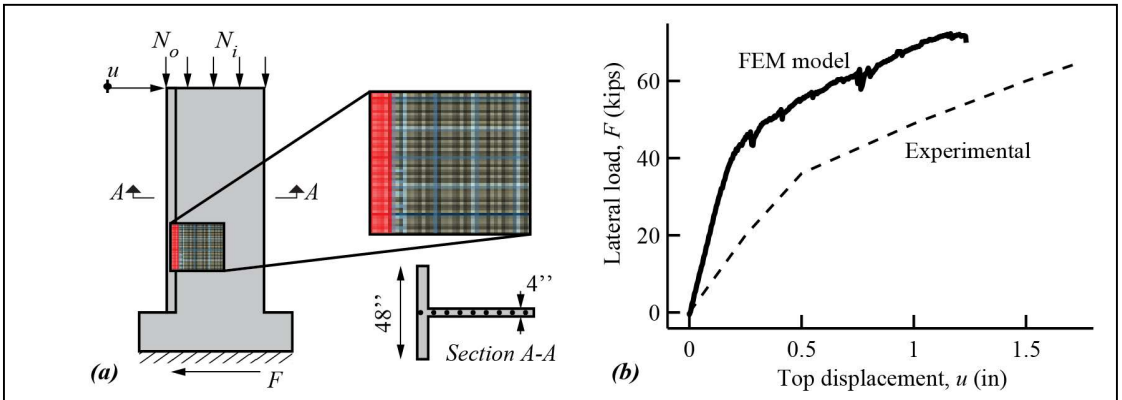

Figure 3-8. Finite element model for specimen ID5: (a) model; and (b) analytical results.

3.4. Model of RC walls damaged during the 2010 earthquake

This section investigates the use of the described analytical model to predict the damage mechanism of actual shear wall resisting planes during the 2010, Chile earthquake. Because the same failure repeated in different buildings, two RC resisting planes of a damaged building located in Santiago (Building SO) are used as a benchmark. The building has 18 stories and 2 basements, and is composed by two symmetrical blocks (called herein blocks

“a” and “b”) separated by a construction joint. Each block is composed of RC shear walls of 20 cm thickness, deep beams of dimension 20 by 75 cm, and 15 cm thick floor slabs. First, a detailed analysis is provided for the damaged resisting plane (shear wall) Q (Figure 3-9), and the second case is the damaged resisting plane U (Figure 3-9), both located in block “b” of the building.

3.4.1. Damage of resisting plane Q

A schematic 3D view of the building obtained from a linear 3D finite-element model developed in ETABS [38] is presented in Figure 3-9(a). The wall layout presents a typical “fish-bone” like configuration with central longitudinal walls in the East-West direction, and orthogonal walls in the North-South direction (Figure 3-9(b)). The upper stories are for residential use, while the basements are intended for parking. The basements have a larger floor plan area with RC columns in the extended underground zone to allow for vehicle circulation. Both blocks have an almost identical plan configuration, and block “b” has an average shear wall density (total area of walls divided by tower area, calculated at the first level above grade) of 6.5%, an average wall thickness of 20 cm, and a fundamental period of 0.86 s in the N-S (Y) direction. Figure 3-9(b) shows a typical floor plan of block “b”, where the selected resisting plane Q is indicated, and the elevation of the wall is depicted in Figure 3-9(c).

Figures 3-9(d) and (e) show the cross section of wall Q at the basements and the first story, respectively. These figures show that the wall is quite slender, has an offset that leads to a flag-shape (walls having a significant reduction of the wall length in one story compared with the story immediately above), presents very low boundary transverse reinforcement, and has a pronounced irregularity at the ground level, where the wall changes in length and cross section. Indeed, the wall shortens from 695 cm in the first story to 575 cm at the basement, and the orthogonal wall flanges of 70 cm in the first story are discontinued also at the basement. The vertical boundary reinforcement increases from 4ϕ22 to 4ϕ25 at the basement; additional ϕ8 stirrups spaced at 17 cm are included in the basement.

The building suffered severe damage during the 2010, Chile earthquake. Damage was localized in the transverse shear walls at the first basement level and north side of the building. Figure 3-1 shows the observed damage in different axes of Building SO. Figure 3-1(a) shows the failure of the shear wall Q, where the damage initiated at the boundary and propagated almost horizontally toward the interior of the building stopping at the longitudinal wall along axis 8, which served as a large flange. The concrete crushed in essentially all the trace of the rupture and longitudinal boundary reinforcement buckled. Similar failure was observed in axis U and F of the same building, as shown by Figures 3-1(b) and (c), respectively. Furthermore, the basement columns located in the enlarged basement area near the failure wall boundaries also presented severe damage with reinforcement buckling, cracking, and spalling of concrete. Additionally, punching shear failure of slabs was also observed at this level. Some other shear walls located in the first story presented damage at the wall boundary, but with less intensity. The resisting elements in upper stories, including walls and slabs did not show significant damage.

The roof displacement demand imposed by the earthquake is estimated using the recommendations of the Chilean supreme decree D.S. N 61 [39], which establishes that $\delta_u = 1.3S_d(T_{cr})$, where $T_{cr} = 1.5T_y$, is the estimated cracked period of the structure in the direction of analysis, and equal in this case to 1.29 s. The response displacement spectra considered in the analysis in the N-S direction are the ones obtained from two recorded ground motion stations closer to the building (Santiago-Peñalolen and Santiago-Centro) [40]. The estimated ultimate roof displacement for these two ground motions ranges between 13 cm and 18 cm.

An inelastic finite element model of resisting plane Q was developed in DIANA [28], aimed to replicate the damage pattern observed in Figure 3-1(a) by means of an inelastic pushover analysis. The data here are represented by the damage pattern of the wall, and the unknown is the kinematic condition that may have caused such failure. The 2D analytical model follows the regularization assumptions discussed in the previous sections. The nominal properties specified in the project ($f_c' = 25$ MPa, $f_y = 420$ MPa) were used, and following the CEB-FIP recommendations [31] the tensile fracture energy used in the model is $G_f =$

0.111 MPa-mm. For the compressive fracture energy, recommendations by Nakamura and Higai [32] were used which results in $G_{uc} = 44$ MPa-mm.

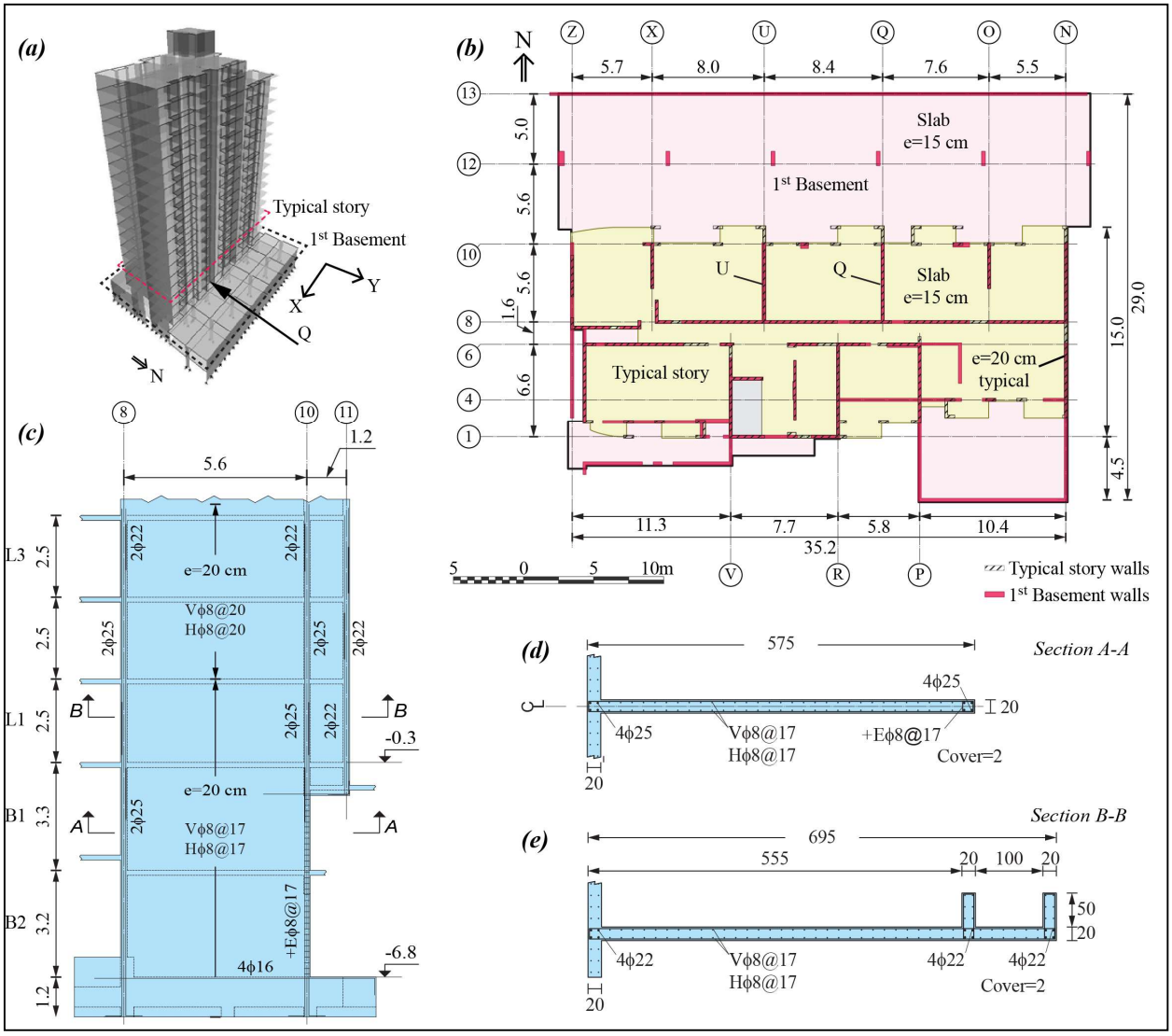

Figure 3-9: (a) schematic 3D view of the structural model (block "b"); (b) first basement and typical story floor plan of block "b" (m); (c) elevation of resisting plane Q (m); (d) section A-A of axis Q at basements (cm); and (e) section B-B of axis Q from first story and above (cm).

Since the boundary confinement of the wall is limited (Figure 3-9(c)), only unconfined concrete is considered in the finite element model. The Hordijk model was considered for concrete tensile behavior, and different stress-strain constitutive models in compression

were evaluated: (i) CONS; (ii) PARA; (iii) THOR; and (iii) MULT. PARA model is automatically regularized internally by the software for the effect of element size; and THOR and MULT models have to be regularized independently to account for the proper element size. In THOR model, the default parameters *n* and *k* are scaled to satisfy Eq. 3-1, resulting in *n*=2.27 and *k*=0.73. Finally, the MULT model is defined as a multi-linear model with a linear ascending branch up to the concrete strength defined by a Young´s modulus E, followed by a horizontal plateau up to the deformation ε_p, taken as 0.0021 in this case, and a descending branch up to ε_u defined by Nakamura [32], taken as 0.034 in this case.

The web of the shear wall is modeled using 0.2 m thick elements, while the wall flange (axis 8) is modeled using 2.9 m thick elements according to the flange dimension from first story and up. The orthogonal wall flanges in the first story (Figure 3-9(e)) are modeled with 70 cm thick elements. Because the model is planar, the implicit assumption is that the behavior of these orthogonal flanges is equivalent to that of elements symmetrically placed relative to the central plane of the wall. Both, horizontal and vertical displacements, are fixed at the base of the wall (second basement), and gravitational loads are applied to the nodes at each floor level. These loads were obtained from a 3D linear finite-element model of the building developed in ETABS [38] using dead load plus 25% of live load (D+0.25L). Figure 3-10(b) shows the gravitational load of wall Q in each story. The large increase in axial load observed for the first basement is attributed to the increased floor plan dimension of the basements, and the use of the space as parking and garden areas (Figure 3-9(b)). This larger vertical load is combined with a decrease in wall length at this level resulting in ALR=15% for the critical section (section A-A in Figure 3-9(c)).

To determine the strength and failure mechanisms of wall Q, a pushover analysis with controlled displacements was performed. Consequently, four different displacement load patterns, or Load Cases (LC), were imposed into the wall. These LCs are schematically shown in Figure 3-10(a) and correspond to: (i) a constant lateral displacement at all roof nodes of wall Q (R); (ii) floor lateral nodal displacements that increase in height according to an inverted triangular pattern (T); (iii) floor lateral nodal displacements that result from the predominant elastic mode shape in the direction of the wall (M1); and (iv) floor lateral

and vertical nodal displacements that result from the predominant elastic mode shape (MV1). As a reference, the deformed shape of wall Q for the predominant elastic building mode in the direction of the wall (first ETABS mode) is shown in Figure 3-10(c). The lateral and vertical displacements at the floor levels are the ones imposed into the floor nodes of the MV1 model. Please note that lateral displacements are equal within a floor level for all models, but vertical displacements in MV1 are not. Before imposing any LC to the wall, the gravitational loads (D+0.25L) shown in Figure 3-10(b) are applied as vertical floor nodal forces for cases R, T and M1, and as equivalent nodal vertical displacements for case MV1. In the pushover analyses, all imposed nodal floor displacements are proportionally increased by a factor until failure.

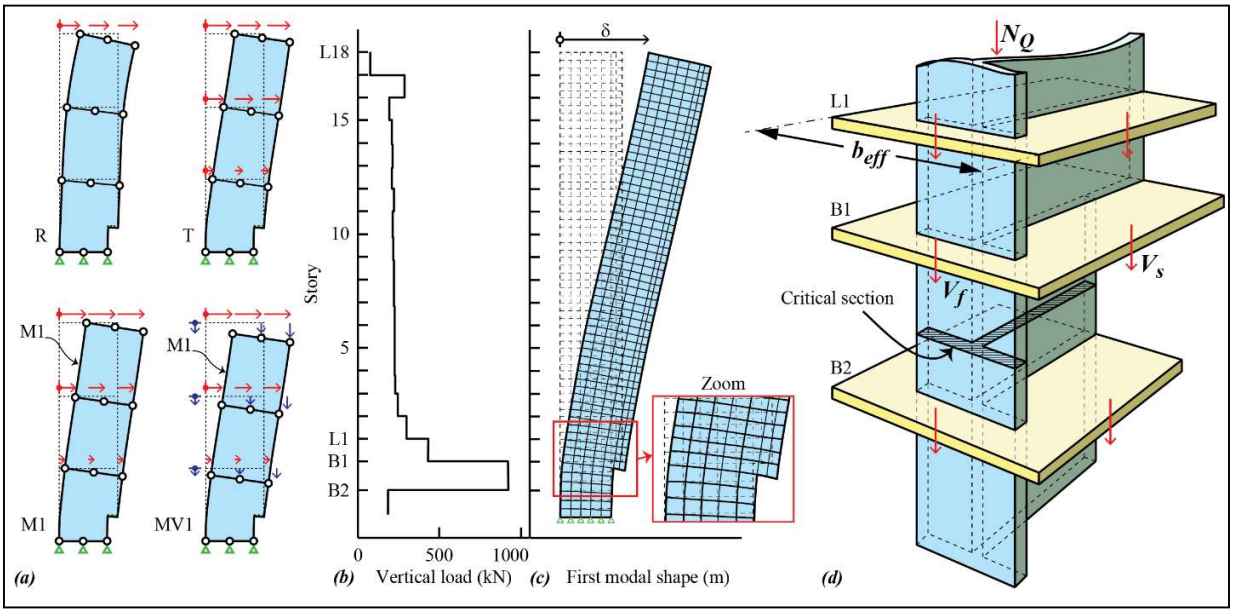

Figure 3-10: Pushover analysis and transfer of axial loads into wall Q: (a) schematic view of imposed displacement patterns for pushover analyses; (b) height-wise distribution of gravitational loads in wall Q (D+0.25L); (c) predominant elastic mode shape (first building mode) in the direction of wall Q; and (d) slab framing action and vertical load transfer mechanism to the wall.

One difficulty in pushover analysis of a planar resisting plane is to correctly represent the 3D interactions between the plane and the rest of the structure. Such kinematic interactions occur in this case through the floor slab, since it is the only element connecting wall Q with the rest of the structural system. As with any substructure, this interaction is captured by the

displacements and rotations at the contact boundary between wall and slab. Therefore, the rationale behind load case MV1 is to include, in addition to the modal floor lateral displacements of M1, the modal vertical displacements at the wall-slab contact interface. These displacements represent the framing action of the slab and enable to capture variations in the axial load of the wall due to lateral motion of the building. Indeed, as confirmed by the linear dynamic ETABS model and the MATLAB inelastic dynamic building model presented later in Section 5, a building displacement in the north direction produces an increase in the axial load of wall Q. Therefore, the imposed vertical displacements are responsible for bringing the additional axial load to the wall that results from the wall interaction with the rest of the structure. As shown schematically in Figure 3-10(d), the variation in axial load of wall Q is produced by variations in the shear forces of the slabs. Further, this increase in axial load of wall Q cannot be accounted for by load patterns that neglect vertical displacements such as R, T, and M1, which lead to constant axial loads. Because the inelastic dynamic results presented later show that the building remained essentially elastic until failure, it seems reasonable to assume as a load pattern, the predominant vibration mode of the building in the direction of the wall.

Figure 3-11 summarizes the results from the inelastic pushover analysis of the four loading cases and stress-strain constitutive models used for concrete in compression. The figure plots the bending moment at the centroid of the critical section versus the lateral roof displacement for each case. The critical section corresponds to the base of the wall for LC T, and to the first basement for the other three load cases (Section A-A Figure 3-9(c)). The concrete plastic deformations of the bottom portion of the wall are also identified in the figure for some critical steps in the pushover analysis. In general, Figure 3-11 shows that the behavior of the shear wall is sensitive to the imposed displacement pattern and to the stress-strain constitutive model of concrete in compression.

Figure 3-11(a), (b) and (c) shows results for load cases R, T and M1, respectively. These cases implicitly assume a constant axial load equal to the gravity loads (ALR=15% due to gravity loads), since the lateral displacement pattern does not impose vertical loads. This effect translates into poor outcomes of the three loading cases when trying to represent the

damage pattern observed in the wall. For instance, case R (Figure 3-11(a)) does not present strength degradation and fails to resemble the horizontal crack observed at the first basement during the earthquake (Figure 3-1(a)); Figure 3-11(b) shows that case T predicts a limited ductility behavior, but damage localizes at the bottom of the wall and none of the damage patterns observed, irrespective of the stress-strain constitutive models used, resemble the observed damage pattern. On the other hand, case M1 (Figure 3-11(c)) concentrates the plastic deformations of the wall at the irregularity between the first basement and first story and is able to predict the initial damage pattern, but cracking does not propagate toward the interior of the wall, as with case R. Finally, Figure 3-11(d) shows the results for case MV1, which presents clear strength degradation for different stress-strain constitutive models after the roof displacement exceeds approximately 9 cm. This displacement value is quite consistent with the estimated roof displacement obtained later for the 3D dynamic analysis. Figure 3-12(a) shows the ALR for the different stress-strain constitutive models considered in case MV1. For the PARA and MULT models, a peak ALR=47% is obtained, which is also consistent with the dynamic results. Additionally, PARA and MULT models show a very stable behavior and characterize well the damage pattern observed after the earthquake (Figure 3-11(d)). The THOR model fails abruptly prior to reach the wall strength and the CONS model clearly overestimates the wall capacity.

Shown in Figure 3-12(b) are the theoretical M-Φ curves for the critical section of the wall (section A, Figure 3-9(d)). The moment strength of the wall for the initial ALR of 15% is $3x10^4$ kN-m, which is consistent with the average strength predicted by pushover analysis for the first three load patterns. Moreover, Figure 3-12(b) shows that for an ALR=45%, the wall strength increases to $3.8x10^4$ kN-m. The strength predicted by the pushover analysis in the case MV1 is lower than this value possibly because the kinematic condition imposed in this load case leads to a higher compression in the wall flange, thus changing the location of the axial resultant. In the case of section analysis (Figure 3-12(b)), the axial load is always applied in the center of gravity of the section.

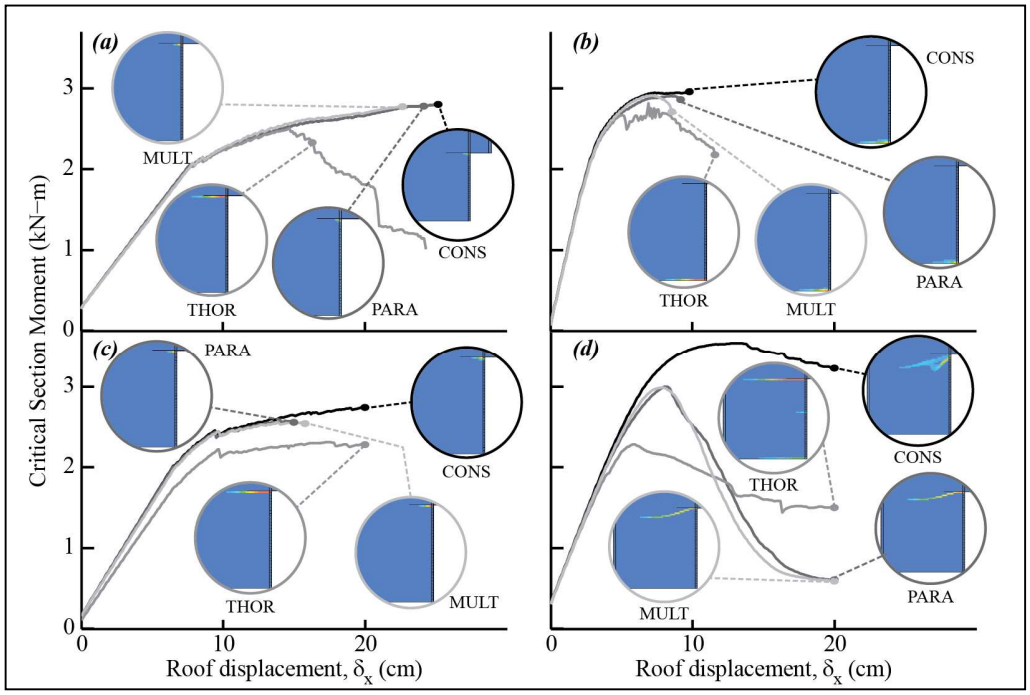

Figure 3-11: Finite element model results: (a), (b), (c) and (d) moment-displacement for load cases R; T; M1 and MV1, respectively.

Because of the large increase in axial load observed in wall Q, it is important to verify if such increase is feasible given the shear capacity of the surrounding slabs. To make comparisons easier, all numbers are expressed in terms of ALR (%) in wall Q. The maximum shear capacity of the slab would be developed for a punching mechanism of the wall into the slab, which could be induced, say, by a large upward acceleration. If a shear failure is assumed at every story above the critical section (19 stories), a maximum ALR=165% could be transferred into wall Q. This punching shear mechanism is unlikely, but only as a reference, it was obtained using a critical section perimeter b_o=17 m and a nominal shear strength of $v_c = 0.33\sqrt{f_c'}$ (MPa) (shears V_f and V_s in Figure 3-10(d)). This number would be reduced to half, i.e. ALR=82.5%, if we consider the one-way shear strength of the slab. Although it was not observed, a lower bound for this value could be found by assuming a flexural double yield line mechanism to occur along the hallway of the slab between axis 6 and 8 (Figure 3-9(b)). Such mechanism could originate from the lateral displacement of the building in the north-south direction, and the maximum shear that results from it implies an ALR=17% (V_f in Figure 3-10(d)). This estimate is based on nominal properties, neglects the

shears transferred by the slab sections parallel to the wall (V_s in Figure 3-10(d)), and assumes an effective slab width of 8 m (b_{eff} in Figure 3-10(d)). Hence, this mechanism would lead to an ALR=15%+17%=32% for wall Q. The shears transferred by the slabs running parallel to the wall V_s are expected to increase the axial load in wall Q due mainly to the vertical component of ground motion, the biaxial motion of the structure, and any load transfer from other failing walls. Indeed, as will be discussed in Section 5, at the time of failure of wall Q, t^*, it can be shown that vertical acceleration would increase the gravitational loads in this wall by approximately 19% more, leading to a final lower bound for ALR of about 35%. For all these reasons, ALR=35% should be considered as a lower bound for ALR. Therefore, though it seems a high value, the ALR=47% estimated by the pushover, which is also consistent with an ALR=45% shown later by three-dimensional inelastic dynamic analysis, lies within a range of possible ALR values.

3.4.2. Damage of resisting plane U

The proposed methodology was also applied to another severely damaged resisting plane of Building SO (plane U). The cross section and elevation of wall U are similar to those of wall Q (Figures 3-10(a)-(c)), except that wall U is 25 cm thick instead of the 20 cm of wall Q. Wall U is reinforced with double layer of horizontal and vertical reinforcement ϕ10@17 cm instead of bars ϕ8 as for wall Q. From the first-story upward, both walls U and Q are identical. The damage of wall U is shown in Figure 3-1(b) and is similar to that of wall Q.

In this case, in order to validate the results presented earlier for wall Q, only case MV1 is presented, i.e., a condition of lateral and vertical nodal displacements according to the first mode of the building in the direction of analysis. Figure 3-12(c) summarizes the results obtained for the bending moment at the critical section versus roof displacement. As for the case of wall Q, it is shown that the imposed load pattern MV1 is able to predict the observed damage pattern for the PARA and MULT models.

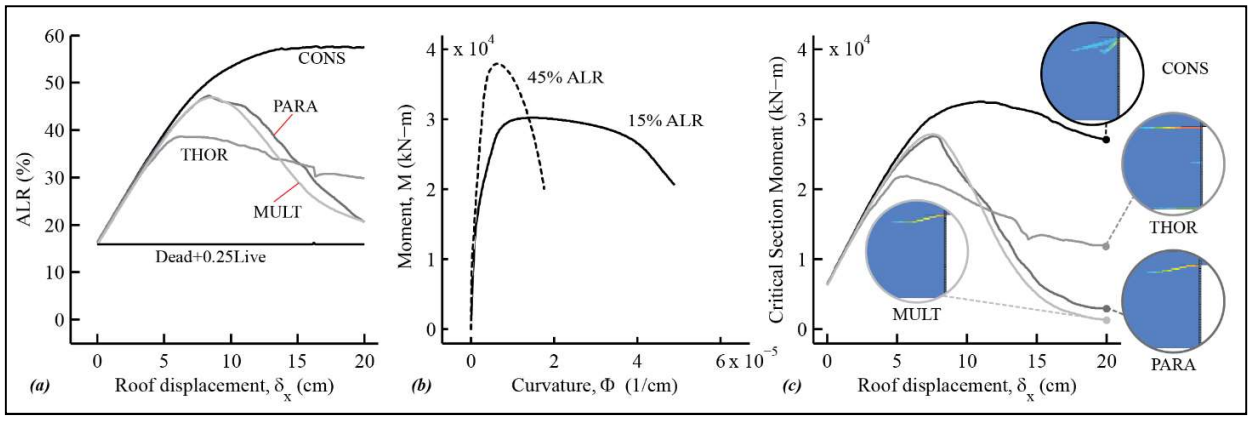

Figure 3-12: Resisting plane parameters: (a) Axial load ratio (ALR) for wall Q and LC MV1; (b) theoretical capacity M-Φ curves for axis Q and U; and (c) moment-displacement results for wall U and MV1.

3.5. Inelastic dynamic analysis of Building SO

The damage of Building SO is analyzed using a 3D model, nominal concrete properties, and a ground motion acceleration record obtained near the building site. A 3D dynamic model was developed by combining a 3D linear elastic finite element model of the building, extracted from ETABS [38], with the inelastic force-based RC walls [21]. The model was subjected to the three components of ground acceleration recorded in the nearby station Peñalolén [40] (Chile, 2010), which was obtained for similar soil characteristics to those in the selected building.

Because structural damage is localized in the first story and basement, the structural model includes only nonlinearity in some walls of the lower levels of the building, while the rest of the structure remains elastic. This is a reasonable assumption based on the observations of the building after the earthquake. The nonlinear elements used to model RC walls were fiber elements that account for bending and compression behavior. Although the element model allows to account for nonlinear shear behavior, such behavior was neglected in this case due to the high slenderness of the building. Indeed, a bending-compression failure was expected, as it was empirically observed after the earthquake in Building SO and several others [9]. None of these buildings showed diagonal cracking, thus proving the greater importance of bending and compression behavior over shear. One limitation of the dynamic model was to

consider an elastic behavior of the floor slabs. Although this is a typical assumption in current Chilean practice, and there was no significant damage reported after the earthquake on these slabs, this effect could have led to an overestimation of the framing action of the slab and hence, an overestimation of axial loads in some walls.

Figure 3-13 shows a wall of shell elements connected to the force-based fiber element used [21]. Both elements have the same section, but the fiber element incorporates several nonlinear behaviors for each type of fiber. The cyclic stress-strain relationship of concrete is based on the Kent and Park model [34], while the relationship for steel includes the monotonic curve as a bound of the cyclic behavior, the Bauschinger effect, and the bar buckling introduced through a softening region with a reduced stiffness when reloading from this zone. The softening slope gets steeper as the spacing of transverse reinforcement increases [21] (Figure 3-13(d)). All the fibers are regularized taking the length associated with each integration point, as explained elsewhere [21], where a detailed description of constitutive models can be found. The effect of tension strain prior to buckling, although experimentally observed and studied elsewhere [41], is not taken into account in the present study, since for this particular building, with walls subjected to high axial loads, the analyses show that maximum tension strains prior to failure are mainly in the elastic region of the steel curve, i.e. $\varepsilon < 0.002$.

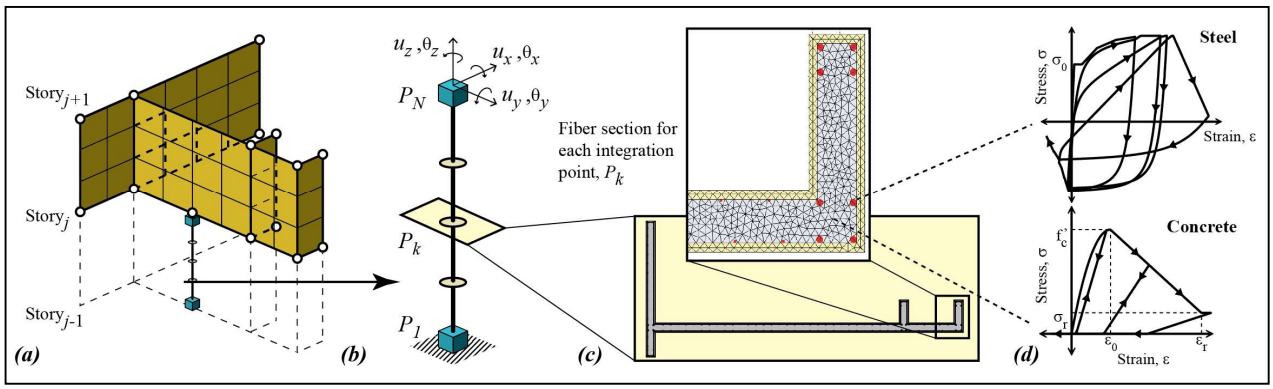

Figure 3-13. Modeling of shear wall with a fiber element, degrees of freedom, and meshing of the sections

The detailed algorithm for taking the original ETABS model to the final nonlinear model includes the following steps: (1) to check the mesh of the ETABS model, and generate manually a compatible mesh in ETABS [38]; (2) to translate the model without kinematic constraints from ETABS to SAP2000 [38], and check that periods and mode shapes are about the same (error less than 5%); (3) to include rigid in-plane diaphragms to the model in SAP2000 in order to reduce the number of degrees of freedom (DOFs); (4) to extract the mass and stiffness matrices from the SAP2000 model; (5) to identify the walls (or portions of them) to be modeled by the inelastic fiber element and create a rigid body constraint at the ends of the element in the SAP2000 model—in the model created, 27 nonlinear elements were used corresponding to 10 different shear walls, namely N,O,Q,R,T, U, X,Y, Z, 1b and 1c (Figure 3-15), where O, Q, U and X were modeled with fibers from the second basement to the second story; (6) to create fiber sections for these elements with nominal properties; (7) using MATLAB [42], recognize the nonlinear elements identified in (5) and introduce the fiber elements with the sections created in (6); and (8) to prepare the system to be integrated with Newmark's method ($\beta = 1/2$ and $\gamma = 1/4$), given its unconditional stability—Newton-Raphson iterations are used for convergence within each iteration, in which the stiffness matrix is evaluated at each sub-iteration. The mass matrix obtained using SAP2000 is singular and has masses only associated with translational DOFs. Although a consistent mass matrix is a good choice, for the sake of simplicity, a small mass value ($1e^{-7}$ tonf-s^2/cm^3) was added to the diagonal terms corresponding to rotational DOFs to make the matrix invertible, following procedure recommended by [43]. This simplification in the mass matrix can be numerically justified since it has a negligible effect in the calculated dynamic response. With the mass matrix and linear stiffness matrix from (4), Rayleigh damping was assumed for the model. The damping matrix used was $C_r = 0.325M + 0.0013K_{elastic}$. These values were calculated after arbitrarily imposing 3% of critical damping at 1.2 times the fundamental period (0.84 s), and for the period for which the mass participation factor was close to 70%. The factor 1.2 is used not to overestimate damping as periods become longer due to the nonlinear response. The typical integration time step used was 0.005s, and it was dynamically reduced to 0.001s in critical cycles.

Figure 3-14 (a) shows the three ground motion components used in the analysis, and Figures 3-14(b) and (c) show the dynamic response of resisting plane Q. Showing the history of ALR at the critical section of wall Q (just below the setback), part (b) presents a sudden failure after reaching a peak ALR=45%. This sudden failure is also reflected in part (c), which shows the hysteretic curve of the bending moment at the critical section versus the roof displacement of the building. Three distinctive zones can be identified in this plot: an essentially elastic zone, which is asymmetrical in both horizontal directions due to the T-shape of the wall; a softening zone, which comes just after the negative peak at 9.19 cm (-3.97x10^4 kN-m) and corresponds to ALR=43%; and a residual zone, which is characterized by low capacity residual moment-deformation cycles, which is indicative of a larger reduction of the moment capacity of the wall. Please notice that the softening zone is consistent with the strength of -3.8x10^4 kN-m estimated by the M-Φ curves in Figure 3-12(b). The softening slope in this zone is abrupt and almost vertical, meaning that the failure presented very limited ductility. Indeed, maximum historic concrete compressive strains of the wall remains lower than the deformation at maximum concrete strength in the cycles before the peak, and increases abruptly up to 0.055 at the peak cycle. After failure, the bending moment of the wall changes from negative to positive value, which is due to the shift in the resultant of axial load. It is the floor diaphragm that holds the damaged section in place and limits its increase in deformation. Additionally, results of the dynamic model show that all walls severely damaged during the analysis O, Q and U failed in the same cycle just after t=79.76 s (Figure 3-14(a)), all with very limited ductility.

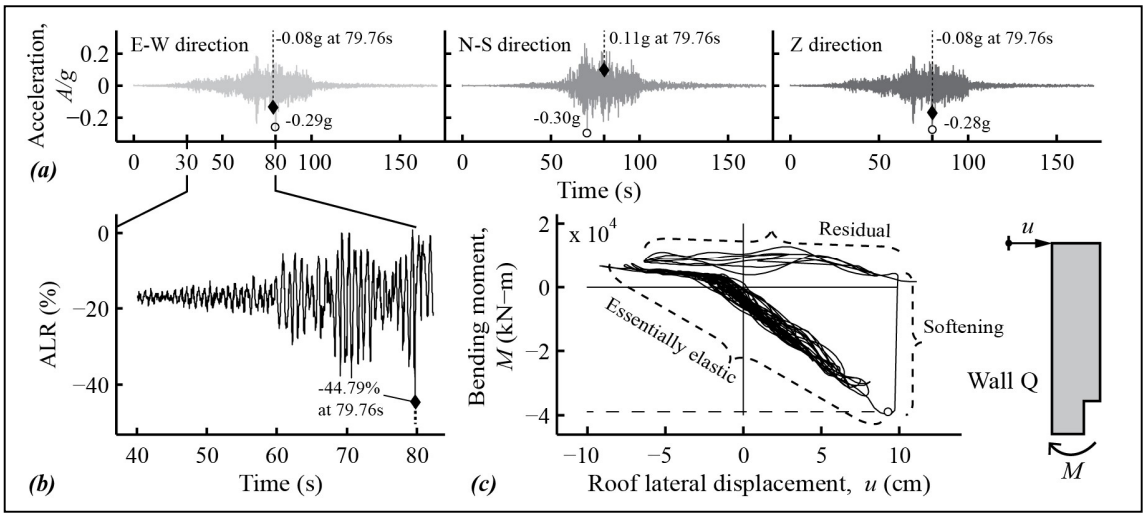

Figure 3-14. Ground motion and results obtained from the inelastic dynamic analysis: (a) acceleration records; (b) axial load ratio (ALR) history at the critical section; and (c) critical-section bending moment-displacement for wall Q.

Results of the dynamic analysis are in good agreement with results from the 2D pushover analysis. For instance, the ALR at the peak response obtained with pushover analysis (47%) is very similar to the one obtained by dynamic analysis (45%); also, the roof displacement at peak strength for the dynamic and pushover analyses is essentially the same (≈10 cm). The results of dynamic analysis also show a large increase in the ALR of walls, effect that is also present in the pushover analysis for the displacement pattern MV1. This observation supports the hypothesis that the wall behavior in this case could be represented by a 2D pushover analysis with an imposed displacement pattern such as MV1, which accounts for the framing action of the slab through coupling between the lateral and vertical nodal displacements.

Shown in Figure 3-15 are the ALR of different walls at the time of failure of wall Q, i.e. t^*=79.76 s. The position of the resultant of all vertical forces acting on the first basement at t^* is plotted in this figure together with the same resultant at time $t=t_0=0$. The latter corresponds to the position of the Center of Gravitational Forces (CG) at that level. At initial time t_0, the total vertical load is $W(t_0)$=-88,977 kN, which is split in -49,423 kN carried by the walls above the CG and -39,554 kN by the walls below the CG. An upward vertical shift in the location of this resultant of vertical forces in the figure at t^* would be indicative of

larger compression loads in the walls above the CG. In fact, at t^* the resultant of vertical forces for all walls above the CG is -95,952 kN, almost twice the value at t_0. Conversely, the resultant of vertical forces for all walls below the CG decreases to -9,643 kN. The increase in compression of the walls above the CG is accompanied by an increase in the tensile forces of some walls below the CG, reaching a peak tensile ALR=24.2% in wall 1c (Figure 3-15). This significant ALR is smaller than the tensile capacity of the wall, ALR=29%, due to the significant contribution of the boundary reinforcement. Furthermore, the reason for wall U (next to the left of Q) to show a smaller ALR is due to failure of this wall one hundredth of a second earlier, leading to an instantaneous transfer of axial load to the neighboring walls.

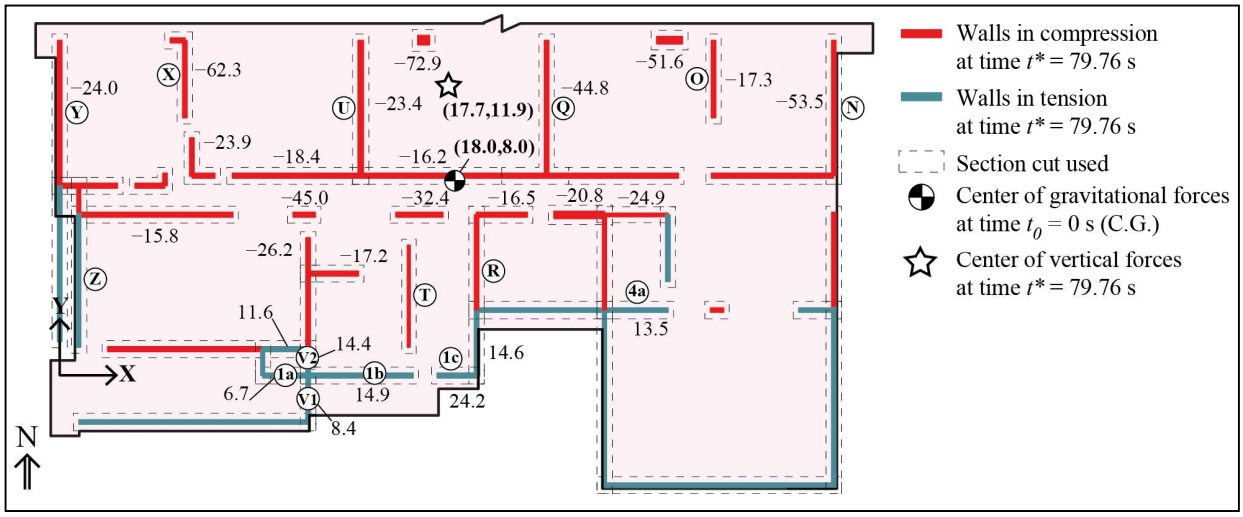

Figure 3-15. Axial load ratio (ALR %) distribution in the first basement at the instant of failure of wall Q, where negative values correspond to compression and smaller values between -15% and +5% have been omitted for clarity.

Although it is plausible that a significant increase in the axial loads occurred in shear walls due to overturning and vertical ground acceleration in the building, thus leading to brittle behavior and the observed damage pattern, it is also fair to say that the actual failure mechanism should probably lie between the two following cases. One as presented characterized by a low number of cycles of the wall exposed to high ALR, brittle behavior ([12],[44]), and lateral displacements consistent with the estimates provided by elastic and inelastic building models; and the other, corresponding to a cyclic degradation of the wall

under axial loads more comparable to the gravity loads [45] and lateral displacements that are likely to be larger than the ones predicted by the elastic and inelastic models presented herein . In the former case with high ALR, significant shears are needed to be transferred by the framing action of slab into the wall, which was not accounted for by the inelastic dynamic models, which considered slab elastic.

3.6. Summary and Conclusions

This article explores the capacity of state-of-the-art analytical procedures to forecast the observed failure in some shear walls of a relatively new RC building during the 2010, Chile earthquake. Previous experimental research on similar walls showed that a plausible failure mechanism was sudden and with limited ductility as a result of high axial compression stresses, poor boundary element confinement, and lack of wall ties. Although there is clarity on the effect of these factors on the wall behavior, the research question responded herein is if the geometry and magnitude of the observed damage could be anticipated by using the best of our current RC modeling procedures and software. This predictability of the observed wall behavior is important in the design of new buildings, as well as the retrofit of old ones, in order not to repeat this undesirable earthquake behavior in the future.

Planar inelastic pushover analyses were performed in DIANA using several RC shear walls as benchmarks to validate the regularization imposed on the stress-strain constitutive models based on the conservation of compressive fracture energy. The results obtained suggest to use as a stress-strain constitutive model either the parabolic model or the multi-linear model. This calibrated material models were used to study the inelastic static response of the two damaged walls in the building studied.

Because the walls analyzed are essentially cantilever elements coupled with other resisting planes by the floor slab, classical pushover analyses that only impose lateral displacements at the floor level are not capable of representing the observed damage in the walls. The reason is that lateral displacement patterns cannot account for the increase in axial load transferred into the walls by the slab shear. However, if the wall-slab interaction is included in the planar pushover analysis by imposing vertical nodal floor displacements according to

the predominant lateral mode in the direction of the wall, the results show the correct failure mode. Therefore, the imposed vertical displacements are intended to represent the additional vertical load carried by the wall as the overturning of the structure causes vertical unloading, or even tension, in the walls of the opposite side of the building. Although the pushover model and the assumption to account for this wall-slab interaction has evident limitations, pushover results in this case are consistent with those from an inelastic dynamic analysis, and the procedure may become an alternative to analyze in simpler terms the complex inelastic dynamic behavior of RC wall buildings.

Although all model results presented herein, pushover and dynamic, consistently show that the wall behavior was brittle, it is fair to say that it is not possible to completely discard that the wall damage could have been caused by a completely different mechanism with lighter axial loads and cyclic behavior. The sudden and brittle wall mechanism seemed more likely to the authors mainly because it showed consistency with some of the experiments and the dynamic lateral displacement demand necessary to produce wall failure. However, it is apparent that the modeling assumption used herein of linear behavior of the building slab may have led to some overestimation of the axial load in walls.

This previous conclusion does not imply necessarily that cyclic behavior did not play a role in the damage of these walls, but rather that the wall behavior was dominated by high axial stresses. Indeed, after spalling, buckling of the longitudinal reinforcement is likely to occur due to the cycling of loads, the large spacing of transverse reinforcement, and the high axial stresses. The question if this damage could have been prevented or delayed by a better detailing of transverse reinforcement is still a matter of research. Results in the literature with thin boundary elements [15] have shown that the non-ductile behavior observed at the boundaries of these walls is difficult to correct even with close spacing of transverse reinforcement.

In summary, under the set of modeling assumptions presented, and though still quite demanding numerically, available analytical models were able to predict for two shear walls of the building considered, the geometry and magnitude of the observed damage during the

earthquake as well as the lateral displacement demand expected. In the future these results should be validated with other ground motions and walls that underwent similar damage.

Acknowledgments

This research has been sponsored by the National Science and Technology Council of Chile, CONICYT, under grant Fondecyt 1141187, and by the National Research Center for Integrated Natural Disaster Management CONICYT/FONDAP/15110017. The authors are very grateful for this support.

REFERENCES

[1] Moroni O., and Gomez C. "Concrete shear wall buildings." World Housing Encyclopedia, Report 4.

[2] Pao J., Brzev S. "Concrete shear wall highrise buildings." World Housing Encyclopedia, Report 79.

[3] Mejia L.G., Ortiz J.C., Osorio L.I. "RC Structural Wall Buildings." World Housing Encyclopedia, Report 109.

[4] Kam W.Y., Pampanin S., Elwood K. (2011) "Seismic Performance of Reinforced Concrete Buildings in the 22 February Christchurch (Lyttelton) Earthquake." Bulletin of the New Zealand Society for Earthquake Engineering, 44(4), 239-278.

[5] Gómez CE. (2001) "Structural System Characteristics used in RC and Reinforced Masonry Building Construction in Chile." Civil Engineering Thesis 2001. University of Chile, 215 pp. (In Spanish).

[6] Guzmán MA. (1998) "Structural Characteristics used in Design of High Buildings in Chile." Civil Engineering Thesis 1998. University of Chile. (In Spanish).

[7] Jünemann R., de la Llera J.C., Hube M.A., Cifuentes L.A., Kausel E. (2015) "A statistical analysis of reinforced concrete wall buildings damaged during the 2010, Chile earthquake". Engineering Structures, 82 (2015) 168–185.

[8] Wood SL. (1991) "Performance of reinforced concrete buildings during the 1985 Chile earthquake: implications for the design of structural walls." Earthquake Spectra, 7(4): 607-638.

[9] Westenenk B., de la Llera J.C., Jünemann R., Hube M.A., Besa J.J., Lüders C., Inaudi J.A., Riddell R., Jordán R. (2013) "Analysis and Interpretation of Seismic Response of RC Buildings in Concepción during the February 27, 2010 Chile Earthquake." Bulletin of Earthquake Engineering; 11(1): 69-91.

[10] Westenenk B., de la Llera J.C., Besa J.J., Jünemann R., Moehle J., Lüders C., Inaudi J.A., Elwood K.J., and Hwang S-J. (2012) "Response of Reinforced Concrete Buildings in Concepción during the Maule Earthquake." Earthquake Spectra; 28(S1): S257-S280.

[11] Wallace J.W., Massone L.M., Bonelli P., Dragovich J., Lagos R., Lüders C., Moehle J. (2012) "Damage and Implications for Seismic Design of RC Structural Wall Buildings." Earthquake Spectra; 28(S1); S281-S299.

[12] Alarcon C., Hube M.A., de la Llera J.C. (2014) "Influence of axial load in the seismic behavior of RC walls unconfined wall boundaries." Engineering Structures; 73:13-23.

[13] Hube M.A., Marihuén A., de la Llera J.C., Stojadinovic B. (2014) "Seismic behavior of slender reinforced concrete walls." Engineering Structures; 80:377-388.

[14] Massone L.M., Polanco P., Herrera P. (2014) "Experimental and analytical response of RC wall boundary elements". Proceedings of the 10th National Conference in Earthquake Engineering, Earthquake Engineering Research Institute, Anchorage, AK.

[15] Arteta C.A., To D.V., Moehle J.P. (2014) "Experimental response of boundary elements of code-compliant reinforced concrete shear walls." Proceedings of the 10th National Conference in Earthquake Engineering, Earthquake Eng. Research Institute, Anchorage, AK.

[16] Galal K., El-Sokkary H. (2008) Advancement in modeling of RC shear walls." Proceedings of the 14th World Conference on Earthquake Engineering, Beijing, China.

[17] Takayanagi, T., Derecho, A.T. and Corley, W.G. (1979). "Analysis of Inelastic Shear Deformation Effects in Reinforced Concrete Structural Wall Systems." Nonlinear Design of Concrete Structures. CSCE-ASCE- ACICEB International Symposium. University of Waterloo, Ontario, Canada, pp. 545-579

[18] Vulcano, A., Bertero, V. V. and Colotti, V. (1988). "Analytical Modeling of RC Structural Walls." Proceedings, 9th world Conference on Earthquake Engineering, V. 6, Tokyo-Kyoto, Japan, 41-46.

[19] Massone, L.M., Orakcal, K. and Wallace J.W. (2006). "Shear–flexure interaction for structural walls." ACI special publication—Deformation capacity and shear strength of reinforced concrete members under cyclic loading. ACI-SP236-07,127–150.

[20] Magna-Verdugo C.E., Kunnath S.K. (2014) "Non-linear response analysis of reinforced concrete shear walls using multi-spring macro-models." Proceedings of the 10th National Conf. in Earthquake Engineering, Earthquake Engineering Research Institute, Anchorage, AK.

[21] Vásquez J.A., de la Llera J.C., Hube M.A. (2016) "A regularized fiber element model for reinforced concrete shear walls". Earthquake Engineering & Structural Dynamics, doi:10.1002/eqe.273.

[22] Spacone, E., Filippou, F. C., & Taucer, F. F. (1996). "Fiber Beam-Column Model for Non-Linear Analysis of R/C Frames: Part I. Formulation." Earthquake Engineering & Structural Dynamics, 25(7), 711–725

[23] Belmouden, Y., & Lestuzzi, P. (2007). "Analytical model for predicting nonlinear reversed cyclic behavior of reinforced concrete structural walls." Engineering Structures, 29(7), 1263–1276.

[24] NERHP (2014). "Recommendations for seismic design of reinforced concrete wall buildings based on studies of the 2010, Maule, Chile Earthquake." NIST GCR 14-917-25. US Department of Commerce.

[25] LSTC, 2013, LS-DYNA, Livermore Software Technology Corporation, Livermore, California.

[26] CSI (2013), Nonlinear Analysis and Performance Assessment for 3D Structures, PERFORM-3D, Computers and Structures, Inc., Berkeley, California, http://legacy.csiamerica.com/perform3d/overview.

[27] Feenstra P.H., de Borst R., and Rots J.G. (1991) "A comparison of different crack models applied to plain and reinforced concrete." Proceedings of the International RILEM/ESIS

Conference "Fracture Processes in Concrete, Rock and Ceramics", Noordwijk, The Nehterlands.

[28] TNO DIANA. (2010). DIANA - User's Manual.

[29] Hube M.A. and Mosalam K.M. (2011). “Experimental and computational evaluation of in-span hinges in reinforced concrete box-girder bridges.” Journal of Structural Engineering, Vol. 137, No. 11, pp. 1245-1253.

[30] Quitral F. (2013) “Non-linear brittle behavior of shear wall buildings during 2010 Chile earthquake.” Master of Science Thesis. Pontificia Universidad Católica de Chile. (in Spanish)

[31] Comité Euro-International du Béton. (1990). CEB-FIP model code 1990, Thomas Telford, London.

[32] Nakamura, H., & Higai, T. (2001). “Compressive fracture energy and fracture zone length of concrete.” Modeling of Inelastic Behavior of RC Structures under Seismic Loads, p471-487.

[33] Karthik M., Mander J. “Stress-block parameters for unconfined and confined concrete based on a unified stress-strain model.” Journal of Structural Engineering 2011; 137 (2):270-273.

[34] Scott, B., Park, R., & Priestley, M. (1982). “Stress-strain behavior of concrete confined by overlapping hoops at low and high strain rates.” ACI Journal Proceedings, (79), 13–27.

[35] Dazio A., Beyer K., and Bachmann H. (2009) “Quasi-static cyclic tests and plastic hinge analysis of RC structural walls.” Engineering Structures; 31:1556-1571

[36] Dazio A., Wenk T., Bachmann H. Versuche an Stahlbetontragw änden unter zyklisch-statischer Einwirkung (Tests on RC walls under cyclic-static action). IBK report no. 239. Birkhäuser; 1999. http://e-collection.ethbib.ethz.ch/view/eth:23296.

[37] Thomsen IV, J.H. and Wallace, J.W. (1995). “Displacement Based Design of RC Structural Walls: an Experimental Investigation of Walls with Rectangular and T-Shaped Cross-Sections.” Report No. CU/CEE-95/06, Department of Civil and Environmental Engineering, Clarkson University, Potsdam, NY.

[38] Computers and Structures, Inc. (2010). CSI Analysis Reference Manual for SAP2000, ETABS, SAFE and CSIBridge. Berkeley, California.

[39] D.S. N 61 MINVU. Building seismic design code, replacing D.S N 117, 2010. Chilean Ministry of Housing and Urbanism, Diario Oficial; 13 December 2011[in Spanish].

[40] Universidad de Chile. Departamento de Ingeniería Civil and Oficina Nacional de Emergencia Chile (ONEMI). Earthquakes of Chile; 2010. http:// terremotos.ing.uchile.cl/2010 [in Spanish] [accessed 21.02.14].

[41]Rodriguez, M.E., Botero J.C., and Villa, J. (1999), "Cyclic Stress-Strain Behavior Of Reinforcing Steel Including Effect Of Buckling" Journal of Structural Engineering, ASCE, Vol. 125, No. 6. June, Pages 605-612.

[42] MathWorks Inc. MATLAB version R2011b.

[43] E. Hinton, T. Rock, O.C. Zienkiewicz, "A note on mass lumping and related processes in the finite element method." Earthquake Engineering and Structural Dynamics. 4 (3) (1976) 245-249.

[44] Su, R. K. L., & Wong, S. M. (2007). "Seismic behavior of slender reinforced concrete shear walls under high axial load ratio." Engineering Structures, 29(8), 1957-1965.

[45]Segura, C., and Wallace J. (2915). "Experimental Study on the seismic performance of thin reinforced concrete structural walls". SEFC 2015 Proceedings, Tokyo Institute of Technology, Yokohama, Japan

4. EARTQUAKE DAMAGE ASSESMENT OF REINFORCED CONCRETE SHEAR WALL BUILDINGS USING A 3D FINITE ELEMENT MODEL

R. Jünemann[a], J.C. de la Llera[a], and M.A. Hube[a],

[a] *National Research Center for Integrated Natural Disaster Management CONICYT/FONDAP/15110017 and Department of Structural and Geotechnical Engineering, Pontificia Universidad Católica de Chile, Vicuña Mackenna 4860, Santiago, Chile*

ABSTRACT

Finite element models have been widely used to predict analytically the seismic behavior of structures. Motivated by the failure observed in some reinforced concrete shear wall buildings during recent earthquakes, this article presents the results of a 3D inelastic finite element (FE) model of an actual building damaged during the 2010, Chile earthquake, in which damage was localized in shear walls of the first basement. The three-dimensional finite element model of the building uses 4-node shell elements and was developed in the software DIANA. The inelastic behavior was concentrated in vertical elements located at first story and basements, where concrete was considered using the total strain rotating crack model, and reinforcement was modeled using an embedded formulation. Inelastic dynamic analyses were performed considering a single ground motion record obtained in the vicinity of the building during the earthquake, and results are compared with the actual building damage. These results show that the model predicts an abrupt localized failure in some critical walls, in a pattern similar to the one observed after the earthquake. Additionally, it is shown that the dynamic response causes an important increase in axial load of RC walls relative to the initial gravitational condition. This factor is critical in producing the localized flexural-compressive failure observed. Finally, a parametric study is presented to evaluate the sensitivity of the FE response to changes in modeling assumptions. Different modeling assumptions produce changes mainly of the instant and sequence of failure; however, all models show an abrupt collapse of the critical

walls that were damaged during the earthquake, for high axial load ratios. Therefore, the proposed FE model could be used in practice to assess the condition of an existing shear wall building and eventually propose a retrofit strategy.

4.1. Introduction

During severe earthquakes over the last decade, reinforced concrete (RC) wall buildings have shown a type of brittle damage in walls characterized by concrete crushing at wall boundaries localized over a short height and a crack that propagates toward the interior of the wall. Additionally, reinforcement buckling and fracture at wall boundaries and global wall buckling have been observed.

Research on the brittle failure observed in RC walls has been mainly focused on analytical and experimental work on isolated RC wall specimens ([1][2][3][4][5][6]). However, studies regarding 3D models of damaged structures are very limited. Results on pushover analysis of isolated damaged walls and the results of a different dynamic inelastic analysis (Jünemann *et.al* [7]) have shown that the 3D interaction of the walls with the rest of the structure is a key factor in understanding the behavior of this type of structures. Kozmidis *et.al* [8] developed a nonlinear dynamic analysis on a tall RC building damaged during the 2010 earthquake using nonlinear fiber elements in Perform 3D. Although the proposed model showed concrete crushing in several building locations, the damage locations did not coincide accurately with the ones observed after the earthquake. Furthermore, the collapse of the Alto Río building during the 2010 Chile earthquake was studied using a 3D finite element model using shell elements of a representative slice of the building in the software LS-DYNA [9]. The study shows that bar buckling has a major effect on the cyclic response of the RC tested walls, and thus, this effect should be included in the FE model used. The model was able to simulate a behavior consistent with the one of building collapse, governed by flexure induced concrete crushing. On the other hand, Ebrahimian *et.al* [10] developed a 3D nonlinear FE model in the software DIANA for the pre-test numerical simulation of a full scale five-story RC building specimen tested on the NEES-UCSD shake table. In this case, a *total strain rotating smeared crack* model was used for concrete, and results show

that the nonstructural components have significant influence on the seismic response of the building, leading to some discrepancy between the predicted response by FE and the response measured for low intensity earthquakes, i.e. when nonstructural elements remain elastic increasing the stiffness of the system. Additionally, results showed that the constitutive stress-strain model for concrete was not able to capture the pinching hysteretic behavior of real RC flexural members (beams and columns).

The fundamental research question of this article is if we are able to reproduce the observed damage in a real building during the 2010 Chile earthquake using a dynamic 3D inelastic FE model in a software like DIANA. And in doing so, which are the key modeling aspects and assumptions to achieve this objective. Therefore, this article studies these modeling assumptions in a real structure damaged during the 2010, Chile earthquake. The geometry of the selected building is complex but typical for these types of residential structures. The observed damage in the building was localized in the first basement. To make comparisons easier with the original design of the structure, a complete 3D FE model of the building was developed in ETABS [11] assuming elastic behavior, and then an inelastic FE model of the entire building was developed using the software DIANA [12], which allows for material nonlinearity. In the latter, the inelastic behavior was concentrated in the vertical elements located in the first story and basements. Concrete behavior was modeled using the *total strain rotating crack model*, while reinforcement was modeled using an embedded formulation. The building model was subjected to a ground motion recorded closest to the building during the 2010 Chile earthquake. First, the two horizontal components of the seismic record were applied independently to the critical direction of the building. Then, the 3 components were applied simultaneously. Results show an abrupt compression failure of the critical walls as the strongest component of the seismic record is applied. Finally, a parametric study is carried out that evaluates the different modeling assumptions. The variables analyzed are the amount and location of the inelastic elements considered, and the stiffness of the slab.

4.2. Building description

The selected building is located in Santiago, Chile, and suffered severe damage in RC walls during 2010 earthquake, like other RC shear wall buildings located in Santiago, Viña del Mar and Concepción [13][14][15]. The building is part of a complex composed by 4 independent and similar towers (Figure 4-1a)), and the focus will be placed on Tower 3 ("the building"), which is a mirror of Tower 2. It is a residential building with 18 stories and 2 basements, and has a typical "fish-bone" like configuration with central longitudinal walls in the East-West direction, and orthogonal walls in the North-South. Figure 4-1b) shows a 3D view of the building model, while Figure 4-1c) shows the first basement floor plan. The building is composed of 15 cm thick floor slabs and typical 20 cm thick RC shear walls with an average total wall density of 6.5% (total area of walls in all directions divided by tower area, calculated at the first level above grade). The building was designed with f_c'=25MPa concrete compressive strength and steel A630-420H (f_y=420 MPa). The basements are destined to car parking and present an enlarged floor plan area with RC columns in the extended underground zone.

Field investigations conducted after the earthquake showed that most severe damage was localized in the transverse RC walls of the north side of the building in the first basement level (Figure 4-1c)). Concrete crushing and reinforcement buckling was observed, particularly in walls at axis Q, U and N1 (Figures 4-2a), b) and c)), which affected almost the entire length of the wall, compromising the vertical stability of the elements. Additionally, global wall buckling was observed in some cases. These walls present a similar configuration in height, with an irregularity in the wall length in the transition between the basements and the first story were the damage was concentrated, as is schematically shown in Figure 4-1d) for wall Q. Additionally, beams located in axis 10 were damaged in the joint with the previously mentioned walls. Walls in axis O and X suffered moderate damage at first basement (Figure 4-2d) and e)). Finally, damage was observed in first basement column in axis 10 between axis Q and U (Figure 4-2f)). The vertical elements in axis 10 between axis Q and O also showed local damage and loss of concrete cover (Figure 4-2g)). No

significant damage was reported on RC slabs. It is interesting to notice that Tower 2 (mirror of Tower 3), suffered almost the same damages than the previously described for Tower 3, but additionally, concrete crushing and reinforcement buckling was observed at the opposite side wall N2 (Figure 4-1c)). In this case, the damage was concentrated at the base of first story level, as shown in Figure 4-1h).

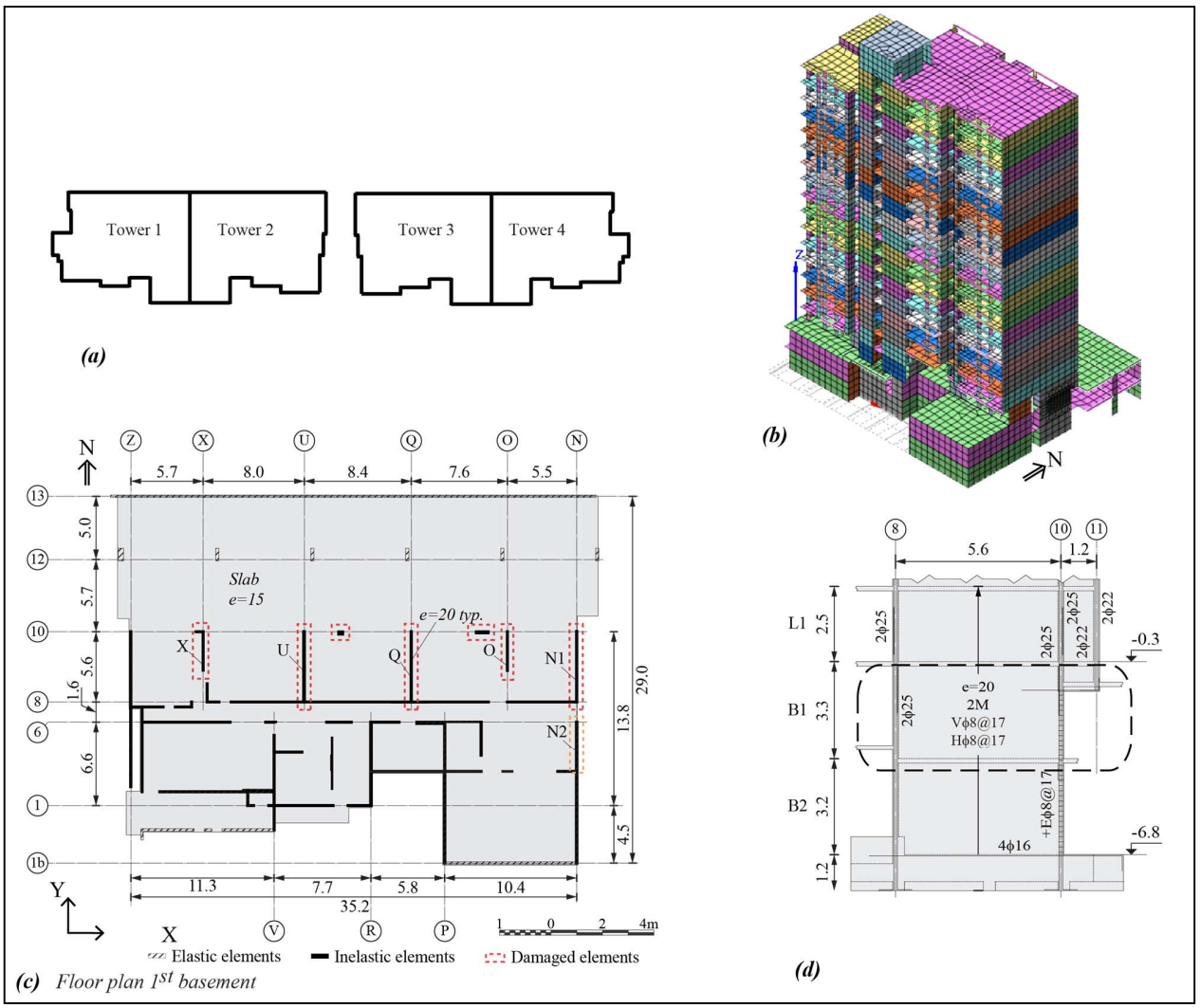

Figure 4-1: a) Building complex; b) general 3D view of building model in DIANA; c) first basement floor plan; and d) elevation of wall Q.

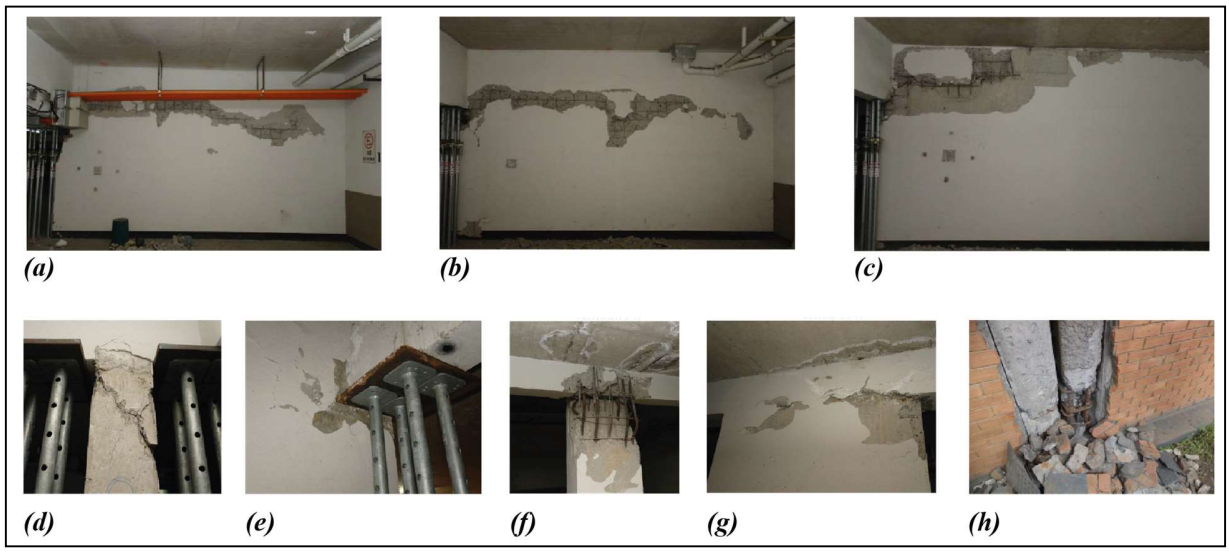

Figure 4-2: Observed damages in first basement of analyzed building: a) wall at axis U; b) wall at axis Q; c) wall at axis N1; d) wall at axis O; e) wall at axis X; f) column at axis 10, between axis Q and U; g) vertical element at axis 10, between axis O and Q; and h) first story wall N, Tower 2. (Damage information thanks to Sopoerer y Asociados)

4.3. Elastic finite element models

A reference elastic model of the building was developed in ETABS [11] using conventional modeling assumptions (i.e. gross cross element cross section and uncracked stiffness), and the same elastic model was developed in DIANA [12], in order to compare elastic responses of both analytical models and validate the DIANA elastic model.

Both models considered shell elements for walls and slabs, and beams were modeled with frame elements including shear. For the DIANA model, walls and slabs are modeled using three or four node triangular or quadrilateral iso-parametric curved shell elements with five degrees of freedom per node (three translations and two rotations), based on linear interpolation and Gauss integration, considering a 2x2 integration scheme over the element area. Basement levels were included in the model and all nodes at the base were restricted from lateral and vertical displacements. No rigid diaphragms were included at floor levels

and the effect of surrounding soil at basements was neglected. The self-mass of the structural elements corresponding to the dead loads plus 25% of the live loads (D+0.25L) was included in both models. Damping is included as 2.7% modal in the ETABS model, while in the DIANA model it is included through Rayleigh proportional damping defining 3% damping at 1.2 times the first elastic period and for the elastic period for which the mass participation factor was more than 75% in both principal directions.

The fundamental period of the building is T_y=0.87 s in the ETABS model and 0.86 s in the DIANA model, both in the N-S direction. The first ten periods of the building present differences lower than 8% between both elastic models, which is within the acceptable range for different FE models [16]. The vertical support reaction for gravity loads is 100,918 kN for the ETABS model and present a difference lower than 0.5% with the DIANA model.
An elastic response history analysis was developed considering simultaneously the three components of the ground motion recorded in the nearby station Peñalolen [17]. The seismic record considered is shown in Figure 4-3a). In order to efficiently develop inelastic analysis in the subsequent sections, a significant duration of the seismic records between 5% and 95% of the Arias Intensity [18] was considered in the numerical simulations, as shown in gray color in Figure 4-3a). Figures 4-3b) and c) show pseudo-acceleration and displacement spectrum, respectively. In order to estimate the roof displacement demand imposed by the earthquake, recommendations given by the Chilean supreme decree D.S. N 61 [19] were considered, i.e. $\delta_u = 1.3S_d(T_{cr})$, where $T_{cr} = 1.5T_y$, is the estimated cracked period of the structure in the direction of analysis. The estimated displacement demands are 17.2 cm and 23.3 cm for E-W and N-S components, respectively. The elastic T_y and estimated cracked T_{cr} periods of the building are shown in Figure 4-3c), with the corresponding spectral displacements. For the elastic period T_y, the estimated roof displacements ($\delta_u = 1.3S_d(T_y)$) are 7.02 cm and 15.08 cm for the N-S and E-W components, respectively. Please notice that in this case the estimation for the E-W component is more than twice the estimation for the N-S component, while this trend is reversed for the cracked period T_{cr}. For this reason, in the subsequent section both N-S and E-W components of the seismic record are applied to the critical direction of the building.

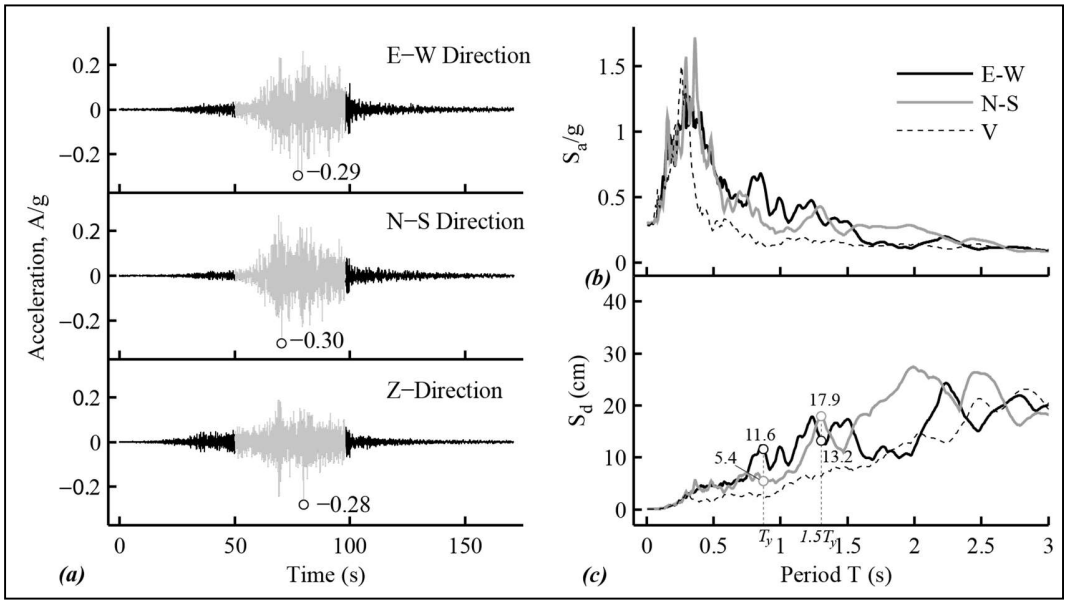

Figure 4-3: a) Ground motion record Peñalolen; b) elastic pseudo-acceleration spectrum; and c) elastic displacement spectrum.

Figures 4-4a) and b) show displacement of the center of gravity at the roof level (δ_r) and normalized base shear in N-S direction for both elastic models, respectively. The peak roof displacements are 9.5 cm for the ETABS model and 9.3 cm for the DIANA model, which occurs at 80.6 s. These values present a difference of 1%, and correspond to a roof drift of 0.18%. The difference between both models for the peak normalized base shear is 7%. Additionally, Figure 4-5) shows the axial load ratios (ALR) and bending moment for the first basement critical elements (i.e. walls at axis Q, U and N1). The axial load ratios are calculated as ALR=$N/f_c'A_g$, where N is the axial load in the critical section, A_g the gross section area and f_c' concrete compressive strength. The axial load in the critical section N is calculated as the sum of the nodal forces of all nodes that compose the section. The bending moment M is calculated as the moment of the same nodal forces with respect to the center of gravity of the section. The critical section considered to calculate ALR and M is located 2.07 m above the second basement, as schematically shown in Figure 4-8, and negative values of ALR correspond to compression in the critical section. The section cut considered for walls U and N1 is rectangular, while for wall Q has T-shape with a flange length of 2.96 m according to the dimension of the element from first story and up. Figure 4-5a) shows

gravitational and seismic ALRs for the three critical walls, and the response is very similar for both analytical models, showing differences lower than 7% for peak ALRs. Finally, Figure 4-5b) shows the bending moment *M* at critical section of walls Q, U and N1 for both models versus roof displacement δ_r. Again results are very similar, which validates the DIANA elastic model.

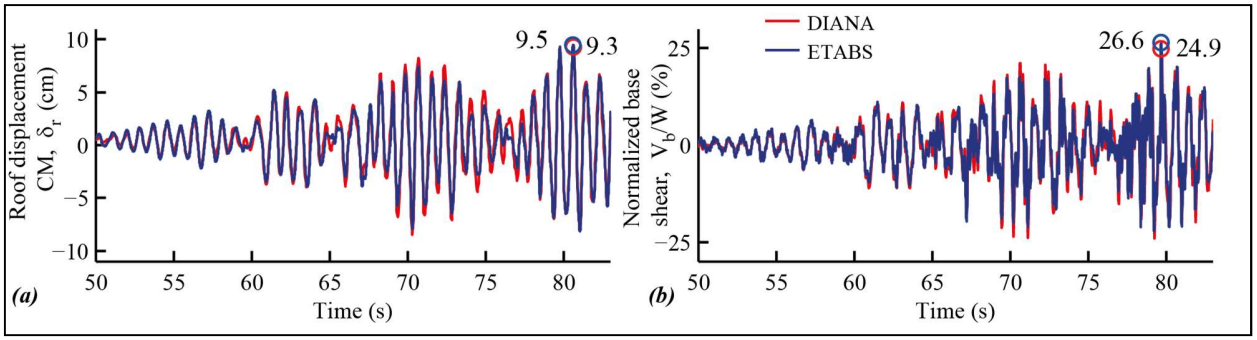

Figure 4-4: Linear elastic response in the N-S direction: a) roof displacement; and b) normalized base shear.

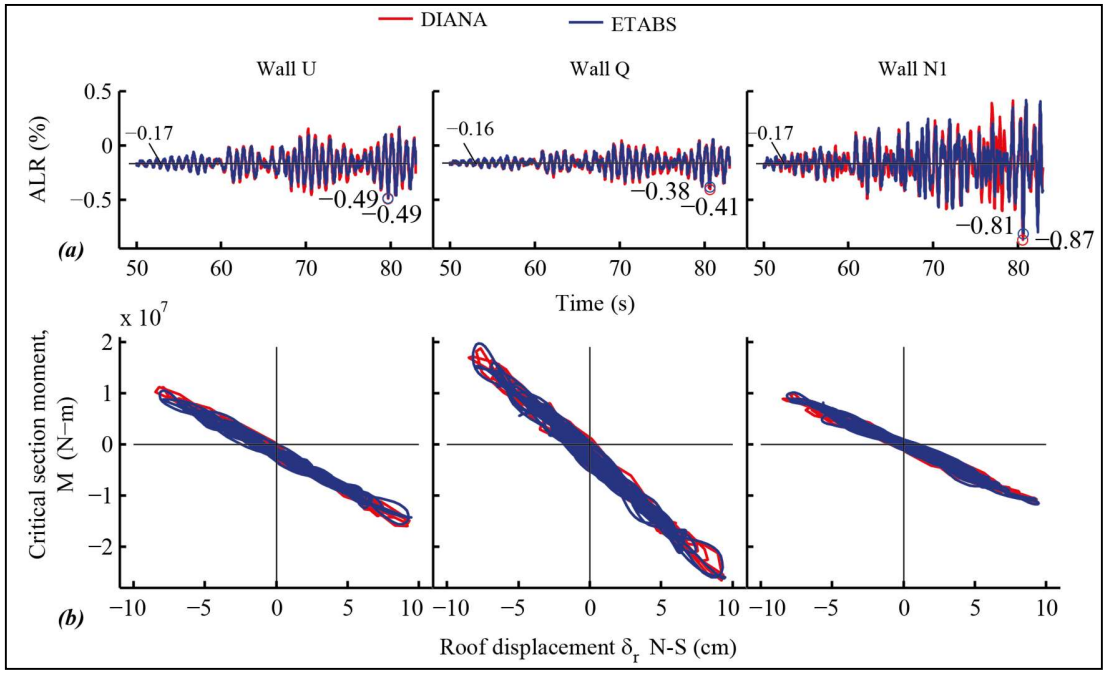

Figure 4-5: Linear elastic response for first basement critical walls U, Q and N1: a) axial load ratio; and b) bending moment versus roof displacement.

4.4. Inelastic finite element model

The approach followed in this section is based on finite element models with inelastic material behavior using the software DIANA [12]. As the building damage after 2010 earthquake was concentrated in the first basement (B1), all vertical elements at the first three levels of the building (i.e. L1, B1 and B2) were modeled with inelastic behavior, with the exception of perimeter walls and columns at axis 12 (Figure 4-1c)). Since no significant damage was reported on other elements, the rest of the structure is modeled with linear elastic behavior as described in Section 4.3, including slabs.

To model concrete behavior, the *smeared cracking* approach is considered, following *total strain rotating crack* model. In this approach, concrete fracture is considered within a continuum with a stress-strain constitutive model with softening for both compressive and tensile behavior, while the principal axes rotate with the principal strains during crack propagation. Compressive stress-strain constitutive for concrete is modeled using the Parabolic curve implemented in the software, which adjusts the stress-strain relationship based on the element size in order to keep the compressive fracture energy constant, which minimizes the mesh-size effects. This model has been evaluated elsewhere showing good results for 2D RC walls over other constitutive models predefined in the software [7]. The walls presented almost no boundary confinement, thus only non-confined concrete was considered. Three effects are included for concrete behavior according to software available options [12]: increase of strength due to lateral confinement; compression softening effect; and decrease in Poisson's ratio with increased cracking. For tensile behavior, Hordijk constitutive model is used. Figure 4-6a) shows the theoretical stress-strain constitutive relation used for concrete in this case, based on the material properties defined in Section 4.2 and mesh size considered in the finite element model. The unloading and reloading are modeled through a function that is linear to the origin, implying that no residual strains appear after unloading. Walls and slabs were modeled with the curved shell elements described in Section 4.3.

Reinforcement is modeled using an embedded formulation, which assumes perfect bonding. The stress-strain constitutive model for steel is equal in tension and compression and considers exponential hardening (Figure 4-6b)). This model does not include the effect of bar buckling or fracture since the software does not allow the use of different behavior in each direction of the reinforcement bars. This is a limitation of the proposed model, since both effects were observed in damaged walls after 2010 earthquake and have shown to have significant impact on the cyclic behavior of RC walls [9].

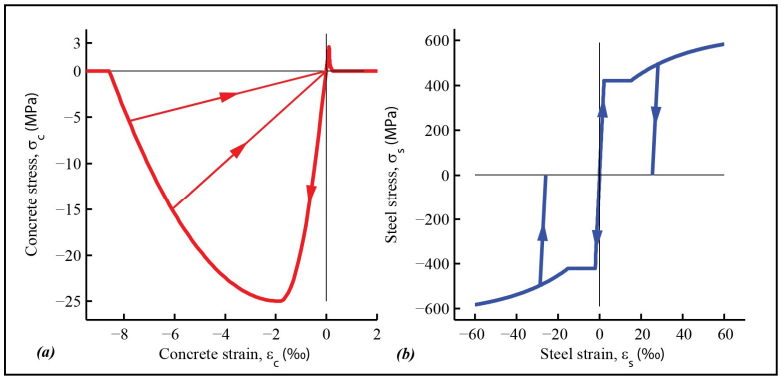

Figure 4-6: Material uniaxial stress-strain behavior: a) concrete; and b) steel.

Gravity loads are applied as a first load case and equilibrium is achieved through regular iterative Newton-Rapshon method. For nonlinear dynamic analysis, the seismic record is applied as base excitation after application of the gravity loads. The equations of motion in time are integrated through Newmark's method with a maximum step size of 0.01 s, while the solution of the nonlinear dynamic equilibrium equations are solved through Newton-Raphson method with secant stiffness matrix with a convergence criterion based on energy norm with a relative tolerance of 10^{-4}.

4.5. Inelastic dynamic response

This section presents results for dynamic inelastic analysis considering different inputs summarized in Table 4-1, where AA-B means that AA component of the seismic record is applied to B direction of the building. First, the two horizontal components of the seismic record presented in Section 4.2 where applied separately to the Y direction of the building (*I1* and *I2*). Then, the three components of the seismic record were applied simultaneously

to the building (*I3*), and finally, the horizontal components are switched in the direction applied (*I4*). As will be discussed later, building response is sensitive to the seismic record considered, showing an abrupt failure for cases *I2* and *I4*, while almost no inelastic incursion for cases *I1* and *I3*.

Table 4-1: Dynamic analysis inputs

Input ID	Ground motion component-building direction
I1	NS-Y
I2	EW-Y
I3	NS-Y, EW-X, V-Z
I4	EW-Y, NS-X, V-Z

4.5.1. Input I1: NS ground motion component applied to Y direction of the building

Figure 4-7 shows roof displacement and normalized base shear for both elastic (LRHA) and inelastic (NLRHA) DIANA models subjected to N-S component of the seismic record. Around time 62 seconds, differences between both models appear, which is attributed to concrete cracking in tensioned elements. Figure 4-7a) shows that the inelastic model reaches a roof displacement of 7.62 cm, which corresponds to a roof drift of 0.16% at a time 79.01 s, which is lower than maximum roof displacement of the elastic model (8.92 cm) for this seismic record. Similarly, the peak normalized shear for the inelastic model is also lower than the peak for the elastic model (Figure 4-7b)).

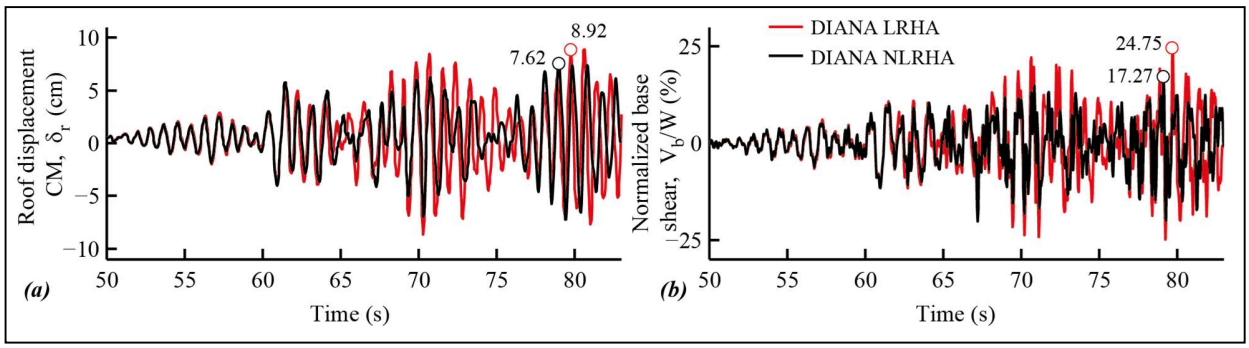

Figure 4-7: Inelastic dynamic response for I1 in the N-S direction: a) roof displacement; and b) normalized base shear.

Figure 4-8 shows schematically the location of the critical section and integration points for critical walls U, Q and N1 (Figure 4-1b)). The critical section is located 1.03 m below B1 level, and the finite elements 1-5 correspond to the critical elements of each wall, each of them with four integration points. Figure 4-9 shows concrete stress-strains curves in the vertical direction at the integration point indicated in Figure 4-8 of element 1. For walls U and N1, the integration point remains in the linear-elastic range in compression, while for wall Q, the integration point shows higher concrete strains, however, concrete strains are lower than $2x10^{-3}$ for all walls, i.e., no significant concrete crushing occurs.

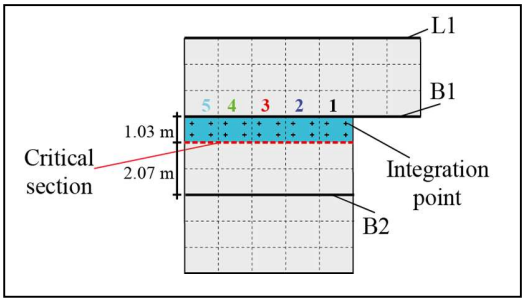

Figure 4-8: Scheme of critical section and integration points of critical walls.

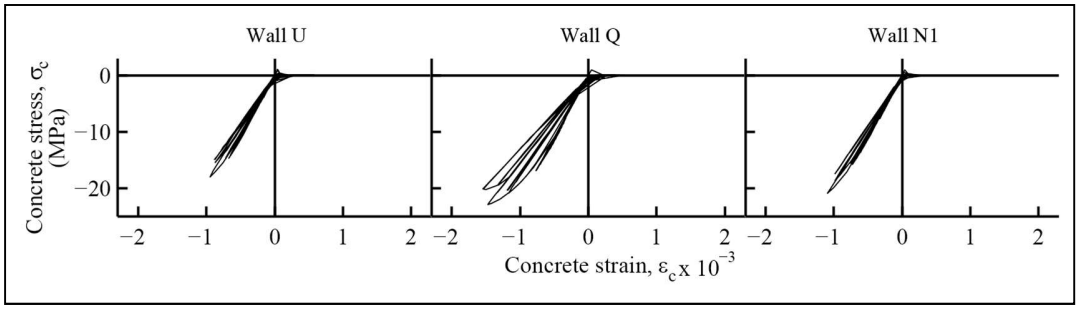

Figure 4-9: Local response for I1: concrete stress-strains at one integration point of critical element walls U, Q and N1.

Figure 4-10a) shows the history of the ALRs in the critical section of each wall for both elastic and inelastic models, where the ALR for gravity loads (ALR_0) are 17%, 16% and 17% for walls U, Q and N1, respectively. The ALRs for the inelastic model are lower than the ALRs for the elastic model for the three walls not only in tension (positive) but also in compression (negative). As the concrete cracks due to tensile stresses, the critical walls are not able to reach tensile ALRs as high as in the elastic model. Additionally, as opposite walls

crack in tension, critical walls in compression are not able to reach compression ALRs as high as in the elastic model either. However, the dynamic amplification factors of ALRs (i.e. $max(ALR)/ALR_0$) are 2.35, 1.81 and 2.71 for walls U, Q and N1, respectively, which show a significant increase in axial loads due to dynamic effect. Figure 4-10b) shows the bending moment at the critical section versus the roof displacement δ_r. It is clear that the walls remain in the elastic range for positive roof displacements (i.e. walls in compression), however, the bending moment for negative roof displacements is much lower than for the elastic model due to concrete cracking in the inelastic model. For negative roof displacements, the axial load at north-side walls diminishes and concrete cracks in tension, changing the position of the axial load in the wall section with respect to the elastic case, which reduces the bending moment in the section for small strains without steel yielding. Finally, Figure 4-11 shows the theoretical nominal capacity curves and the pairs P-M for elastic and inelastic DIANA models and for the three critical walls. Please notice that in this case, the signs of the axial load and bending moment have been inverted. Results show that for this input, the elastic behavior exceeds wall capacity only in tension, but not in compression, thus a concrete compressive failure in these walls is not expected. In summary, dynamic results for this input does not predict the wall failure observed after the earthquake, walls remain essentially in the elastic range with the exception of concrete cracking, and results show to be consistent with the elastic results.

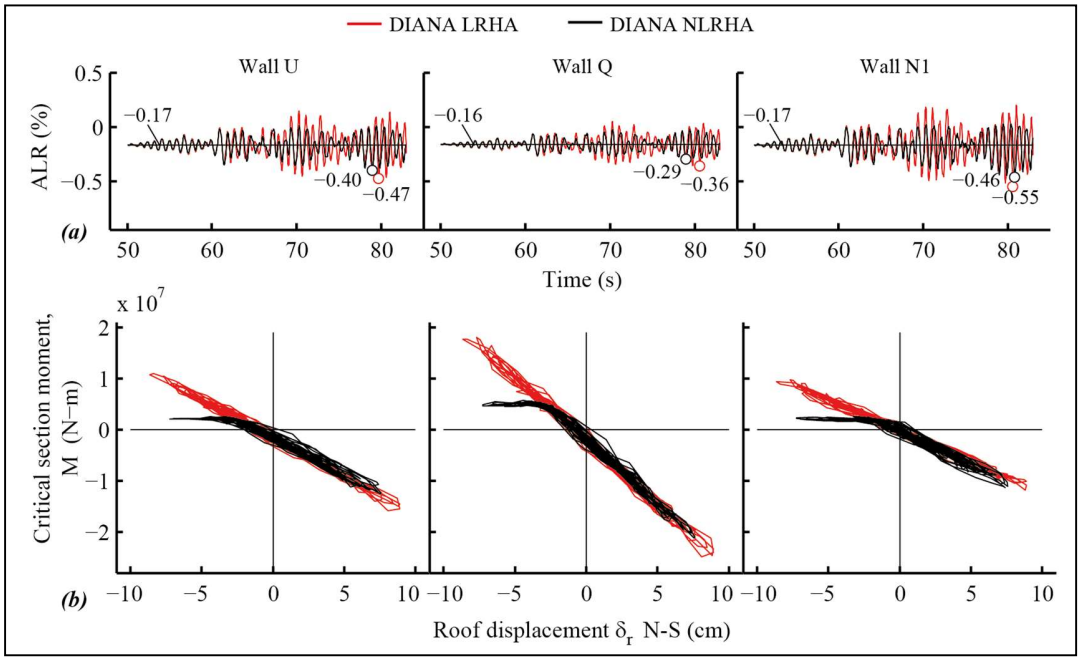

Figure 4-10: Local response of critical walls for I1: a) axial load ratio history; b) bending moment versus roof displacement history; and c) concrete plastic strains at failure moment.

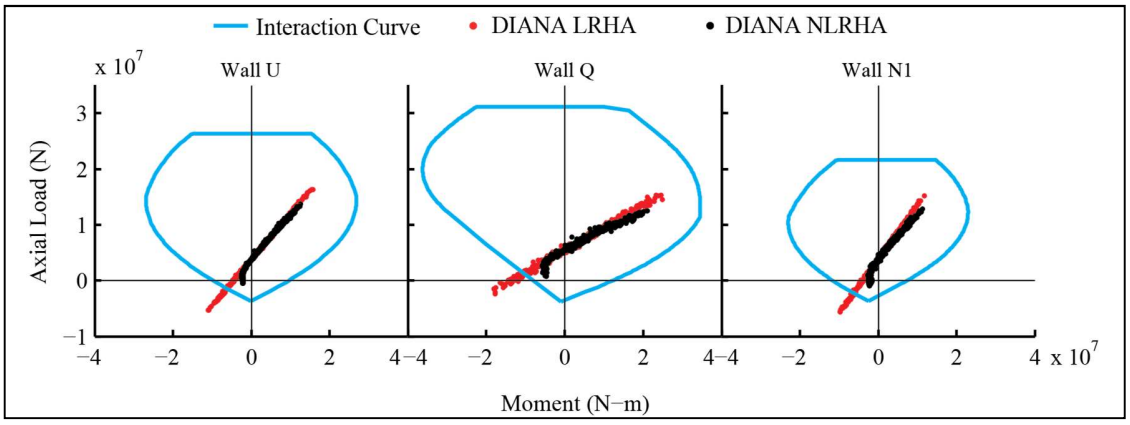

Figure 4-11: Local response for I1: Interaction curves P-M and axial load vs moment for critical walls.

4.5.2. Input I2: EW ground motion component applied to Y direction of the building

The E-W component of the ground motion is applied to the Y direction of the building. In this case, an abrupt failure is observed, as shown in Figures 4-12 to 4-15. Figure 4-12a) and b) show the roof displacement history and the normalized base shear history, respectively for both elastic (LRHA) and inelastic (NLRHA) models. In this case, maximum

displacements and base shear are higher than for the N-S component of the seismic record (Figure 4-7), which was expected since both pseudo-acceleration and displacement spectrum are higher for the E-W component than for the N-S component of the seismic record for the range of periods under consideration (Figure 4-3c)). The maximum roof displacement for this input is 21.4 cm for the inelastic model at t=80.3 s, which is within the estimated seismic demand (17.2 cm - 23.3 cm). This displacement corresponds to a roof drift of 0.5%, which is lower than the drifts estimated by Wallace *et.al.*[13] for vulnerable buildings above 15 stories, of 0.8% to 1%.

Figure 4-12b) shows the normalized base shear for both models. The maximum for the elastic model is 45.3% while the maximum for the inelastic model is 24.5%, which traduces in an effective inelastic reduction factor R_e=1.85. This R_e factor can be compared with the effective spectral reduction factor R**, which correspond to the ratio between the elastic response base shear and the design response base shear amplified by the factor 1.4. This effective factor takes into account the effect of minimum base shear requirement and the 1.4 amplification factor for evaluation at ultimate load. For this particular building, R** is estimated as 3.1, which is 65% larger than the estimated value of R_e. Additionally, R** has been studied for a large database of Chilean buildings [20], and for a building period around 0.85 s, the estimated R** vary between 2.5 to 5.5, with a mean value of approximately 3.5.

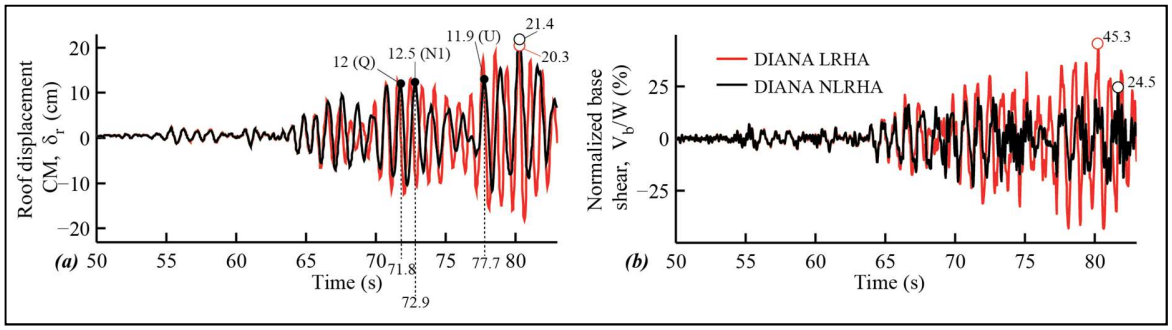

Figure 4-12: Inelastic dynamic response for I2 in the N-S direction: a) roof displacement; and b) normalized base shear.

Shown in Figure 4-12a) are three particular instants at t=71.8 s, t=72.9 s and t=77.7 s, which correspond to failure of walls Q, N1 and U, respectively for roof displacements of 12 cm,

12.5 cm and 11.9 cm, which correspond to drifts of approximately 0.3%. Failure in compression is defined herein as the instant when vertical concrete strains exceeds 0.5% in more than one element, which is clearly observed in Figure 4-13, which shows the histories of vertical concrete strains for one integration point for the five elements that compose each critical section of the analyzed walls (Figure 4-8). It is clear that an abrupt increase in concrete strains occurs for most of the elements in the three walls, reaching values higher than 0.5%, which is a clear sign of concrete crushing and damage of the wall.

For wall Q the failure occurs at t=71.8 s (Figure 4-13b)), for a roof displacement of 12 cm (Figure 4-12a)), and for an ALR of 35% (Figure 4-14a)). The instant of failure at wall N1 occurs at t=72.9 s, (Figure 4-13c)) for a roof displacement of 12.5 cm (Figure 4-12a)), and for an ALR of 63% (Figure 4-14a)). Finally, the failure of wall U occurs at t=77.7 s, (Figure 4-13a)) for a roof displacement of 11.9 cm (Figure 4-12a)), and for an ALR of 46% (Figure 4-14a)). Additionally, Figure 4-14b) shows an abrupt loss of bending capacity at the failure point of each wall. Finally, Figure 4-15 shows the concrete plastic strains just after the failure of these walls, which are concentrated in the critical section, very similar to the damage pattern observed after the earthquake in these walls (Figure 4-2a), b) and c)).

It is clear that for this input an abrupt compressive failure is observed in the critical walls. It is also observed that elastic and inelastic responses differ significantly in this case, since significant inelastic incursion of the elements occurs.

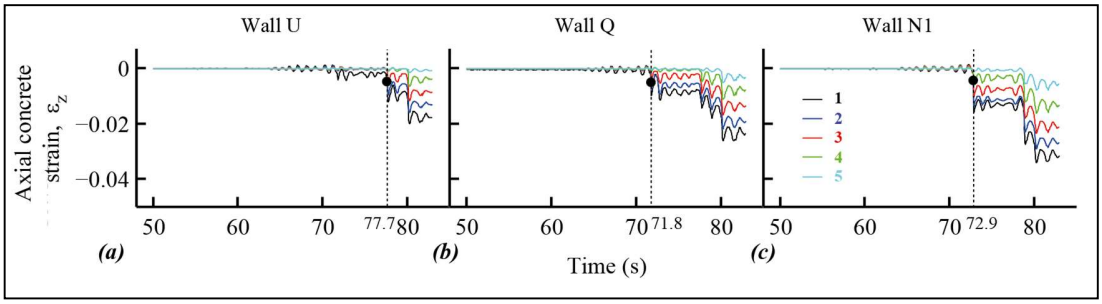

Figure 4-13: Local response for I2: concrete strain in one integration point of five elements at critical section: a) wall U; b) wall Q; and c) wall N1.

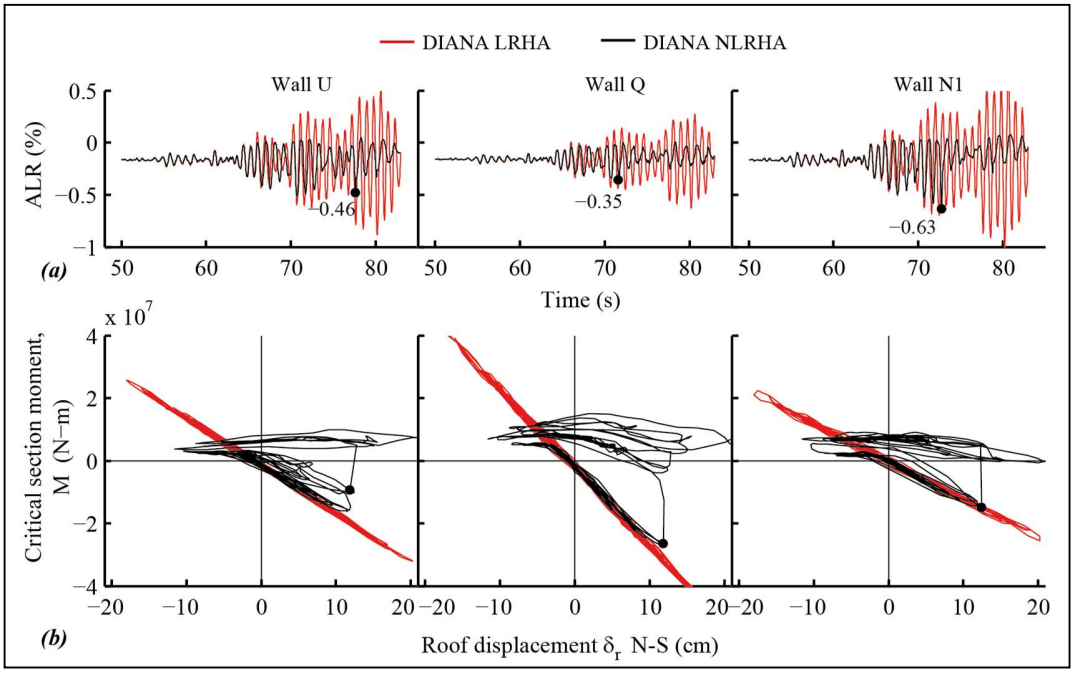

Figure 4-14: Local response of critical walls for I2: a) axial load ratio history; and b) bending moment versus roof displacement history.

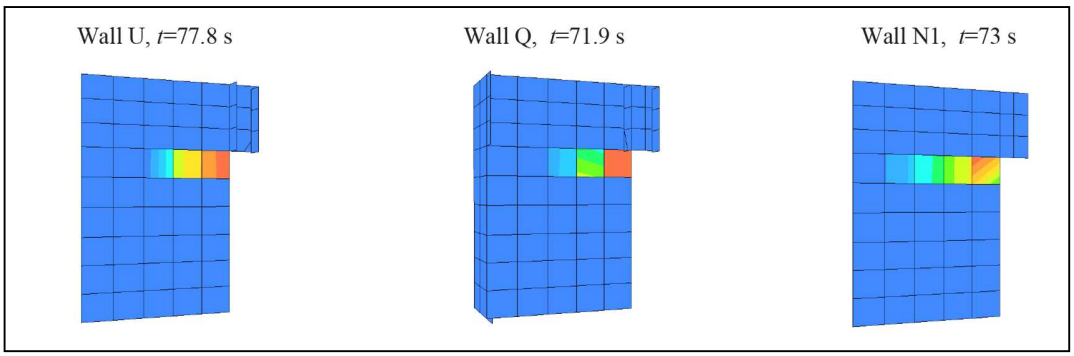

Figure 4-15: Concrete plastic strains after failure instant for critical walls U, Q and N1 for input I2.

Figure 4-16 shows the pairs P-M for input *I2* for both elastic and inelastic DIANA models, with the nominal interaction curves for the three critical walls. Please notice that again, the signs of the axial load and bending moment have been inverted. For input *I2*, the elastic demand exceeds wall capacity in compression for the three walls, thus wall flexural-compression failure was expected, as predicted by the inelastic response. In addition to the theoretical interaction curve, a reduced interaction curve has been included, calculated with the effective maximum strength of concrete. The lateral effects included in the DIANA

inelastic model reduce the maximum compressive strength to approximately 21 MPa instead of the nominal 25 MPa. With this consideration, the compressive failure shown in Figure 4-16 is consistent with the effective interaction curve. Additionally, in the case of wall U, an interaction curve considering the effective section is also shown, since one of the elements of this section fails previously to the rest of the elements.

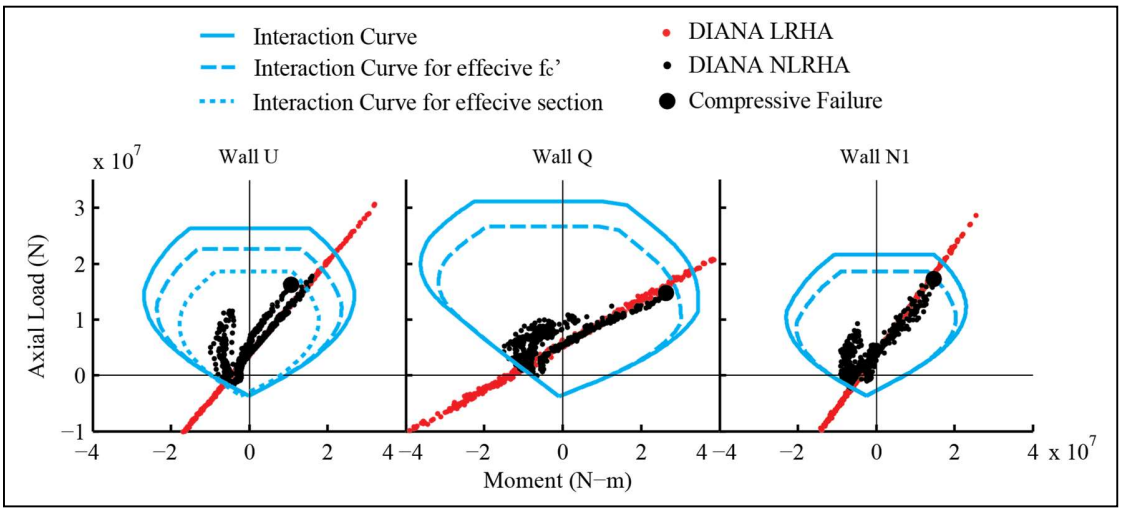

Figure 4-16: Local response for I2: Interaction curves P-M and axial load vs moment for critical walls.

Additionally, significant concrete crushing and loss of capacity was observed in walls N2 and O as shown in Figure 4-17a) and b), respectively. The analytical failure in both walls is also consistent with the damage observed after the earthquake (Section 4.2, Figure 4-1c)). Wall O present compressive failure at t=78.9 s, for an ALR of 46% (Figure 4-17b)), while wall N2 fails at t=72.2 s, for an ALR of 44% (Figure 4-17a)). Please notice that this latter wall is located in the south side of the building and fails for a roof displacement of δ_r=-9.4 cm, in the opposite direction than the rest of the walls. This wall shows a failure at the base of the first story, similar to what was observed in Tower 2 (Figure 4-2h)). As the towers are extremely similar, it is not surprising that the model has predicted the failure of this wall, which was also observed in Tower 4.

Finally, vertical elements at axis 10 presented severe concrete crushing and loose of they axial capacity at t=80 s. Although concrete crushing is observed in other points of the

structure, it is not enough to cause the failure of the elements. Thus, it is observed that for this input, the model reproduces an abrupt compressive failure in walls at axis U, Q, N1, N2 and O, which is consistent with the reported observed damage after 2010 earthquake.

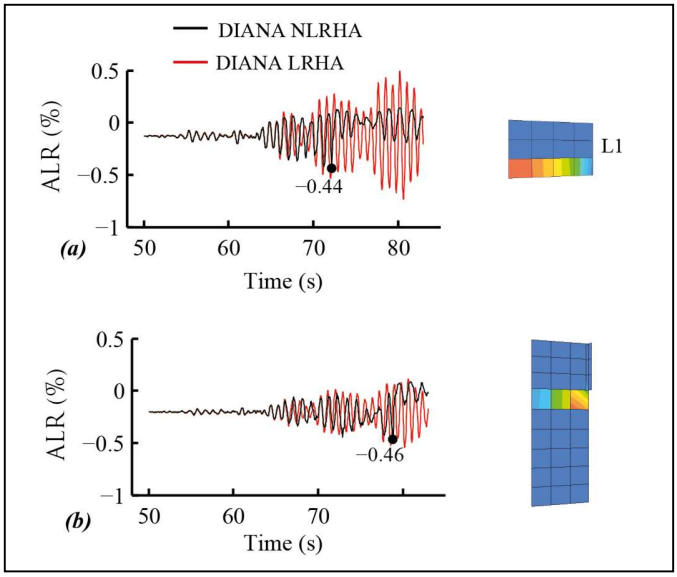

Figure 4-17: ALR history and concrete strains for I2: a) wall N2; and b) wall O.

Additionally, it is worth to comment some relevant aspects on the local response of damaged walls. First, Figures 4-18a) and b) show the kinematics of wall Q for the inelastic model at the failure instant (red), and for the first elastic mode of the building (blue), both scaled to the same lateral roof displacement. It is apparent that the kinematic of the inelastic model is consistent with the first elastic mode. Figure 18-b) also shows that the critical section of the wall is almost under pure compression at the failure instant, which is consistent with the first mode shape. This implies that the neutral axis of the section is approximately equal to the wall length ($c/l_w \approx 1$), and that the concrete ultimate compressive strain is reached before the reinforcement yields at the opposite side. Thus, using the first elastic mode shape to evaluate the 2D response of this type of walls through a pushover analysis may be a good proxy to the inelastic response, as presented elsewhere [7].

Second, the frequently used estimations of drift capacity of RC walls based on the plastic hinge approach is presented in Equations 4-1 and 4-2 [21],[22],[23]. Eq. 4-1 is based on a cantilever wall subjected to a lateral triangular distribution, and Eq. 4-2 is a simplified

expression of Eq. 4-1 which is consistent with the later for low values of $\emptyset_y$ ($\emptyset_y << \emptyset_u$). As discussed previously, in this case the wall fails in compression before reinforcement yields in tension, i.e. $\emptyset_y = \emptyset_u$ for the effect of estimating displacement capacity. Considering the ultimate curvature obtained by the DIANA model at the failure instant of wall Q, $\emptyset_u = 1.61e^{-5}$, the drift estimations of δ_u/h_w are 1.97% and 0.44% using Equations 4-1 and 4-2 respectively. The difference between both estimations occurs because the wall fails without ductility, thus the estimation given by Eq. 4-2 is not adequate. On the other hand, the estimation given by Eq. 4-1 is much higher than the estimation by the DIANA model because of the hypothesis of cantilever wall implicit in Eq. 4-1.

$$\delta_u = \frac{11}{40}\emptyset_y h_w^2 + (\emptyset_u - \emptyset_y) l_p (h_w - l_p/2) \quad \text{Eq. 4-1}$$

$$\delta_u = \emptyset_u l_p h_w \quad \text{Eq. 4-2}$$

In summary, the significant initial ALR due to gravity loads, plus the distribution of walls in the floor plan traduces in a 3D interaction between the wall and the rest of the structure that cannot be adequately represented by the typical assumption of a cantilever wall. In a cantilever wall subjected to lateral loads, the ALR of the wall does not increase due to lateral effect and remains equal to the gravity ALR, as discussed elsewhere [7]. Additionally, the estimation of roof displacement assuming a cantilever wall seems inappropriate for this type of walls, thus the relation between roof displacement and section capacity must be reconsidered for design purposes.

Finally, Figure 4-18b) shows the reinforcement strain history for one integration point of the first element in the critical section of wall Q (Figure 4-8). Steel remains within the elastic range prior to failure of the wall, with strains lower than 0.2% both in tension and compression. This implies that the effect of high tension strains prior to buckling does not occur in this case, as discussed elsewhere [7].

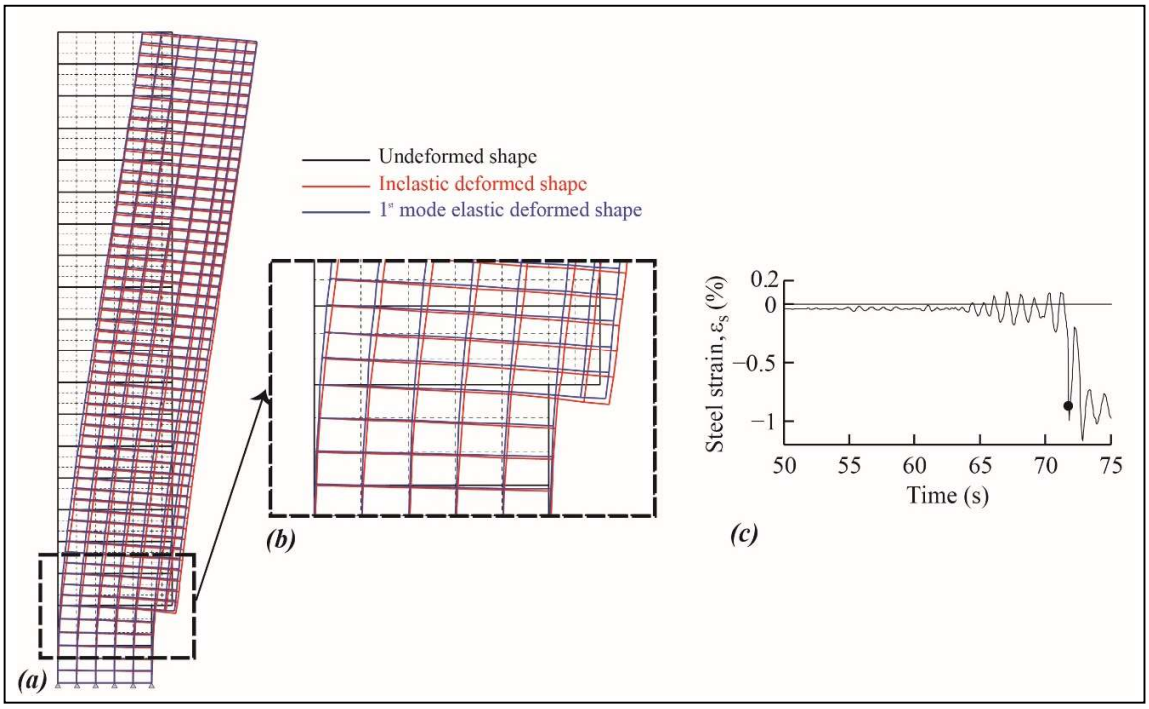

Figure 4-18: Local response for wall Q a) undeformed and deformed shape; b) zoom of undeformed and deformed shape; and c) reinforcement strain history.

4.5.3. Input I3: Three components of ground motion record

In this case, the three components of the seismic record are applied simultaneously. Figure 4-19 shows the response for both inputs *I1* and *I3*, i.e. single component and 3 components. Figure 4-19a) shows that the roof displacement for both inputs is very similar, however for input *I3* the peak roof displacement is 6.64 cm at around t=70 s, which is lower than for *I1* and occurs earlier. As an example of local response, Figure 4-19b) shows the ALR history for wall Q, showing the same effect than for roof displacement. Wall Q reaches a peak ALR similar for both inputs, but in the case of *I3* it is reached earlier in the response. The building does not present severe concrete crushing or compressive failure of any vertical element, as was the case for *I1*. Although the effect of including the other seismic record components has an impact on global and local responses, it does not condition the wall brittle failure expected.

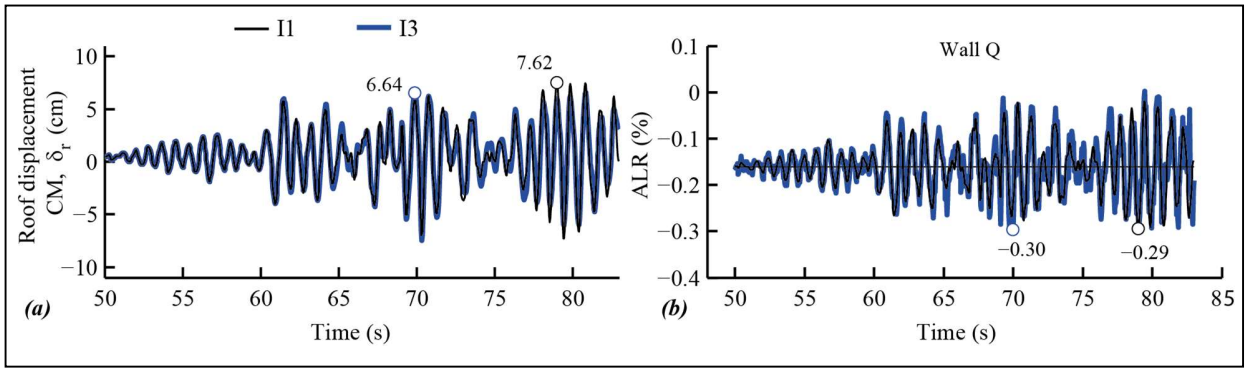

Figure 4-19: Inelastic dynamic response for I1 and I3: a) roof displacement in the N-S direction; and b) ALR in wall Q.

4.5.4. Input I4: Rotated three components of ground motion record

In this case, the three components of the seismic record are applied simultaneously but with the horizontal components switched in the direction applied. In this case, an abrupt failure is observed in critical walls, as was the case for *I2*. At t=70.9 s and for a roof displacement of δ_r=12 cm, walls Q and N1 reach concrete compressive strains higher than 0.5% and the walls lose their capacity abruptly, as shown in Figure 4-20 and 4-21. At t=77.6 s, the same effect occurs in wall U, for a roof displacement of δ_r=13 cm. Failure in walls U and Q occurs similarly for inputs *I2* and *I4*, for similar roof displacements and ALRs. However, failure of wall N1 occurs at an ALR=44%, much lower than the 63% reached for input *I2*. For this input, wall N2 fails in compression at t=67.2 s with an ALR of 55%, and is the first wall that show failure in compression, before Q and N1. Additionally, wall O shows compressive failure at t=77.7, just after failure of wall U. Significant concrete crushing is observed in other elements of the building after t=77.7 s.

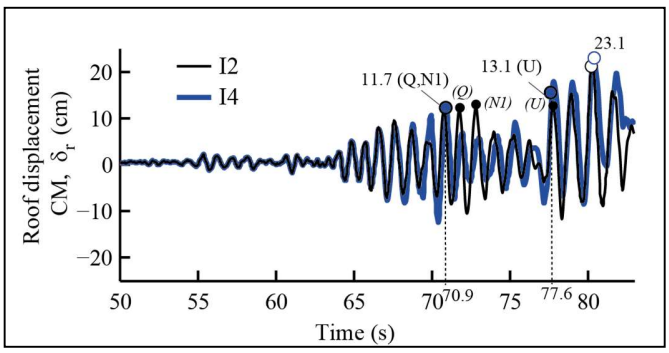

Figure 4-20: Roof displacement in the N-S direction for I2 and I4.

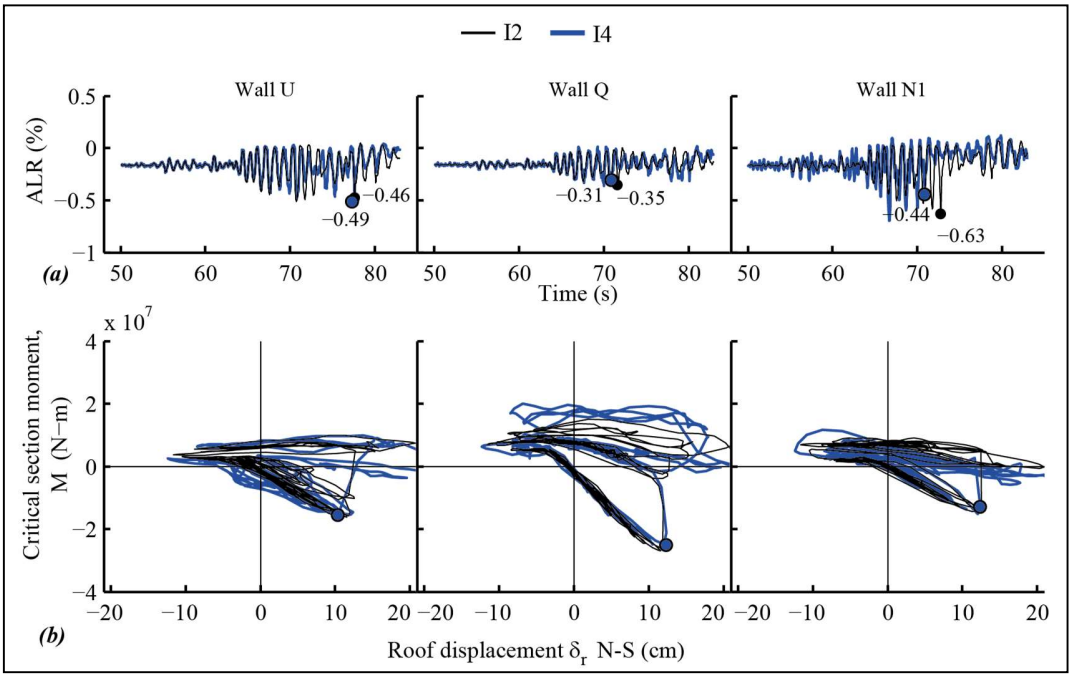

Figure 4-21: Local response of critical walls for I2 and I4: a) axial load ratio history; and b) bending moment versus roof displacement history.

Results for the different inputs considered in this section show that the compressive failure at critical walls (U, Q and N1) is sensitive to the seismic record considered, since it shows abrupt failure for *I2* and *I4*, and no failure for *I1* and *I3*. The effect of the three components is not significant when the building does not present severe damage (*I1* and *I3*). However, when the critical walls fail (*I2* and *I4*), the effect of the additional seismic components is significant. The roof displacement at failure of critical walls Q, U and N1 does not vary significantly for *I4*, however the failure sequence and the peak ALRs of critical walls differ.

4.6. Parametric Study

In this section, three different inelastic models are evaluated, and their responses to input *I2* are compared with the response presented in Section 4.5 for the same input, which from now on will be referred to as reference model M0. The inelastic models considered are summarized in Table 4-2, which characterizes by: (i) M1 concentrates the inelastic behavior

in a subset of 14 wall elements distributed in first story and basements (detailed in Table 4-3), which were selected based on the observed damage and on results of elastic dynamic analysis; (ii) M2 concentrates the inelastic behavior in the same elements than M1 plus all other wall elements in the first basement (B1); and (iii) M3 is the same as M0, but the stiffness of the slabs is reduced to 0.25 times the original stiffness, in order to represent inelastic behavior of the slabs.

Table 4-2. Inelastic models considered

Model	Elements with inelastic behavior
M1	14 walls (L1, B1 and B2)
M2	M1+ all B1 walls
M3	As M0, but slabs with $EI=0.25EI_0$

Table 4-3. Inelastic elements in M1

Non linear stories	Non linear walls													
	N1	N2	O	Q	R	T	U	V	X	Y	Z	1	5	6
B2	✓	-	✓	✓	-	✓	✓	✓	✓	-	-	✓	✓	✓
B1	✓	-	✓	✓	-	✓	✓	✓	✓	-	-	✓	✓	✓
L1	✓	✓	✓	✓	✓	✓	✓	✓	✓	✓	✓	✓	✓	✓

Figure 4-22 shows roof displacement in the N-S direction for the three models. All models show failure of the critical walls at the instants identified in Figure 4-22, and the corresponding ALRs at failure are summarized in Table 4-4.

First, model M1 presents significant difference in the global response with respect to M0 (Figure 4-22a)). In M1 the peak roof displacement reached is 13.8 cm, which is 36% lower than the peak for M0 (21.4 cm). Although critical walls show compressive failure at similar levels of ALR, failures occur later than for M0 (Table 4-4), specially for Q and N1.

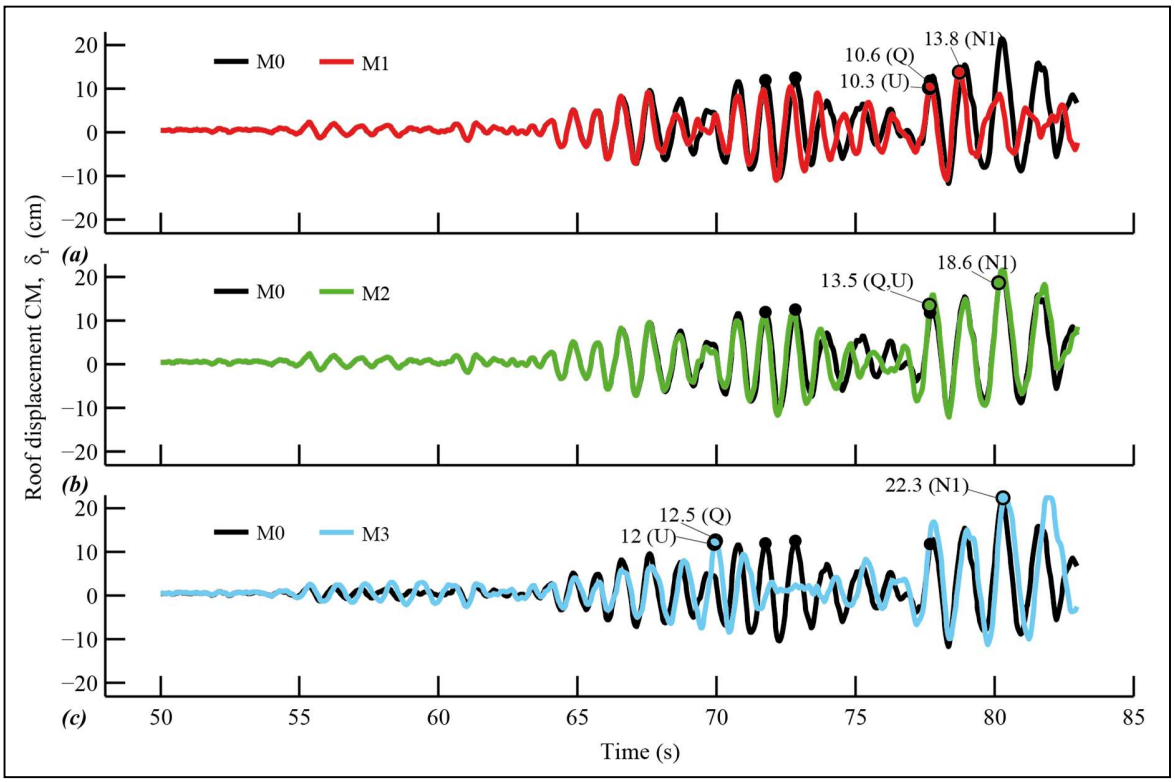

Figure 4-22: Global response, roof displacement: a) M1; b) M2; and c) M3.

Table 4-4. Local responses at failure for critical walls

		U			Q			N1		
Model	Peak δ_r (cm)	ALR (%)	t (s)	δ_r (cm)	ALR (%)	t (s)	δ_r (cm)	ALR (%)	t (s)	δ_r (cm)
M0	21.4	46	77.7	11.9	35	71.8	12	63	72.9	12.5
M1	13.8	48	77.6	10.3	34	77.6	10.6	63	78.7	13.8
M2	18.6	46	77.7	13.5	35	77.7	13.5	60	80.2	18.6
M3	22.3	45	69.9	12	31	69.9	12.5	63	80.3	22.3

Results for M2 (Figure 4-22b)) show that an abrupt failure of walls Q and U occurs simultaneously at t=77.7 s for a roof displacement of 13.5 cm, while wall N1 fails at t=80.2 s for a roof displacement of 18.6 cm. Wall Q fails later than for M0, but wall U fails at the same moment. The ALRs at failure instant are very similar for both M0 and M3 models (Table 4-4).

Finally, Figure 4-22c) shows that when a reduced stiffness is considered in the slabs (M3),

a peak roof displacement of 12 cm is achieved earlier than in model M0. At this point (t=69.9 s), an abrupt failure occurs in wall U, while wall Q fails in the next time instant for a roof displacement of 12.5 cm. As was the case for model M2, wall N1 is the last one to fail (Table 4-4). Again, the ALRs at failure are very similar for both M3 and M0 models.

By comparing M0, M1 and M2 it is possible to conclude that the model which considers inelastic elements in the critical story (M2) is sufficient to predict the expected response using the method proposed in this article. Although the failures at critical walls occur at different instants and in a different sequence, the ALRs at failure instants are very similar and the predicted peak roof displacement is also in good agreement with the reference model M0. However, considering isolated elements such as in model M1 and neglecting the inelastic behavior of some elements of the critical story floor plan traduces in larger differences in response with respect to M0. Finally, the effect of reducing slab stiffness is significant in the failure sequence, but the ALRs at failure of each critical wall are very similar, with a maximum difference of 11% in the case of wall Q.

4.7. Discussion and Conclusions

This article presents an assessment of the inelastic response and damage of a real RC shear wall building using a 3D finite element model developed in the software DIANA. The model was initially validated with a linear elastic building model developed in ETABS. The inelastic DIANA model considered *the total strain rotating crack model* for concrete behavior, an embedded formulation for steel, and a localization of the inelastic behavior in the shear walls of the first three levels of the building, i.e. the first story and basements.

Analytical results show good agreement with the damage observed after the 2010, Chile earthquake, at least for the most critical ground motion component of the seismic record considered. Such record was obtained closest to the building location and was input in the critical direction of the building (*I2*). If the other component of the record is used as an input, only concrete cracking is observed with no significant inelastic behavior in compression (*I1*). The inelastic model did not consider the buckling of reinforcement, which is one of the

possible causes of why there is no significant damage predicted by this input.

For the critical input component (*I2*), a sudden compression failure of walls is predicted. The compressive strains in concrete elements increase dramatically in one cycle, and cracking spreads rapidly toward the interior of the walls, causing an almost complete loss in bending capacity of the wall section. The model predicts this type of sudden compressive failure in the three critical elements (U, Q and N1), and in walls O and N2, implying that the geometry and location of the failure is very similar to the one observed after the earthquake. For the three critical elements U, Q and N1, the failure occurred at the top of the first basement (B1), just below the setback of the wall (vertical irregularity). For wall O the failure also occurred in the same section, but for wall N2, it was located at the base of the first level. The latter is also consistent with observations. The first wall failure occurred for a roof displacement of about 12 cm, which corresponds to a roof drift ratio of 0.3%, which is smaller than the estimations of 0.8% to 1% roof drift ratios presented elsewhere for vulnerable buildings. These wall failures also occur for ALRs between 35% and 63%, and represent dynamic amplification factors relative to the gravitational ALRs between 2.2 and 3.7.

Local results at wall Q shows that the kinematics at failure instant are consistent with the first elastic mode shape, and that the critical section wall is almost under pure compression, without previous yielding of steel in tension. The typical assumption of cantilever wall is then inappropriate for the walls analyzed in this study, thus it is recommended to reevaluate the relation between roof displacement and section capacity for design purposes.

The effect of simultaneous action of the three ground motion components is not significant for the building case without severe damage (*I3*). However, as soon as the critical walls fail (*I4*), the effect of the additional seismic components of ground motion becomes significant. The roof displacement at which the critical walls reach failure does not vary significantly if one or multiple ground motion components are considered; however, the sequence of failure and the ALRs of critical walls differ for the cases with one or multiple components.

A parametric study was also developed to evaluate the effect of the number and location of inelastic elements in the building, and the effect of stiffness reduction in slabs. It is possible

to conclude that the model which considers inelastic elements concentrated in the critical story (B1) is sufficient to predict the expected response using the method proposed in this article. However, neglecting the inelastic behavior of some elements within a critical story does not predict a global response consistent with the reference model. Finally, the effect of reducing stiffness in the slabs is significant in the failure sequence, but not for the ALRs at failure.

The model results presented herein consistently show that the wall behavior was brittle, and hence, concrete compressive strains increased dramatically within one cycle, causing a sudden loss in wall capacity at instants with high ALRs. The wall response is highly affected by the 3D interaction of the building and the distribution of the walls in the floor plan, which traduce in significant increase in ALRs. However, because results are shown only for 30 seconds of a single seismic record, it is not possible to discard completely that the wall damage could have been produced by cyclic behavior, say after 80 seconds, or for a seismic record different from the one considered.

In summary, under the set of modeling assumptions presented herein, and for the inputs considered, available analytical models were able to predict in this case, the geometry and magnitude of the observed damage during the earthquake, as well as the lateral displacement demand expected. In the future these results should be validated for other buildings undergoing similar damage and with other ground motions.

ACKNOWLEDGEMENTS

This research has been sponsored by the National Science and Technology Council of Chile, CONICYT, under grant Fondecyt 1141187, and by the National Research Center for Integrated Natural Disaster Management CONICYT/FONDAP/15110017. The authors are grateful for this support and would like to thank also the company Spoerer Ingenieros Asociados SpA.

REFERENCES

[1] Alarcon C., Hube M.A., de la Llera J.C. (2014) "Influence of axial load in the seismic behavior of RC walls unconfined wall boundaries." Engineering Structures; 73:13-23.

[2] Hube M.A., Marihuén A., de la Llera J.C., Stojadinovic B. (2014) "Seismic behavior of slender reinforced concrete walls." Engineering Structures; 80:377-388.

[3] Massone L.M., Polanco P., Herrera P. (2014) "Experimental and analytical response of RC wall boundary elements" Proceedings of the 10th National Conference in Earthquake Engineering, Earthquake Engineering Research Institute, Anchorage, AK.

[4] Arteta C.A., To D.V., Moehle J.P. (2014) "Experimental response of boundary elements of code-compliant reinforced concrete shear walls." Proceedings of the 10th National Conf. in Earthquake Engineering, Earthquake Engineering Research Institute, Anchorage, AK.

[5] Magna-Verdugo C.E., Kunnath S.K. (2014) "Non-linear response analysis of reinforced concrete shear walls using multi-spring macro-models." Proceedings of the 10th National Conf. in Earthquake Engineering, Earthquake Engineering Research Institute, Anchorage, AK.

[6] Vásquez J.A., de la Llera J.C., Hube M.A. (2016) "A regularized fiber element model for reinforced concrete shear walls". Earthquake Engineering & Structural Dynamics, doi:10.1002/eqe.273

[7] Jünemann R., de la Llera J.C., Hube M.A., Vasquez J.A., Chacón M.F. (2016) "Study of the damage of reinforced concrete shear walls during the 2010, Chile earthquake", Earthquake Engineering and Structural Dynamics, 45;10:1621-1641.

[8] Kozmidis A., Melek M., Massone L., Orakal K. (2014). "Comparison of industry-standard nonlinear dynamic analysis methods with observed damage on a RC building." *Proceedings of the 10th National Conference in Earthquake Engineering*, Earthquake Engineering Research Institute, Anchorage, AK.

[9] NERHP (2014). "Recommendations for seismic design of reinforced concrete wall buildings based on studies of the 2010, Maule, Chile Earthquake." NIST GCR 14-917-25. US Department of Commerce.

[10] Ebrahimian H., Astroza R., Conte J.P., Restrepo J.I., Hutchinson T.C. (2014)

"Experimental Validation of Dynamic Nonlinear FE Model of Full-Scale Five-Story Reinforced Concrete Building". Proceedings of the 9th International Conference on Structural Dynamics, EURODYN 2014, Porto, Portugal

[11] Computers and Structures, Inc. (2010). CSI Analysis Reference Manual for SAP2000, ETABS, SAFE and CSIBridge. Berkeley, California.

[12] TNO DIANA. (2010). DIANA - User's Manual.

[13] Wallace J.W., Massone L.M., Bonelli P., Dragovich J., Lagos R., Lüders C., Moehle J. (2012) "Damage and Implications for Seismic Design of RC Structural Wall Buildings." Earthquake Spectra; 28(S1); S281-S299

[14] Rojas F, Naeim F, Lew M, Carpenter LD, Youssef NF, Saragoni GR, Schachter M. (2010) "Performance of tall buildings in Concepcion during the 27 February 2010 moment magnitude 8.8 offshore Maule, Chile earthquake". Structural Design of Tall and Special Buildings; 20:37–64.

[15] Carpenter LD, Naeim F, Lew M, Youssef NF, Rojas F, Saragoni GR, Schachter M. (2011) "Performance of tall buildings in Viña del mar during the 27 February 2010 offshore Maule, Chile earthquake." Structural Design of Tall and Special Buildings; 20:17–36.

[16] Chacón M.F., de la Llera J.C., Hube M.A., Marques J., Lemnitzer A. (2016) "Epistemic uncertainty in the seismic response of RC free-plan buildings" Engineering Structures, submitted for publication.

[17] Universidad de Chile. Departamento de Ingeniería Civil and Oficina Nacional de Emergencia Chile (ONEMI). Earthquakes of Chile; 2010. <http:// terremotos.ing.uchile.cl/2010> [in Spanish] [accessed 21.02.14].

[18] Arias A. (1970) "A measure of earthquake intensity". Seismic design for nuclear power plants. MIT Press, p.438-483. Cambridge, Massachusetts.

[19] D.S. N 61 MINVU. Building seismic design code, replacing D.S N 117, 2010. Chilean Ministry of Housing and Urbanism, Diario Official; 13 December 2011[in Spanish].

[20] Lagos R., Kupfer M., Lindenberg J., Bonelli P., Saragoni R., Guendelman T., Massone L., Boroschek R., and Yañez F. (2012) "Seismic Performance of High-rise Concrete Buildings in Chile". International Journal of High-Rise Buildings. Vol 1; 3:181-194.

[21] American Concrete Institute ACI (2008) Building code requirements for structural concrete and commentary ACI 318-08. American Concrete Institute, Detroit

[22] Alarcon C., Hube M.A., Jünemann R. and de la Llera J.C. (2015) "Characteristics and displacement capacity of reinforced concrete walls in damaged buildings during 2010 Chile earthquake". Bulletin of Earthquake Engineering 13:1119-1139.

[23] Massone L. (2013) "Fundamental Principles of the reinforcement concrete design code changes in Chile following the Mw 8.8 earthquake in 2010". Engineering Structures, 56 (2013) 1335-1345.

5. SUMMARY AND CONCLUSIONS

This research presents an analytical investigation on the behavior of RC wall structures during the 2010 Chile earthquake through three phases that correspond to the different chapters of this dissertation: (i) a statistical analysis of reinforced concrete wall buildings damaged during the earthquake based on the analysis of data gathered in the field; (ii) inelastic analysis and response of RC walls damaged during 2010 earthquake by means of pushover analysis of single walls; and (iii) three-dimensional inelastic dynamic analysis and response of a real RC building based on a detailed finite element model. Although the analytical models considered throughout this dissertation are very different from each other and still sensitive to modeling assumptions, results show that the geometry and magnitude of the observed damage during the earthquake as well as the lateral displacement demand expected can be represented by analytical models under certain conditions. Results show a brittle wall behavior, characterized by high axial load ratios and low roof displacements.

The first phase of this research (Chapter 2) presents a building database composed by a group of 36 reinforced concrete wall buildings taller than 9 stories that suffered moderate to severe damage during the earthquake and located in the densest cities affected by the seismic event: Santiago, Viña del Mar, and Concepción. For these buildings, which compose the inventory of damaged buildings, structural and/or architectural drawings, soil-mechanics studies, and damage inspection reports were collected for almost all cases, thus generating a complete database of damaged buildings. Building characteristics such as location, year of construction, number of stories and damage level, are presented in this phase for the inventory of damaged buildings. Additionally, different structural characteristics or parameters were identified and obtained for each of the buildings: (i) geometric characteristics: floor plan aspect ratio and slenderness ratio; (ii) material properties: concrete and steel strength, and type of soil; (iii) dynamic parameters: estimated period T and stiffness ratio h/T; (iv) wall-related parameters: wall thickness, wall density, wall density per weight (DNP) and axial load ratio (ALR); and (v) irregularity indices: ratio of average floor plan area above and below ground level ($\overline{A_a}/\overline{A_b}$), ratio of average wall density above and below ground level ($\overline{\rho_a}/\overline{\rho_b}$), and the wall area ratio

WA_{s1}/WA_1, which represents the wall area of the walls in the first story that have continuity into the first basement. As possible, all characteristics of the inventory of damaged buildings were compared with the general building inventory, which consists of a database of approximately 500 RC Chilean buildings that have been studied in the past, and with a small benchmark group of 7 essentially identical but undamaged buildings.

Results of this first phase show that the inventory of damaged buildings is characterized by: (i) mainly new structures, built after year 2000; (ii) high average wall densities (average 2.8% on each direction), which is similar to that of typical Chilean buildings (pre 1985 earthquake); (iii) small wall thickness with an average of 20 cm ; (iv) high axial load ratios due to gravity loads with an average of 10.4%; and (v) significant vertical irregularity with an average of 82% of wall area from first story that continues to the first basement. The same parameters were calculated for the benchmark group of 7 undamaged buildings, and results were very similar to those of the inventory of damaged buildings, showing that none of the selected global building parameters is able to solely explain the observed damage and hence is the result of several factors such as seismic intensity, soil type, structural configuration, structural detailing and construction details, among others.

Additionally, the association between building damage level and global building parameters was explored in this phase by means of *proportional odds logistic regression models* (POLR). Results from univariate models show that the most significant variables to explain the observed damage level are the region were the building was located and the soil type. A series of multivariate POLR models were also performed, isolating the effect of the most significant variables *Region* and *Soil type*. In this case, the only significant variables are the stiffness ratio *h/T* and the building height H. The other variables did not seem to be very significant when included in a model together with *Region* and *Soil type*.

Although not captured by statistical analysis, field observations and experimental results have shown that high ALR reduce ductility capacity of RC walls, thus the ALRs due to seismic effects in RC walls of damaged buildings are also studied. A simple procedure to estimate the axial load ratios in RC walls, including both static and dynamic effects, is presented by means

of the amplification factor AF, which is defined as the ratio between the total maximum axial load ratio including dynamic effects ($max(X_T)$) relative to the static axial load ratio (X_S), where $max(X_T) = |X_S| + max(X_D)$. The AF is estimated based on a peak factor p and the ratio σ_{X_D}/X_S between the standard deviation of the dynamic component of the ALR (σ_{X_D}) and the static component of the ALR (X_S). A dynamic elastic analysis was developed for four buildings damaged during the earthquake and subjected to 4 seismic records, two of them corresponding to seismic records registered during the 2010 earthquake, and the other two corresponding to artificial records compatible with the elastic design spectrum defined by the Chilean seismic code. Aggregate results for all RC walls located in the first stories of each building show that AF depends primarily on the period of the building in each direction and on the seismic intensity. Results show that AF varies between 1.3 and 2.9 for building periods *T* ranging from 0.4 s to 1.6 s, and ground motions normalized to 0.2g at the fundamental period of the building. The total ALR including the static and dynamic contribution or the dynamic amplification factor AF may be used to complement other parameters to foresee the vulnerability of existing shear wall buildings, like the shear wall density ρ and *h/T*, which have proven to be no longer sufficient to predict seismic performance of these structures with brittle behavior, which is highly controlled by large axial loads.

The second phase of this research (Chapter 3) presents inelastic analytical models to forecast the observed failure in some RC shear walls during the 2010 Chile earthquake. Two-dimensional finite element inelastic pushover analysis developed in the software DIANA are presented in this phase following the *total strain rotating crack* model for concrete behavior. Four-node shell elements are considered for concrete, while reinforcement is modeled using the embedded formulation using exponential hardening stress-strain constitutive model that is equal in tension and compression, neglecting the effect of bar buckling or fracture. First, different stress-strain constitutive models for concrete in compression are evaluated and compared with experimental results of RC walls. Results show that the constitutive models that better correlate with experimental behavior are the Parabolic or Multilinear constitutive models, with a proper regularization according to the mesh-size.

Then, a RC wall from a building severely damaged during 2010 earthquake is modeled and inelastic pushover analysis is developed considering four different displacement patterns: (i) a constant lateral displacement at all roof nodes of the wall (R); (ii) floor lateral nodal displacements that increase in height according to an inverted triangular pattern (T); (iii) floor lateral nodal displacements that result from the predominant elastic mode shape in the direction of the wall (M1); and (iv) floor lateral and vertical nodal displacements that result from the predominant elastic mode shape (MV1). By including the vertical displacements according to the mode shape, load case MV1 aims to represent the three dimensional interaction of the wall with the rest of the structure. Vertical displacements represent the framing action of the slab and enable to capture variations in the axial load of the wall due to lateral motion of the building, which are neglected in the other displacement patterns.

The first three displacement patterns implicitly assume a constant axial load equal to the gravity loads, which translates into poor outcomes when trying to represent the damage pattern observed in the wall. First, case R does not present strength degradation and fails to resemble the horizontal crack observed at the first basement during the earthquake; second, case T predicts a limited ductility behavior, but damage localizes at the bottom of the wall, which is not consistent with the observed damage after the earthquake; third, case M1 is able to predict the initial damage pattern, but concrete crushing does not propagate toward the interior of the wall, as with case R. Finally, results for case MV1 present clear strength degradation for different stress-strain constitutive models after the roof displacement exceeds approximately 9 cm, concrete crushing concentrates in the same critical section than the observed after the earthquake, and propagates towards the interior of the wall in a damage pattern similar to the one observed in the real wall. In this case, the ALR in the wall increases from 15% due to gravity loads up to 45%. This increase in the ALR is consistent with results of a 3D dynamic inelastic analysis of the building developed using fiber elements concentrated in some wall elements of the first stories.

Results from pushover analysis show that classical pushover analyses, which neglects coupling of the vertical elements with other resisting elements by the floor slab, are not capable

of representing the observed damage because these models cannot take into account the increase in axial loads due to seismic action. However, if the wall-slab interaction is included in the planar pushover analysis by imposing vertical nodal floor displacements according to the predominant lateral mode in the direction of the wall, the results are consistent with the observed failure mode. Although this procedure has evident limitations, it may become a simple alternative to analyze the complex inelastic behavior of RC wall buildings.

Finally, the third phase of this study (Chapter 4) presents a three-dimensional inelastic dynamic analysis of a real building damaged during the 2010 earthquake. The building is modeled in the software DIANA with 3 or 4-node shell elements, following the *total strain rotating crack* model for concrete and embedded formulation for reinforcing steel, considering similar assumptions than in the 2D model. Because the damage observed in this building was localized mainly in the first basement, inelastic elements are concentrated in the first three stories of the building, while the rest of the structure is model with linear-elastic behavior. The DIANA model was validated first through an elastic dynamic analysis with an equivalent model developed in ETABS.

For the inelastic dynamic analysis, a ground motion recorded in the vicinity of the building during 2010 earthquake is considered and different inputs are evaluated: the two horizontal components of the seismic record applied independently to the critical direction of the building (*I1* and *I2*), the three components of the seismic record applied simultaneously to the building (*I3*), and finally, the horizontal components are switched in the direction applied (*I4*). For input *I1* only concrete cracking is observed, without significant inelastic incursion of concrete in compression. However, for input *I2*, which is the most critical horizontal seismic component, results of the dynamic inelastic analysis show an abrupt failure of walls in compression, with concrete compressive strains that increase dramatically in one cycle and spreads towards the interior of the wall. The geometry and location of the failures predicted by the analytical model are in good agreement with the damage observed after the earthquake. The observed failures occur in RC walls for drift ratios of approximately 0.3% and for ALRs between 35% and 63%, which relative to the gravitational ALRs correspond to dynamic amplification factors between

2.2 and 3.7.

When considering the three components simultaneously, no significant effect is observed in the case of input *I3*, since the building remains essentially in the elastic range, as was the case for *I1*. However, for input *I4* brittle failures are observed, as was the case for input *I2*. Although the roof displacement at failure does not vary significantly, the failure sequence and the ALRs at failure are different.

Finally, different models are subjected to the same input *I2*, and responses are compared with the previous results. The inelastic models aims to evaluate the effect of the amount and location of inelastic elements and of the slab stiffness in the seismic behavior. Results show that considering inelastic behavior concentrated in isolated elements, but not in all the elements of the critical stories, do not predict a global response consistent with the reference model. However, considering inelastic elements concentrated in the critical story (first basement in this case) is sufficient to predict the observed brittle failure. Finally, the effect of reducing slab stiffness to 0.25 times the original stiffness affects the failure sequence, but the ALRs at failure do not vary significantly.

In summary, different analytical models are considered to represent the observed damage in RC walls after 2010 earthquake. Two-dimensional pushover analysis and two different 3D inelastic dynamic analysis are evaluated, which present different modeling assumptions such as the type of inelastic elements, the cyclic behavior of steel, the location and amount of inelastic elements for the 3D models and the type of analysis. Although the analytical models are very different and still sensitive to modeling assumptions, analytical results presented in this research consistently show that the wall behavior was brittle, characterized by high ALR and low roof displacements, without energy dissipation, and that failure occurs abruptly within one cycle. In addition, the analytical models were able to predict the geometry and magnitude of the observed damage during the earthquake as well as the lateral displacement demand expected. However, it is not possible to completely discard that the wall damage could have been caused by significant cyclic behavior associated with lighter axial loads.

Although still complex and highly computationally demanding, 3D inelastic finite element models with inelasticity concentrated in first stories have shown to be a good alternative to evaluate seismic performance of RC structures. Future work to improve the proposed analytical methodology could attempt to include reinforcement buckling and fracture in the steel stress-strain constitutive model, to consider other seismic records from 2010 Chile earthquake, and to evaluate other modeling assumptions such as the mesh-size and the soil-structure interaction. Additionally, this type of analysis could be extended to other buildings with similar damage and compare with other 3D inelastic methodologies. Finally, a new parametric study could be developed in order to evaluate different retrofit alternatives and the effect of non-conventional upgrading techniques based on energy dissipation devices.